Investigating the Dynamics of Polarization Reversal in Ferroelectric Thin Films by Time-Resolved X-ray Diffraction

DISSERTATION

Zur Erlangung des akademischen Grades

„Doctor rerum naturalium“

(Dr. rer. nat.)

in der Wissenschaftsdisziplin Experimentalphysik

eingereicht an der

Mathematisch-Naturwissenschaftlichen Fakultät

der Universität Potsdam

von

Christelle Larodia Tchoumba Kwamen

aus Buea, Kamerun

December 2018

Abstract

Ferroic materials have attracted a lot of attention over the years due to their wide range of applications in sensors, actuators, and memory devices. Their technological applications originate from their unique properties such as ferroelectricity and piezoelectricity. In order to optimize these materials, it is necessary to understand the coupling between their nanoscale structure and transient response, which are related to the atomic structure of the unit cell.

In this thesis, synchrotron X-ray diffraction is used to investigate the structure of ferroelectric thin film capacitors during application of a periodic electric field. Combining electrical measurements with time-resolved X-ray diffraction on a working device allows for visualization of the interplay between charge flow and structural motion. This constitutes the core of this work. The first part of this thesis discusses the electrical and structural dynamics of a ferroelectric Pt/Pb($Zr_{0.2}$,$Ti_{0.8}$)O_3/$SrRuO_3$ heterostructure during charging, discharging, and polarization reversal. After polarization reversal a non-linear piezoelectric response develops on a much longer time scale than the *RC* time constant of the device. The reversal process is inhomogeneous and induces a transient disordered domain state. The structural dynamics under sub-coercive field conditions show that this disordered domain state can be remanent and can be erased with an appropriate voltage pulse sequence. The frequency-dependent dynamic characterization of a Pb($Zr_{0.52}$,$Ti_{0.48}$)O_3 layer, at the morphotropic phase boundary, shows that at high frequency, the limited domain wall velocity causes a phase lag between the applied field and both the structural and electrical responses. An external modification of the *RC* time constant of the measurement delays the switching current and widens the electromechanical hysteresis loop while achieving a higher compressive piezoelectric strain within the crystal.

In the second part of this thesis, time-resolved reciprocal space maps of multiferroic $BiFeO_3$ thin films were measured to identify the domain structure and investigate the development of an inhomogeneous piezoelectric response during the polarization reversal. The presence of 109° domains is evidenced by the splitting of the Bragg peak.

The last part of this work investigates the effect of an optically excited ultrafast strain or heat

pulse propagating through a ferroelectric $BaTiO_3$ layer, where we observed an additional current response due to the laser pulse excitation of the metallic bottom electrode of the heterostructure.

Kurzdarstellung

Ferroika haben aufgrund vielfältiger Anwendungsmöglichkeiten in Sensoren, Motoren und Speichermedien in den letzten Jahren viel Aufmerksamkeit erhalten. Das Interesse für technologische Anwendungen ist in ihren einzigartigen Eigenschaften wie Ferroelektrizität und Piezoelektrizität begründet. Um die Eigenschaften dieser Materialien zu optimieren ist es notwendig, die Kopplung zwischen ihrer Nanostruktur und der zeitabhängigen Antwort auf die Anregung zu verstehen, welcher von der Atomstruktur der Einheitszelle abhängig ist.

In dieser Arbeit wird Röntgenbeugung an einem Synchrotron verwendet, um die Struktur eines ferroelektrischen Dünnschichtkondensators während eines angelegten elektrischen Feld zu beobachten. Den Kern dieser Arbeit bildet die Kombination aus elektrischen zeitaufgelösten Röntgenbeugungsmessungen an einem betriebsfähigen Kondensator, was die Visualisierung des Zusammenspiels zwischen Ladungsbewegung und Strukturdynamik ermöglicht. Der erste Teil der Arbeit befasst sich mit der elektrischen und strukturellen Dynamik einer ferroelektrischen $Pt/Pb(Zr_{0.2},Ti_{0.8})O_3/SrRuO_3$ Heterostruktur während des Ladens, Entladens und der Polarisationsumkehr. Nach der Umkehr der Polarisation bildet sich auf einer längeren Zeitskala als die RC-Zeitkonstante der Probe ein nichtlineares piezoelektrisches Signal aus. Der Umkehrungsprozess ist inhomogen und induziert einen vorübergehenden Zustand ungeordneter Domänen. Die strukturelle Dynamik mit einem angelegten elektrischen Feld unterhalb des Koerzitivfelds zeigt, dass dieser ungeordnete Zustand remanent sein kann und mit einer entsprechenden Abfolge von Spannungspulsen wieder entfernt werden kann. Die frequenzabhängige Charakterisierung der Dynamik einer $Pb(Zr_{0.52},Ti_{0.48})O_3$ Schicht mit einer Zusammensetzung, die der morphotropen Phasengrenze entspricht, zeigt, dass bei hohen Frequenzen die begrenzte Domänenwandgeschwindigkeit eine Phasenverzögerung zwischen dem angelegten Feld und dem strukturellen sowie dem elektrischen Signal verursacht. Eine externe Änderung der RC-Zeitkonstante verzögert den Schaltstrom und verbreitert die elektromechanische Hysteresekurve, während im Kristall eine höhere kompressive piezoeletrische Spannung erzeugt wird.

In dem zweiten Teil dieser Arbeit wurde der reziproke Raum von multiferroischen dünnen $BiFeO_3$ Filmen vermessen, um die Domänenstruktur zu identifizieren und die Entwicklung eines inhomogenen piezoelektrischen Signals während der Polarisationsumkehr zu untersuchen. Das Aufspalten des Bragg Reflexes ist ein Hinweis auf die Existenz von 109° Domänen.

Der letzte Teil der Arbeit beschäftigt sich mit dem Effekt, den ein durch optische Anregung erzeugter ultraschneller Verspannungs- oder Wärmepuls hervorruft, der durch eine ferroelektrische $BaTiO_3$ Schicht propagiert. Dabei wurde durch die Anregung der unteren metallischen Elektrode der Heterostruktur durch den Laserpuls ein zusätzliches Ladungssignal beobachtet.

Contents

List of Figures

List of Tables

Chapter 1

Introduction

Smart materials are widely studied nowadays due to their applications in modern technologies such as memory devices, sensors, actuators, transducers, micro electromechanical systems and energy harvesters [13, 14]. Most of these applications are possible because the macroscopic properties of these materials can be controlled and manipulated by external stimuli. Ferroics are materials like ferroelectrics, ferroelastics or ferromagnets, which exhibit long-range electronic, structural and or magnetic orderings, respectively. A material is termed as ferroelectric when it exhibits reversible spontaneous electric polarization in analogy to the permanent magnetic moment in ferromagnetic materials. Ferroelasticity is the mechanical equivalent of this phenomenon, whereby a material exhibits spontaneous strain. Ferroelasticity and ferroelectricity are both sub-classes of piezoelectricity, where a mechanical stress in the material produces an electric charge (direct piezoelectric effect) or the application of an electrical charge produces a mechanical strain (inverse piezoelectric effect). Ferromagnets in contrast are materials with permanent magnetic moment. Some materials possess more than one type of primary ferroic order. Materials possessing both electric and magnetic long-range ordering are termed multiferroics. Multiferroics can be classified in three different classes, depending on the origin of ferroelectricity in them [15, 16]. In the first class, ferroelectricity arises from electronic ordering (charge) just like in ferroelectrics. In the second it arises from geometrical constraints, the ferroelectric distortion is driven by ionic size effects and in the third class hybridization is at the origin of ferroelectricity. In the latter class, magnetism and ferroelectricity are associated with two different cations. A good example is $BiFeO_3$. Here the ferroelectricity arises from hybridization between the $2p$ orbitals of O and $6p$ orbitals of Bi.

The structure of these materials is generally complex and their properties altered by parameters such as defects, thickness, strain and doping, makes their understanding a challenge. For example, the study of the dynamics of polarization reversal in ferroelectric thin films revealed that domain motion during the switching can be hindered by domain wall pinning resulting in fatigue [17, 18]. Since most applications use thin films, characterizing ferroic thin films in their working device geometry is of paramount interest to the scientific community. X-ray diffraction is a well known technique for probing the structure of materials [19]. Lately, time-resolved X-ray diffraction has been introduced to accurately characterize ferroic film response to external electric fields [20]. The piezoelectric deformation of the unit cell is observed as a shift of the Bragg peak position in reciprocal space, while polarization reversal is marked by a change in diffracted intensity, as predicted by the violation of Friedel´s law. On the other hand, electrical characterization techniques such as polarization-electric field hysteresis loop and positive-up negative-down (abbreviated PUND) pulse measurements had been introduced earlier to characterize the macroscopic polarization in these films [21]. A direct correlation between these two parameters constitute the main focus of the present study.

In this dissertation, time-resolved X-ray diffraction together with displacement current measurement are used to investigate the dynamics of polarization reversal in ferroelectric capacitor structures. In the first part, the structural and electrical signatures of polarization reversal in a $Pb(Zr_{0.2},Ti_{0.8})O_3$ ferroelectric layer under an external field is investigated from sub-coercive to above-coercive fields. This study provides the opportunity to understand ferroelectric domain dynamics under different applied electric field strength. The influence of domain multiplicity on the film structure is evidenced via the Bragg peak width and intensity.

In Chapter 2, basic notions of ferroelectricity are introduced. The properties of the different ferroelectric compounds used in the course of this work are concisely outlined. The different measurement setups used to investigate these ferroelectrics are described in Chapter 3 with an introduction to Sawyer-Tower electrical measurements and some principles of X-ray generation. The simultaneous electrical and X-ray diffraction observation of polarization reversal in a $Pt/Pb(Zr_{0.2},Ti_{0.8})O_3/SrRuO_3$ capacitive structure is reported in Chapter 4. An approach to quantify polarization domain and switching efficiency by comparing the structural dynamics under different fields strength is introduced in Chapter 5. Chapter 6 covers the frequency-dependent structural and electrical dynamics in $Pb(Zr_{0.52},Ti_{0.48})O_3$ ferroelectric layer sandwiched, in one case, between same, and in the other, two different electrode materials, respectively. The effect of an additional external resistor between the power supply and the ferroelectric device on the switching dynamics is also presented. In Chapter 7, first the structure of $BiFeO_3$ is studied statically and the peak splitting due to the change of the domain structure is shown. In a second step, its electromechanical response under different electrical pulse patterns and amplitude is examined and the presence of domain wall motion is examined. In Chapter 8 the effect on the switching transients due to the propagation of a strain wave or heat induced by a laser pulse in a $SrRuO_3$ bottom electrode through the ferroelectric layer is discussed. Finally, in Chapter 9 a discussion of the experiments and an outlook are presented.

CHAPTER 2

Background

2.1 Piezoelectricity

Piezoelectricity is defined as a linear coupling between the electrical and mechanical properties observed in some crystalline materials. When stress is applied to piezoelectric materials, an electric potential is generated. The phenomenon is termed direct piezoelectric effect (PE). It originates from the non centro-symmetry of the material's unit cell. In the absence of external bias in the paraelectric phase, the unit cell is not polarized. This is because the charges carried by its constituent atoms are balanced due to the symmetric distribution within the unit cell. When compressed or elongated, the charged atoms are either pushed further apart, or closer together giving rise to a redistribution of the charges in the unit cell. This leads to the appearance of either positive or negative electric charges on the surface of the crystal. The effect is reversible, the application of a potential difference on the crystal's surface will generate an expansion or a contraction of its unit cell, depending on the polarity of the field applied. This is known as the inverse piezoelectric effect. The magnitude of the deformation and the electric potential are related by the piezoelectric coefficient d as follows

$$\varepsilon_j = d_{ij} \times E_i \tag{2.1}$$

where E is the applied field in V/m and ε the strain.

In this thesis, we studied the longitudinal PE coefficient d_{33}, which is the one along the direction parallel to the applied field. The sign of d depends on the direction of the applied field. PE materials possessing reversible spontaneous electric polarization are known as ferroelectrics.

2.2 Ferroics

Ferroic order encompasses ferroelectricity, ferroelasticity, and ferromagnetism. Ferroics are characterized by physical changes that occur below a certain transition temperature. In the case of ferroelectrics (FE), a permanent electric dipole develops below the so-called Curie temperature T_C. Above T_C, the material is not polar due to the centro-symmetry its structure presents. This phase is referred to as the paraelectric phase. Below T_C, the orientation of the spontaneous dipole formed can be reversed back and forth by applying a cyclic electric field to the FE material, giving rise to a polarization-electric field hysteresis loop, which is exemplary displayed in Figure 2.1. The manifestation of the hysteresis loop in materials has been used as evidence of ferroelectricity in many systems [22, 23, 24, 25] .

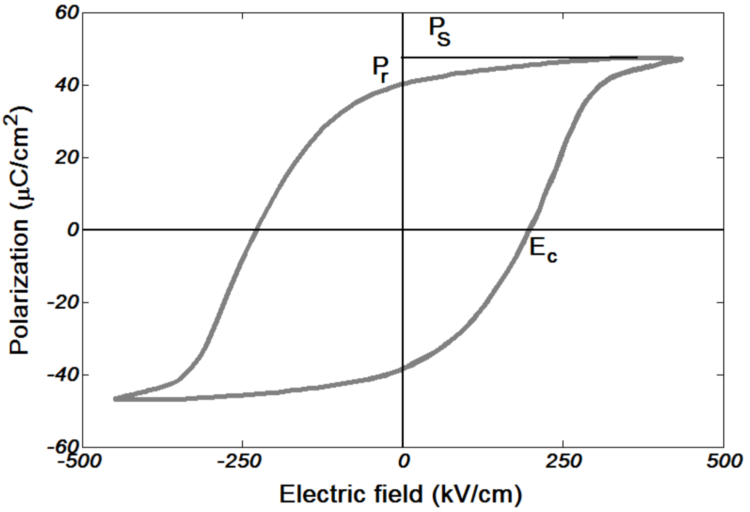

FIGURE 2.1: Typical polarization-electric field $P-E$ hysteresis loop measured on ferroelectric materials, showing the remanent polarization P_r, the spontaneous polarization P_s, and the coercive electric field E_c.

The shape of the $P-E$ loop is similar to the shape of the hysteresis one would obtain from a ferromagnetic material for the magnetization versus applied magnetic field. From the hysteresis loop, one can read the coercive field, E_c, the field strength required to switch the macroscopic polarization, and the maximum polarization P_s.The remanent polarization, P_r, is the polarization in the material after the electric field has been removed.

It is common in ferroelectric materials that polarization is not homogeneous across the whole material volume. Regions with uniform polarization form so-called ferroelectric domains [26, 27, 28]. Ferroelectric domains are formed in order to minimize the electrostatic energy of the depolarizing fields and the elastic energy associated with the mechanical constraints to which the ferroelectric material is subjected when cooled down from the paraelectric phase [29]. The region separating differently oriented domains is called domain wall. Domain walls are labeled by the relative angle between adjacent domains dipoles. Walls seperating domains with antiparallel dipole orientation are called 180° domain walls and 90° domain walls seperate regions with mutually perpendicular dipoles [29, 30, 31]. Ferroelectric domain walls have a thickness on the order of 1-10 nm, much narrower than the ferromagnetic ones that may be about 100 nm wide [29, 32, 33, 34]. Domain walls can be moved when the material is subjected to external stimuli, and their motion depends on both extrinsic (bias) and intrinsic (material structure, defects density, strain) parameters. In Chapter 4 of this thesis, we show evidence of domain wall motion using time-resolved X-ray diffraction. A single domain state can be reached by applying a high electric field. This process, known as poling, is often applied to polycrystalline ferroelectric ceramics [35].

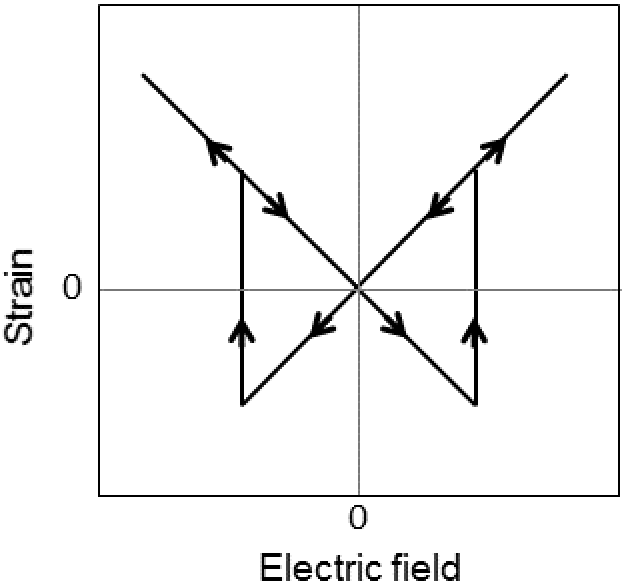

FIGURE 2.2: Schematic of an ideal electromechanical hysteresis loop

Polarization reversal is accompanied by a mechanical deformation of the crystal. Deformation along the direction parallel to an applied electric field is quantified by the longitudinal piezoelectric coefficient d_{33} as introduced before while that measured along the direction perpendicular to the applied electric field is quantified by the transverse piezoelectric coefficient. In ferroelectric materials subjected to an alternating electric field, when the applied field is anti-parallel to the polarization in the FE layer, the longitudinal PE strain ε is negative and once the polarization aligns with the applied field, the PE expansion kicks in leading to an electromechanical $\varepsilon - E$ hysteresis loop that is referred to as the "butterfly loop". This happens at the coercive field that is measured during the P-E loop.

Schematic of the electromechanical hysteresis loop for purely 180 degrees polarization reversal is shown in Figure 2.2. When the field and polarization are antiparallel, the lattice contracts. Once the coercive field is surpassed, the piezoelectric coefficient changes sign, leading to an expansive strain [29]. The switch from one polarization orientation to the other in real thin films is less abrupt than depicted in Figure 2.2 because the coercive field may vary for the different domains within the film.

2.2.1 Perovskite ferroelectrics

The materials investigated during this thesis have the chemical composition ABX_3 and crystallize in the so-called Perovskite crystal structure, named after the Russian mineralogist *L. A. Perovski*. In this structure, the A-site ions are cations and are located at the corners of the cubic unit cell. The B-site cations located at the body center as well as the A-site cations are metal ions. The X ions, which are often oxygen ions are located at the face centers of the cube as shown in Figure 2.3 for an ideal perovskite [36, 37].

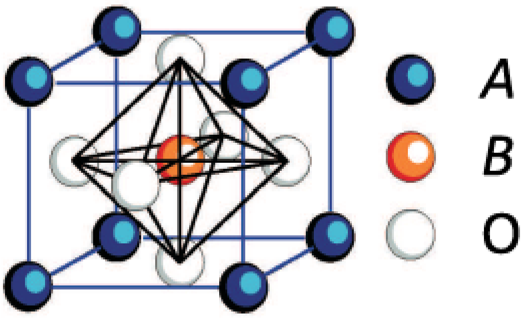

FIGURE 2.3: Ideal crystal structure of perovskite compounds, showing the different constituent atoms locations [1].

A variety of ions of different sizes can be incorporated on the different sites. To accommodate the sizes of the ions, the unit cell can contract, expand, or even rotate bond angles [38, 39, 40], resulting in materials with monoclinic, orthorhombic, rhombohedral, and tetragonal symmetry. The Goldschmidt tolerance factor, t_G, which is a dimensionless number defining how much the obtained structure deviates from the ideal cubic perovskite structure [41, 42], relates the different ionic radii:

$$t_G = \frac{r_A + r_O}{\sqrt{2}(r_B + r_0)} \tag{2.2}$$

where r_A, r_B, and r_O are the A-site, B-site, and oxygen ionic radii, respectively. For cubic structures, $t_G = 1$. Stable perovskite structures have tolerance factors between 0.78 and 1.05 [43, 44]. A t_G less than unity implies a rotation of the octahedra formed by the oxygen ions (like in $PbZrO_3$ for example with a t_G of 0.97), and t_G greater than 1 points to ferroelectric distortions (like in the case of $PbTiO_3$ with a t_G of 1.03) [45].

In this thesis, three members of the perovskite family are studied, $Pb(Zr,Ti)O_3$, $BaTiO_3$ and $BiFeO_3$. Although all of them show ferroelectric polarization, their crystal symmetry is not the same. Their respective crystal structure and properties are described in the following sections.

2.2.1.1 Lead Zirconate Titanate ($Pb(Zr,Ti)O_3$)

$Pb(Zr,Ti)O_3$ (PZT) is a solid solution phase of $PbZrO_3$ and $PbTiO_3$. Its chemical formula is $Pb(Zr_x,Ti_{1-x})O_3$ where x is a number such that $0 < x < 1$. The corners of its perovskite unit cell are occupied by the lead ions (Pb^{2+}), while the B-sites are randomly filled with the Ti^{4+} and Zr^{4+} ions. At high temperatures, PZT has a cubic unit cell and thus is paraelectric. The T_c of PZT can be varied between ∼513 K and 770 K depending on the relative composition of Ti and Zr, given by the number x [6, 46]. Such high Curie temperatures enable the integration of PZT in devices operating over wide temperature ranges. Depending on the value of x, its ferroelectric phase can present either a tetragonal or a rhombohedral distortion when cooled below T_c, with its unit cell dimensions changing accordingly. The phase diagram of PZT is presented in Figure 2.4.

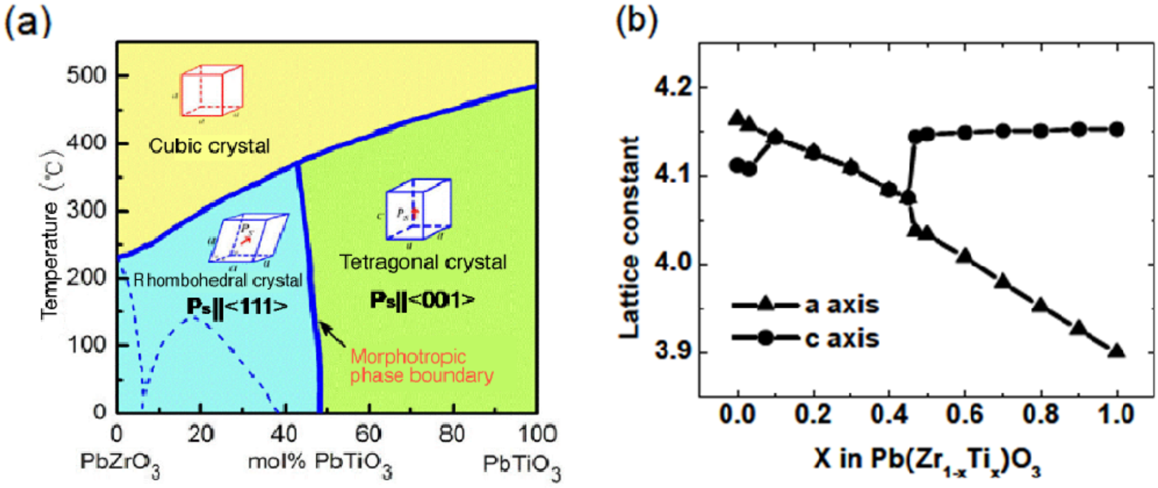

FIGURE 2.4: (a) Phase diagram and (b) lattice constants of Pb(Zr,Ti)O_3 solid solution as a function of Ti content. For each phase, the unit cell symmetry is illustrated together with the direction of spontaneous polarization P_s [2, 3, 4, 5, 6, 7].

The tetragonal ferroelectric phase is observed for the Ti-rich composition, while the rhombohedral one is observed for the Zr-rich composition. The regions separating these two is the morphotropic phase boundary (MPB) at $x \approx 0.52$. The MPB is characterized by the coexistence of the tetragonal and rhombohedral phases. As a result, the piezoelectric coefficient, dielectric permittivity, and remanent polarization increase in this region [47, 48, 49]. As shown in Figure 2.4(b), lattice parameters change abruptly near the MPB. The spontaneous polarization of PZT lies along the <001> directions in tetragonal phase, and along <111> directions in the rhombohedral phase [50, 51]. PZT films can present both 90° and 180° domain walls. Thus, its polarization reversal can happen through successive 90° steps (ferroelastic switching), or directly through 180° flipping of the dipoles (ferroelectric switching), depending on the amplitude of the applied field [52].

2.2.1.2 Barium Titanate ($BaTiO_3$)

$BaTiO_3$ (BTO) is the first simple oxide compound in which ferroelectricity was demonstrated [8, 53]. Its structure is similar to that of PZT in the Ti rich region, with barium (Ba^{2+}) ions sitting at the corners of the unit cell instead of Pb^{2+}. Its advantage over PZT is the non-toxic nature of its constituents, yet its low Curie temperature limits its operational temperature range. Also, its structure presents smaller tetragonality (c/a $\approx$ 1.01 at room temperature), smaller remanent polarization and weaker piezoelectric response as compared to PZT [54, 55] .

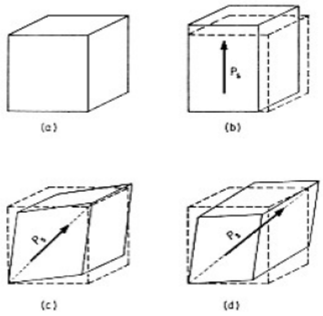

FIGURE 2.5: Unit cells of the structural phases of BaTiO$_3$. (a) Cubic, T > 120 °C (b) Tetragonal, 120 °C < T > 5 °C (c) Orthorhombic, 5 °C < T > -90 °C (d) Rhombohedral, T < -90 °C. The dotted lines in (b), (c) and (d) show the original cubic unit cell [8].

BTO exhibits three different ferroelectric phase transitions when cooled down. Its first structural phase transition is around $T_c \sim$ 120 °C,where it converts from cubic paraelectric to tetragonal FE [8]. As all the other tetragonal ferroelectrics, its spontaneous polarization points along the <001> direction, and stability is observed until about 5°C below which the transition to orthorhombic symmetry occurs with spontaneous polarization along the <110> direction. The third transition, to rhombohedral symmetry occurs below -90°C with spontaneous polarization along the <111> direction [8, 56]. The unit cell dimensions of BTO as a function of temperature is presented in Figure 2.6.

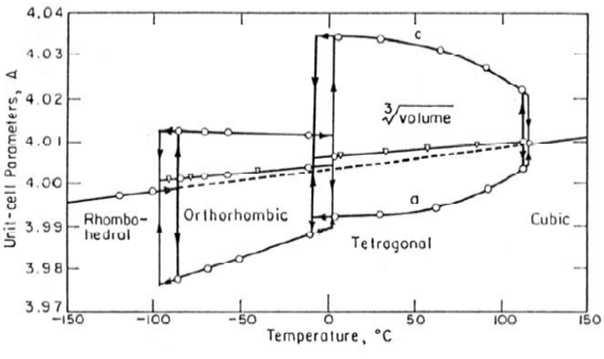

FIGURE 2.6: Lattice constants of BTO as function of temperature [8].

In chapter 8 of this thesis, electric field-induced laser-assisted switching measurements on BTO thin films at room temperature will be presented.

2.2.2 A multiferroic Perovskite: Bismuth Ferrite ($BiFeO_3$)

To date, bismuth ferrite (BFO) is the most studied room temperature multiferroic with coexisting anti-ferromagnetic, ferroelectric, and ferroelastic orders [57]. Below $T_C = 850°C$, its crystal structure presents rhombohedral symmetry, with spontaneous polarization vector P pointing along the pseudocubic <111> direction. Thus by symmetry, P can point into four different crystallographic directions of 2 different polarities given rise to eight possible polarization directions as depicted in Figure 2.7 [57, 58, 59]. The unit cell of BFO consists of Bi^{3+} ions at the A-sites of the perovskite, Fe^{3+} ions at the B-sites and O^{2-} ions at the face centers. There is increasing interest in implementing BFO in FE memories due to its reported high remanent polarization as compared to other ferroelectric materials, and the coupling between its antiferromagnetic and ferroelectric orderings [60, 61].

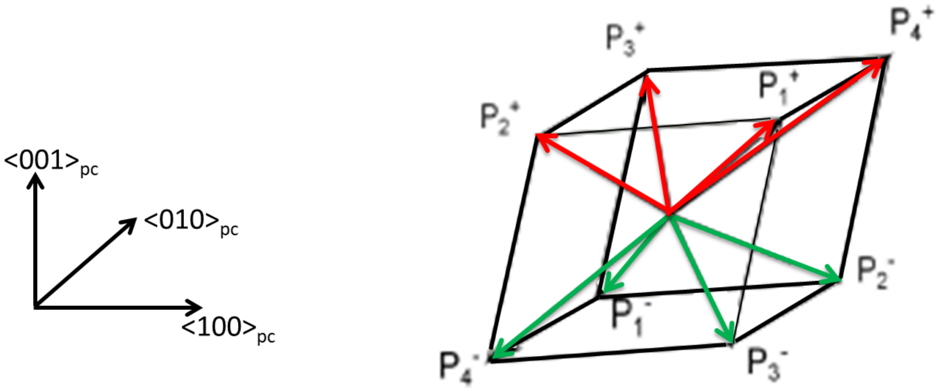

FIGURE 2.7: Schematic representation of the of eight equivalent polarization directions possible in a unit cell of $BiFeO_3$. In red the positive polarity directions (P_i^+) and in green the negative ones (P_i^-) where $P_i^+ = -P_i^-$.

Unlike in classical FE materials, the ferroelectricity in BFO has been primarily associated with the displacement of the A-site cation relative to the O along the $<111>_{pc}$ direction [62]. X-ray and neutron diffraction studies not only confirmed these findings but also pointed out that the shift of the B-site cation with respect to the oxygen octahedra is approximately four times less than that of the A-site cation [63]. The Bi ion in BFO possesses a so-called lone pair of electrons in its 6s shell. The stabilization of the rhombohedral phase below T_c is due to the the hybridization between the Bi ion lone pair and the O^{2-} p orbitals, which drives the Bi ion off-center , giving rise to ferroelectricity [62]. The magnetic order observed in BFO is associated with the 3d electrons of the Fe^{3+} cations [15]. Electric field induced polarization switching dynamics in BFO is more complex than in traditional ferroelectrics. Owing to the different possible domain walls, the structure can encompass 71°, 109° and 180° domain walls. For instance, depending on the film orientation, one can have ferroelastic 71° polarization switching between P_1^+ and P_4^+ , 109° ferroelastic switching between P_1^+ and P_3^+, and or ferroelectric 180° switching between P_1^+ and P_1^- directions as depicted in Figure 2.7 [16]. Positve (+) and negative (-) signs stand for "up" and "down" polarization states respectively. The latter switching can also occur through three sequential 71° switching steps. Since the magnetism in $BiFeO_3$ is related to the FeO_6 octahedra, an electric field applied to the layer can distort the oxygen octahedra, thereby modifying the magnetization [60, 64, 65]. The magnetization in BFO can also be modified by epitaxial strain [66] whereas the electric polarization from Density Functional Theory (DFT) calculations was reported to have a very weak dependence on epitaxial strain [67].

2.3 Ferroelectric properties

2.3.1 Dielectric constant

The dielectric constant, ϵ, is one of the physical properties of ferroeletrics that changes abruptly at the Curie temperature. It defines the ability of a material to store electrical energy and relates the polarization, P, and the electric field, E. The polarization is then given by.

$$P = \epsilon_0 \chi E = \epsilon_0 (\epsilon - 1) E \tag{2.3}$$

where χ is the dielectric susceptibility, and $\epsilon = 1 + \chi$, the dielectric constant.

In ferroelectrics, ϵ diverges at the Curie temperature and is described by a *Curie-Weiss* law [68, 69]. A schematic of the variation of the dielectric constant with temperature is shown in Figure 2.8. High dielectric constants are desirable for applications such as commercial capacitors.

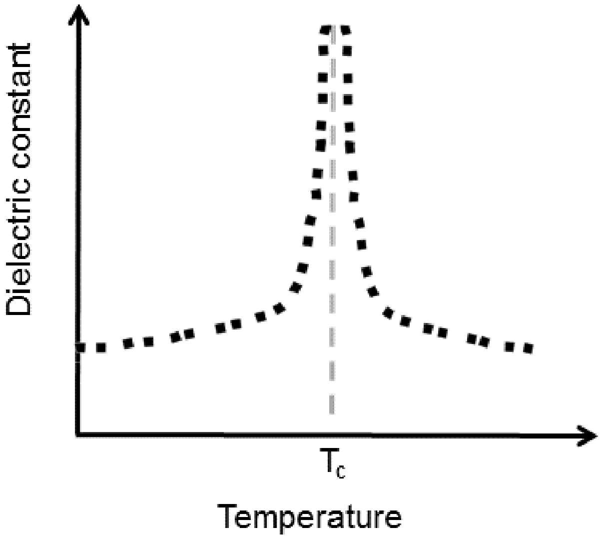

Figure 2.8: Schematic of the temperature-dependence of the dielectric constant of a ferroelectric material around T_C.

2.3.2 Polarization

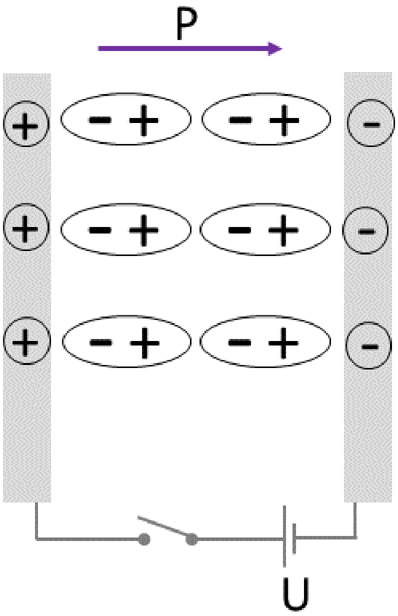

Figure 2.9: Schematic representation of a polarized ferroelectric capacitor

In ferroelectric capacitors, the spontaneous polarization creates an electric field inside the ferroelectric layer known as the depolarization field. The strength of the depolarization field is determined by the compensation of the ferroelectric polarization charges at the surface of the capacitor [70]. Figure 2.9 illustrates an electrically polarized ferroelectric capacitor with dipoles and compensation (bound) charges. When the circuit is closed, the orientation of the dipoles will depend on the polarity of the applied bias.

Landau theory

A phenomenological model to describe the phase transition to ferroelectric state was introduced by Landau [71]. Landau describes a system's equilibrium behavior based on a physical quantity that represents the system, which is known as the order parameter. In the ordered phase, the order parameter has a finite value that vanishes in the disordered phase, which is the high symmetry phase. The Landau theory was first applied to ferroelectrics by Devonshire, with the order parameter being the polarization [72]. The free energy of the ferroelectric system is expanded as a series of even power of the polarization, and can be expressed as follows:

$$F(P) = \frac{1}{2}aP^2 + \frac{1}{4}bP^4 + \frac{1}{6}cP^6 - PE \tag{2.4}$$

with the power series truncated at the sixth term, where the parameter a is proportional to temperature and is given by:

$$a = a_0(T - T_0) \tag{2.5}$$

where a_0 is a positive constant, T the temperature of the system, and T_0 the phase transition temperature. a_0, b and c are known as the Landau-Devonshire potential coefficients. c is always positive, and the sign of b determines the nature of the phase transition for the FE material under consideration. Phase transitions are classified in two categories: first and second order phase transitions.

A $b > 0$ leads to a second order phase transition at the Curie temperature T_c, while $b < 0$ yields a first order phase transition. In the latter, P exhibits a discontinuous drop to zero at the Curie temperature that exceeds T_0 and the free energy $F(P)$ shows three minima at T_c as depicted in Figure 2.11b). For second order phase transitions, P decreases continuously and reaches zero at T_c, and $F(P)$ exhibits a single minimum. The state of the system is defined by the expressing P as a function of E. To obtain this, the free energy is minimized with respect to the polarization as follows;

$$\frac{\partial F}{\partial P} = 0 \tag{2.6}$$

and setting $E = 0$, one obtains the expression for the spontaneous polarization P_0.

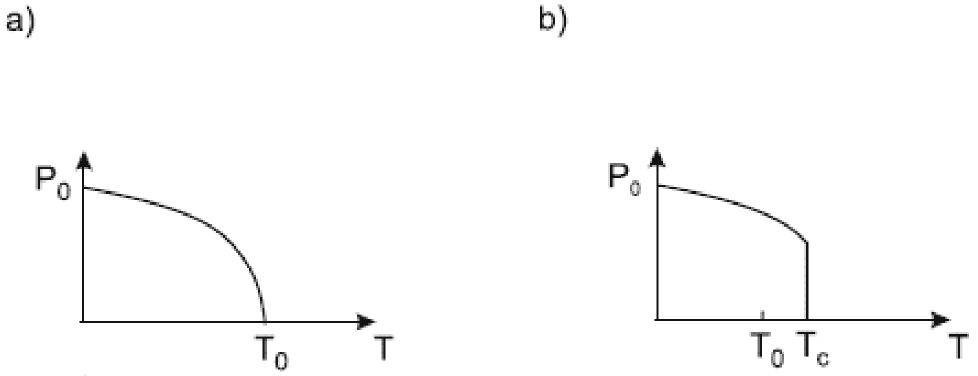

Figure 2.10: Spontaneous polarization as a function of temperature a) for a second order phase transition, $T_0 = T_c$ b) for a first order phase transition, $T_0 < T_c$ [9].

Solving equation 2.6 gives the value of the possible minima of the free energy depending on the system's temperature.

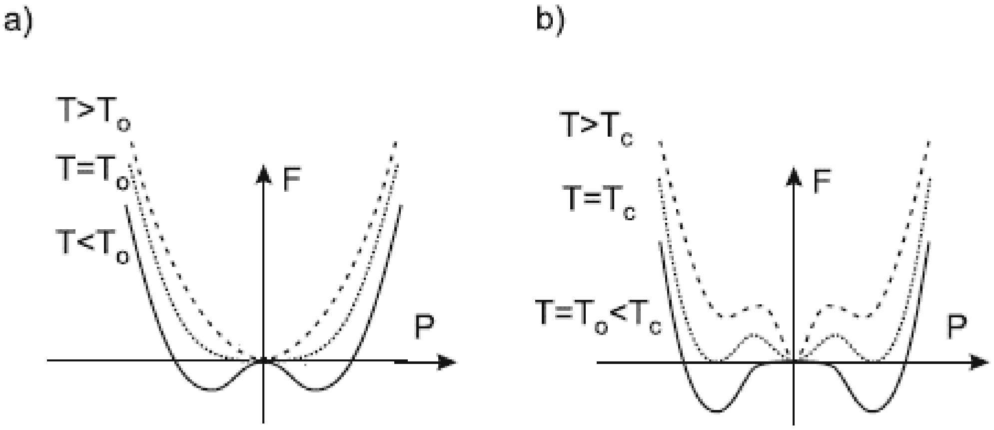

Figure 2.11: Free energy as a function of polarization a) for a second order phase transition, $T_0 = T_c$ b) for a first order phase transition, $T_0 < T_c$. The ferroelectric phase is characterized by a double well potential [9].

F for the second order transition shows a single minimum above the transition temperature (paraelectic phase) and a double minimum below (ferroelectric phase). The major difference between the two types of phase transition is manifested in the three minima observed in the first order phase transition at T_c. The free energy as a function of polarization for the different temperature ranges is depicted in Figure 2.11. Examples of ferroelectric systems exhibiting second order phase transition include PTO and PZT, while the most ancient perovskite FE BTO exhibits a first order phase transition.

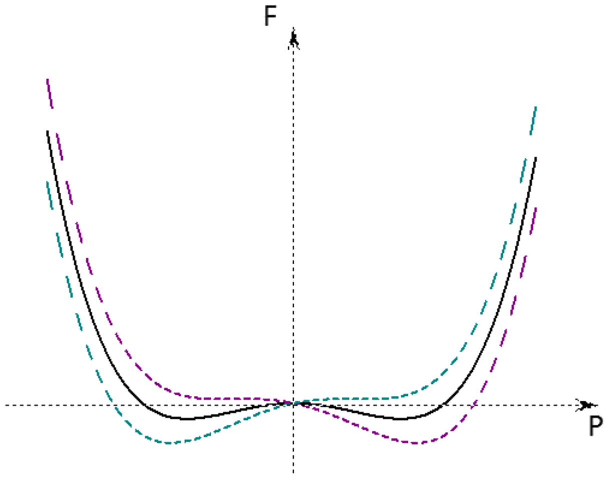

FIGURE 2.12: Double well potential shape change due to the application of an electric field. The solid line represents the case where no external field is applied.The dotted lines depict the case where a field above the coercive field is applied (purple for positive field, and dark cyan for negative field).

Phase transitions to the ferroelectric state can also be described by the "soft-mode phonon" model [73]. In displacive structural phase transitions, the B-site cation is maintained at the center of the unit cell by a restoring force at temperatures $T > T_c$. As the temperature decreases towards T_c, the phonon associated with the restoring force becomes weaker and weaker. At T_c, its eigenfrequency vanishes as the restoring forces disappear [74] and the B-site cation displaces spontaneously from the center of the unit cell to lower its energy. This leads to the new FE ground state that is characterized by the so-called "double-well potential" shown by the solid black line in figure 2.12. The strength of the resulting polarization is proportional to the relative displacement of the B-site cation with respect to the oxygen octahedra.

At zero field, the two minima in the potential energy correspond to the up and down stable polarization states. Applying an above coercive field makes F unsymmetric, depending on the polarity of the applied field. This reduces the barrier between the two minima for the switching to occur.

Polarization fatigue

Fatigue in ferroelectrics is a very important topic, especially for ferroelectric memory applications. A key attribute for memories is the ability to switch back and forth repeatedly without considerable reduction of the polarization value [75, 76]. Macroscopically, polarization fatigue is observed as reduction of the reversible polarization. A lot of work has been done on understanding the mechanism responsible for the observed fatigue in ferroelectrics [77, 78]. Its microscopic origin is mostly attributed to point defects [79] or migration of oxygen ions to the electrode-ferroelectric interface, leaving behind an oxygen vacancy that 'inhibits' the switching by pinning domain walls [20, 80]. The causes of fatigue are not yet circumscribed; they depend on the amplitude, frequency, and profile of the applied bias as well as the device preparation [20] and are sometimes accompanied by an increase of the coercive field.

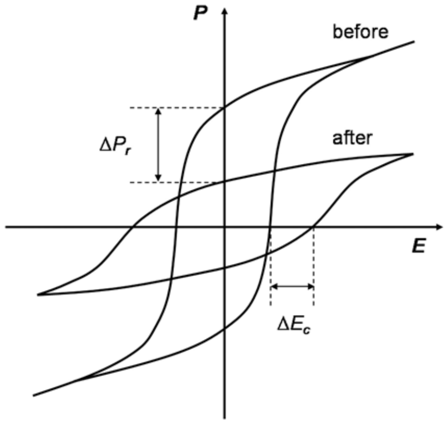

Figure 2.13: Hysteresis loops before and after fatigue of the FE, showing the decrease in polarization and sometimes an increase in coercive field, which is particular for ceramics [10].

Figure 2.13 shows an example of a hysteresis loop measurement before and after fatigue where ΔP_r (respectively ΔE_c) illustrates the decreases in remanent polarization (respectively coercive field) between the non-fatigued and fatigued film. Fatigue is mostly evaluated in-situ by measuring the polarization change after a number of switching events [81]. In past studies, Colla *et al.,* observed polarized regions with frozen domains with preferred orientation in fatigued PZT thin film in-situ during piezoresponse force microscopy studies [82]. For good FE thin films, fatigue typically sets in between 10^7 and 10^9 switching cycles [83, 84].

Other stability issues observed in ferroelectrics are leakage currents, imprint and retention loss [85]. Imprint is the preference of one polarization state to the other and is observed as a shift of the polarization-electric field hysteresis loop along the electric field axis [75, 86, 87]. Retention loss is the inability to maintain a stable (remanent) polarization state in the absence of an electric field [88, 89] while leakage currents are currents originating from mobile charge carriers such as electrons and oxygen vacancies [85, 90, 91]. Just like fatigue, leakage has been discussed to be related to defect formation and domain wall motion during switching [10, 92, 93].

Chapter 3

Experimental Methods and Setups

3.1 Electrical Measurements

Measuring electrical properties is the most commonly used technique to identify and quantify ferroelectricity in materials [29, 94]. There are many ways to characterize FE materials electrically, the most common of which gives rise to the polarization-electric field hysteresis (P-E) loop [95]. The most direct measurement of the P-E loop is based on the well known Sawyer-Tower bridge. This was first introduced in the 90's by C. B. Sawyer and C. H. Tower to measure the hysteresis of Rochelle salt [96]. The Sawyer-Tower circuit uses a linear capacitor in series with the FE capacitor under investigation [96, 97]. Cyclic voltage of appropriate amplitude is applied to the series circuit, with the FE capacitor C_{FE} built such that the field is applied along its ferroelectric axis and both the applied field traces and voltage drop across the linear capacitor C_0 are recorded through high-impedance inputs of an oscilloscope. The linear capacitor is chosen such that $C_0 >> C_{FE}$, to ensure most of the applied field drops in the FE capacitor. Since capacitors in series share the charge that moves between them, one gets:

$$Q_0 = C_0 \times V_0 = Q_{FE} \tag{3.1}$$

Then the hysteresis can be obtained by plotting the Q_{FE} per unit area against the applied field. This measurement scheme presents drawbacks such as parasitic cable capacitance due to closeness of the capacitors and charging of the sense capacitor, which results in erroneous polarization values [98, 99].

Since the essence of such measurement is to determine the surface charge density during the field cycling, it is already sufficient to measure the current flow in the ferroelectric during the cycling,

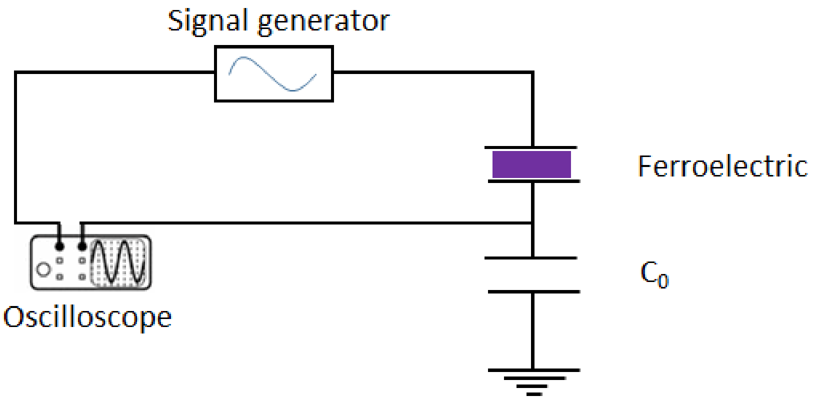

FIGURE 3.1: Schematic of the Sawyer-Tower circuit, where C_0 is the reference capacitor.

and integrating the resulting current over time, one obtains the charge flow on the device surface. Such measurement scheme can be easily implemented in a (simple) laboratory and is used during the synchrotron experiments presented in this thesis in the following chapters. An equivalent circuit of the measurement scheme is presented in Figure 3.2.

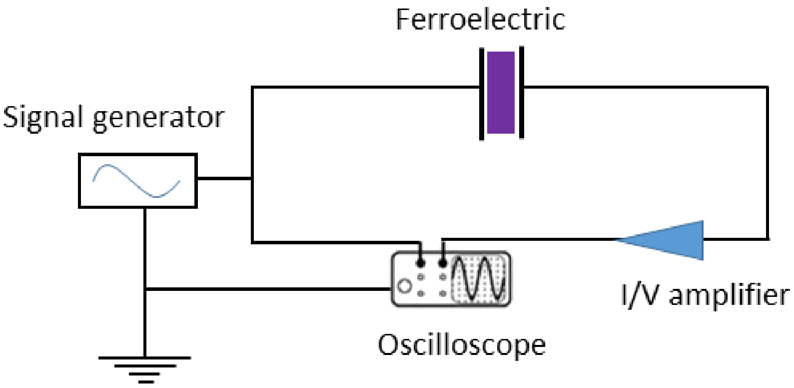

FIGURE 3.2: Schematic diagram of the electrical circuit used for measuring the FE switching current.

In our experiments, voltage pulses were generated from a function generator (Keithley, model 3390) and the output voltage was measured using an oscilloscope (Agilent, model DSO9404A). The output current from the ferroelectric is fed, if necessary, into a current-to-voltage amplifier (Femto DLPCA-200) before being recorded with high input impedance of the oscilloscope. For the case of high output current, the current-to voltage amplifier can be saturated even at its lowest gain. In those cases, the resulting current signal is measured via the 50 Ω resistance of the oscilloscope.

A typical displacement current measured from a Pt/BFO/SRO capacitor and the corresponding *P-E* loop are shown in Figure 3.3. The measured current, as displayed in Figure 3.3(b) shows a maximum at the coercive voltage.

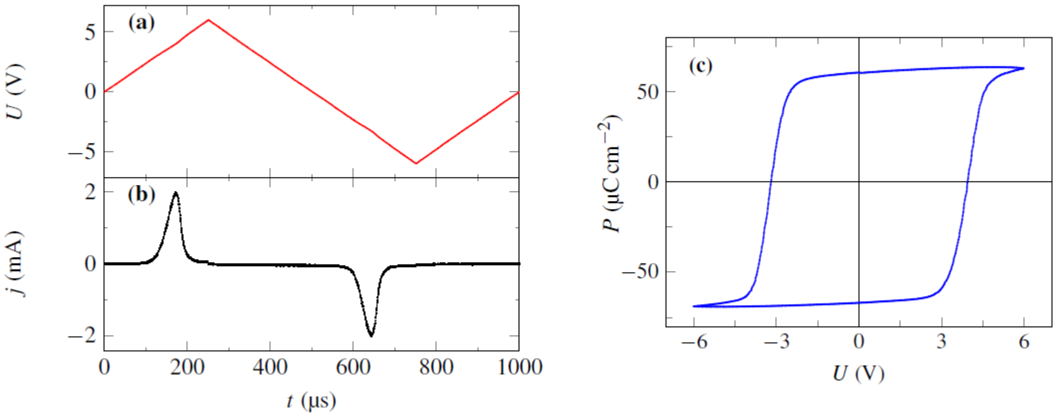

Figure 3.3: (a) Applied voltage and (b) switching current as a function of time and (c) polarization-electric field hysteresis loop obtained from (a) and the integrated current in (b).

where

$$P = \frac{\int j(t)dt}{A} \tag{3.2}$$

A is the area of the electrode and $j(t)$ the measured current. The first point in the raw data of the charge obtained from directly integrating the recorded current is zero since the current only starts flowing when the charges begin to move and to switch, irrespective of the starting value of the polarization. Thus the hysteresis loop in Figure 3.3(c) is offset up because its first point is at the origin of the graph. For symmetric devices with no imprint, the loop can be centered by averaging the positive and negative maximum polarization values from the raw data and subtracting that average from every point. Alternatively, the offset can be determined from PUND measurement that we discuss next.

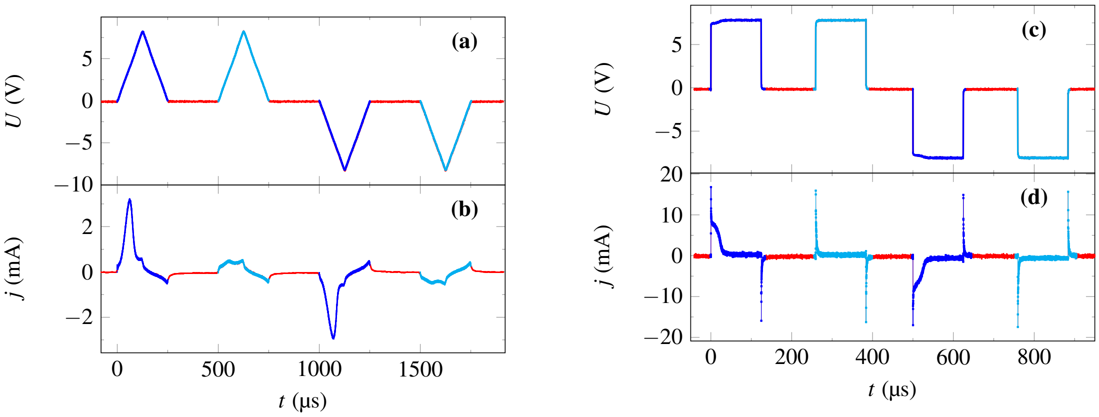

Figure 3.4: Different PUND electric pulse sequences. (a) Triangular PUND voltage pulses of 125 μs ramping time and 250 μs field-free time. (b) Switching (blue) and non-switching (cyan) currents as a function of time during the pulse sequence shown in (a). (c) Square PUND voltage pulses of 120 μs duration each separated by a 140 μs field-free time. (d) Switching (blue) and non-switching (cyan) currents as a function of time during pulse sequence in (c).

The P-E loop measured with such pulse cycling contains both ferroelectric, dielectric and sometimes leakage contributions. By measuring the current response after polarization reversal, the non-ferroelectric contributions can be subtracted and the (intrinsic) remanent polarization-electric field hysteresis loop determined. The so measured polarization is the remanent charge density due to reversal of the polarization state. This technique is known as the positive-up negative-down pulse (PUND) measurement and was initially introduced by Scott *et al.,* [100]. Its cycle is composed of four half triangular or square waves, two successive of same polarity, as illustrated in Figure 3.4(a) and 3.4(c) respectively. The first pulse (blue) reverses the polarization. The second pulse (cyan) on the other hand will not switch the sample again. It measures all other contributions to the current flow, thus resulting in less current than observed during the switching pulse. The third and forth pulses repeat the half-loop measurement for the opposite polarity, with the pulses being separated by a field-free time to get the remanence in between. Figure 3.4 shows in panel (b) and (d) the electrical response of a PT/PZT/SRO capacitor to triangular and square PUND sequences respectively.

The remanent polarization and P-E loop obtained from the latter is presented in Figure 3.5.

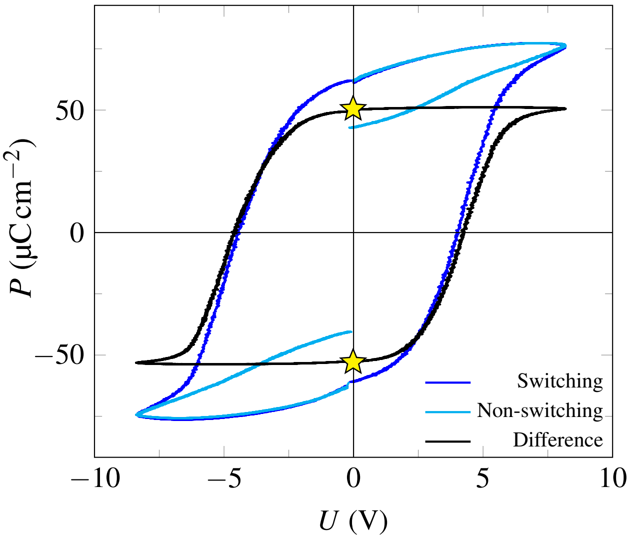

Figure 3.5: Remanent hysteresis measurement showing the switching (blue), non-switching (cyan), and remanent (black) half loops obtained from the measurement shown in Figure 3.4 (a) and (b). The yellow stars indicate the remanent polarization obtained from Figure 3.4 (d).

For each polarity, the non-switching half loops are subtracted from the switching ones in order to obtain the remanent half loop. For capacitors with leakage or imprint, P_r from the continuous single triangular pulse hysteresis measurement is not the effective remanent polarization found by the PUND measurement. A PUND sequence of square pulses yields the remanent polarization at two points on the hysteresis loop, depending on the amplitude of the square pulses. This method is particularly efficient for measuring the polarization of leaky devices [101, 102, 103, 104]. For the full switching pulse presented in Figure 3.4(c) the remanent polarization obtained from the current responses in Figure 3.4(d) is marked by the yellow stars in Figure 3.5.

3.2 X-ray diffraction from ferroelectrics

X-rays are electromagnetic waves with wavelengths ranging between 0.1 and 100 Å. High energy X-rays have the capability to pass through most objects, from human body to solid materials. When incident on solids with periodic structures, they are diffracted since their wavelength is on the order of the crystal's interatomic distances [105, 106]. Classically, X-rays are described as electromagnetic waves. From the quantum mechanical viewpoint, X-rays are considered as quantized photons with energy $\varepsilon = \hbar\omega$ and momentum $\hbar k$. The intensity of an X-ray beam is thus given by the number of photons passing through a given area per unit time, and its wavelength is related to the photon energy as follows: [107].

$$\lambda[\text{Å}] = \frac{hc}{\varepsilon} = \frac{12.398}{\varepsilon[\text{keV}]} \tag{3.3}$$

where h is the Planck constant and c, the speed of the light in vacuum. Diffracted X-ray waves can interfere either constructively or destructively depending on the path difference between them. Constructive interference is obtained for a path difference proportional to an integer of the incident wavelength, λ, as described by Bragg's law

$$n\lambda = 2d\sin\theta \tag{3.4}$$

where n is an integer, θ the incident angle and d is the distance between the crystal planes from which the X-rays are scattered as illustrated in Figure 3.6.

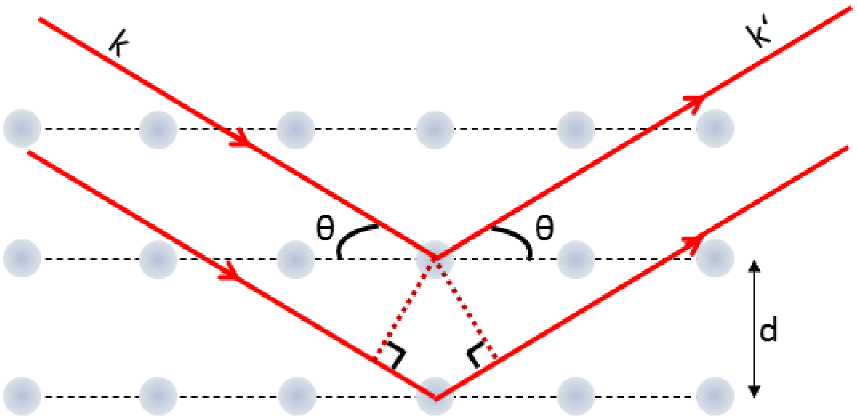

FIGURE 3.6: schematics of a periodically arranged crystal structure showing the conditions for constructive interference in real space. k represents the incident wave vector and k' the diffracted one and d the interplanar spacing.

This is referred to as the Bragg geometry. When the two waves indicated by the two rays in Figure 3.6 interfere constructively (Bragg condition given by Equation 3.4), the diffracted X-rays give rise to a maximum intensity on the X-ray detector known as the Bragg peak. From the angular position of this peak, one can calculate the inter-planar spacing. In this thesis, this is applied to determine the value of the strain experienced by the material due to the inverse piezoelectric effect.

A crystal is a periodic repetition of a constant block of atoms called the unit cell. During X-ray diffraction (XRD), each atom in the unit cell scatters the incident wave vector. The intensity and phase of the scattered wave by each unit cell can be expressed using the structure factor F, which is the sum of the scattered waves from all the atoms of the unit cell. For a diffraction along the (hkl) plane, the structure factor $F(hkl)$ is given by:

$$F(hkl) = \sum_{j} f_j exp[2\pi i(hx_j + ky_j + lz_j)] \tag{3.5}$$

where f_j is the atomic scattering factor of atom j, and (x_j, y_j, z_j) the fractional coordinates of atom j in the unit cell. f_j is a sum of the atomic form factor (f_j^0), the real part ($f_j^{'}$) and the imaginary part ($f_j^{''}$) of the anomalous dispersion for the atom under consideration [108].

$$f_j = f_j^0 + f_j^{'} + if_j^{''} \tag{3.6}$$

Anomalous dispersion results from resonant transitions within the atom [107]. The structure factor can be represented in terms of amplitude and phase of the scattered wave, and the intensity measured in XRD is proportional to the square of its magnitude ($I \propto |F(hkl|^2$).

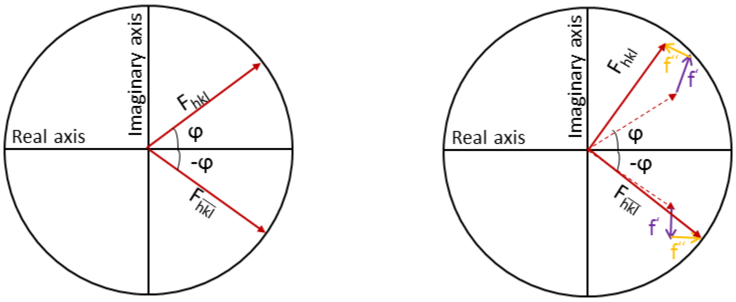

FIGURE 3.7: Argand diagram, showing the violation of Friedel's law in the presence of anomalous scattering ($f^{'}$ and $f^{''}$).

Friedel's law states that the structure factor and thus XRD intensities scattered from the planes (hkl) and $(\bar{h}\bar{k}\bar{l})$ are equal [109]. This holds only in centrosymmetric crystals and or in the absence of anomalous dispersion from the atoms, which is shown in the left panel in Figure 3.7. In the case where some atoms scatter anomalously, this condition is no longer satisfied and Friedel's law is broken. This is termed as the $violation\ of\ Friedel's\ law$. The $Bijvoet\ Difference$ gives the difference between the scattered intensities $I(hkl)$ and $I(\bar{h}\bar{k}\bar{l})$.

In ferroelectrics, this intensity difference can be used to differentiate between polarization states up or down. Reversing the direction of polarization is crystallographically equivalent to inverting the crystal plane (hkl) into plane ($\bar{h}\bar{k}\bar{l}$), thus keeping the interplanar spacing constant but not the structure factor. For a given X-ray wavelength, one can then predict the intensity difference between two polarization states by calculating the difference of the structure factor between hkl and $\bar{h}\bar{k}\bar{l}$ reflections. [110]. The anomalous scattering coefficient for each atom varies with X-ray energy. Synchrotron facilities provide high flux and variable X-ray energy, making it possible to investigate various ferroelectrics at an energy where contribution from anomalous scattering is optimal for the differentiation between polarization states.

3.2.1 X-ray sources

X-rays can be generated by accelerating electrons either in a static electric field [111, 112] or in a plasma atmosphere [113]. The earliest X-ray generation device (X-ray tube) produces a continuous X-rays spectrum (*Bremsstrahlung*) by first heating a filament to produce electrons, then accelerating them in vacuum by a high electric field (20-60 kV) onto a metal target (the anode). This continuous spectrum is superimposed by the anode material's characteristic radiation given by the element fluorescence. This process is quite inefficient since the highest fraction of the electron beam energy dissipates in the target as heat, limiting the brightness of the emitted X-rays. Moreover, the device produces long pulses of microseconds duration that are not useful for the investigation of ultrafast processes [114].

New generation light sources emit short pulses of ps duration, the extreme case are the free-electron lasers (FELs). Here, flashes of intense X-rays are emitted making it possible to study dynamical processes at femtosecond time scales with large photon number [115]. FELs produce X-rays by accelerating electrons into a linear accelerator then sending them through an undulator magnet for amplification due to the interaction between the electron beam and the periodic magnetic field [116]. The emitted electromagnetic radiation from the undulator has a wavelength inversely proportional to the square of the electron beam energy, making it easy to shorten (respectively lengthen) the emitted wavelength by increasing (respectively reducing) the electron beam energy [115]. The number of X-ray FELs facilities to date is still very small as compared to the demand, making it difficult to obtain beamtimes. Similar time resolution has been achieved with table-top laser setups.

Laser-driven plasma X-ray sources produce short X-ray pulses of femtosecond duration [117]. Laser plasma sources produce X-rays by focusing an intense laser pulse onto a metal target thus releasing the valence electrons in it, creating an ionized gas of free electrons (plasma) at its surface. These free charges are accelerated in the high electric field of the laser pulse before colliding with the underlying target to generate X-rays, similar to the process in X-ray tubes [113]. Such setup has been realized at the University of Potsdam, using a laser system with 1 kHz repetition rate and copper as target material, producing X-ray pulses of 200 fs duration. This has been successfully applied to study the ultrafast dynamics of excited solids [118, 119]. The main limitation of this setup is the poor angular resolution due to the presence of $K_{\alpha 1}$ and $K_{\alpha 2}$ characteristic radiation and the low flux of the emitted radiation. Third-generation X-ray sources address these issues.

Synchrotrons produce electromagnetic radiation by acceleration of charged particles (electrons, positrons) in a circular trajectory in a magnetic field. When the direction of these moving particles is changed (acceleration), they emit radiation. Since the particles travel at relativistic velocities within the magnetic field, the emitted radiation is at X-rays wavelength and of high brilliance. The experiments presented in this work were carried out at the XPP-KMC3 end station of the BESSY II synchrotron facility in Berlin, Germany.

3.2.2 Time-Resolved XRD at XPP-KMC3 Beamline

BESSY II is a user facility that provides photon pulses of high brilliance with wavelength ranging from terahertz wave length to hard X-rays. The storage ring BESSY II provides photon bunches of variable length (5 to 70 ps) depending on the operation mode. This limits the experiment's time resolution. Electron bunches of 1.7 GeV energy orbit around the ring at a frequency of 1.25 MHz. In standard multi-bunch hybrid operation mode, the ring current is maintained constant (top up mode) and a large electron bunch of about 4 mA is provided in the center of the 200 ns wide ion clearing gap. In the single bunch operation mode only one electron bunch is provided in the filling pattern with a bunch current of about 13 mA in top up mode. The low-α hybrid operation mode offers the shortest bunches (between 5-10 ps) but with low intensity compared to the standard operation [120]. During our experiments, the storage ring was operated in standard multi bunch mode with a ring current of about 250 mA. The high photon flux allows for detecting lattice changes down to 10^{-6} [120].

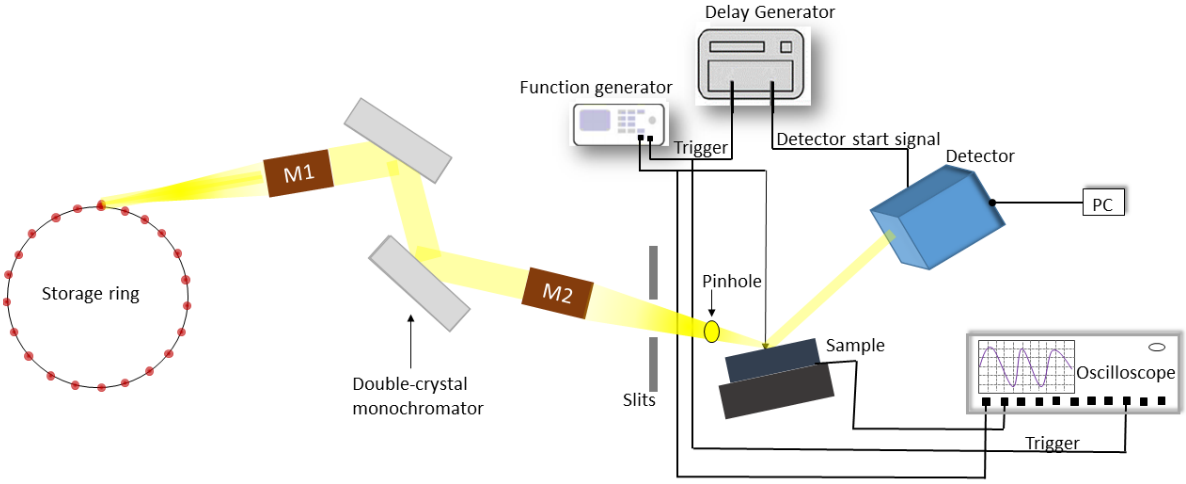

FIGURE 3.8: Simplified scheme of the time-resolved experimental setup at the XPP-KMC3 beamline at BESSY II where M1 and M2 are toroidal X-ray mirrors.

Figure 3.8 shows a schematic diagram of the experimental setup for the time-resolved XRD (TR-XRD) experiments. Electron bunches from the storage ring with energy ranging from 4 to 15 keV [121] are collimated by a toroidal X-ray mirror (M1) and directed to the double-crystal monochromator consisting of two (111)-oriented Si single crystals. The second toroidal mirror (M2) focuses the monochromatized beam onto the sample. The spatial resolution is given by the tunable beam size. The latter can be shaped by putting X-ray slits between M2 and the sample. At the XPP-KMC3 beamline, pinholes of different sizes can be used to reduce the beam spot down to 30 μm [122]. The sample sits on a four circle goniometer that allows for diffraction in Bragg geometry, with diffracted X-rays being collected with the help of an X-ray detector. Two different types of detectors are available: A fast scintillator point detector with an area of about 100 mm^2, which can be reduced by slits, and a Pilatus 100k area detector.

Detection with Pilatus area detector

To record reciprocal space maps (RSMs) efficiently, we use a two-dimensional detector (Pilatus hybrid pixel detector 100k, Dectris). It consist of a silicon module with charge readout in 195 × 487 pixels of 172 × 172 µm size each, with a read out time of a few milliseconds [123]. Each pixel works as a single photon counter. With this 2D detector, we record symmetrically and asymmetrically scattered X-rays for various angles between the incoming X-rays and the sample surface by performing $\omega - 2\theta$ scans where 2θ is the angle between the incoming and the outgoing X-ray wavevectors. Different scenarios are possible: The detector can be kept at a fixed 2θ angle and the sample rotates around an angle $\omega \neq \theta$, generally referred to as ω scan. A ω scan moves almost parallel along the $q_{||}$ reciprocal space coordinate [124]. $\omega - 2\theta$ scan with $\omega = \theta$ can be carried out by moving both the detector and the sample simultaneously, generally referred to as $\theta/2\theta$ scan. A $\theta/2\theta$ scan corresponds to a scan along the $q_\perp$ reciprocal space coordinate.

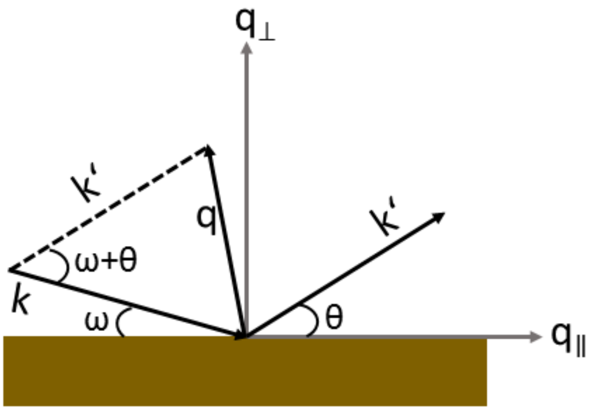

FIGURE 3.9: Schematic representation of the reciprocal coordinate system $(q_{||}, q_\perp)$ of the sample. ω is the angle between sample surface and the incoming X-rays k, and θ is the angle between the sample surface and the outgoing X-ray wavevector k'.

The following unitary transformation maps the collected diffracted intensity onto the scattering intensities as a function of the reciprocal space coordinates parallel and perpendicular to the sample surface [124]:

$$q = \begin{pmatrix} q_{||} \\ q_\perp \end{pmatrix} = k \begin{pmatrix} \cos\ \theta - \cos\ \omega \\ \sin\ \omega + \sin\ \theta \end{pmatrix} \tag{3.7}$$

where ω is the incident X-ray angle, and θ the diffracted one. Figure 3.9 shows the scattering geometry in reciprocal space with the directions of incoming and outgoing wavevectors and measured momentum transfer q. The in-plane component $q_{||}$ contains informations such as mosaicity and domain structure while the out-of-plane component $q_\perp$ is related to the lattice spacing of the measured plane by the relation:

$$d = \frac{2n\pi}{q'_\perp} \tag{3.8}$$

where n is the diffraction order and $q'_\perp$ the center-of-mass or the fitted peak position along $q_\perp$.

An area detector has a longer read out time as compared to a point detector. Thus for the time resolution, we used a point detector.

Detection with the point detector

A home made point detector made of a fast X-ray scintillator with rise time less than 0.5 ns and decay time $< 4\,\mathrm{ns}$ converts incoming X-rays into optical photons that are then detected by a photomultiplier tube (Hamamatsu). For a single 8.9 keV photon, about 100 optical photons are generated and detected by the photomultiplier (PMT). The PMT signal is sent to a time-correlated single-photon counting (TCSPC) module (PicoHarp 300, PicoQuant) via a current amplifier (FEMTO), for counting the number of events. The X-ray photon flux per bunch was small enough to prevent counting multiple X-ray photons as a single event [120, 121]. Our PicoHarp 300 module can sort signals with a maximum sort period of $33\,\mu$s thus losing a fraction of the X-ray flux when measuring at frequencies less than 30 kHz. In such case, the detector trigger is electronically shifted with respect to the first rising edge of the electric pulse and the measurement is repeated until the complete period of the applied voltage pulse is mapped.
We make use of the fast read-out of this detection system to follow time-resolved structural changes with nanosecond resolution.

Electrical connections and synchronization

To follow the electric field induced structural changes in ferroelectric materials, we apply electrical pulses of different shape, amplitude, and frequency to the FE capacitor device via the function generator (FG) model Keithley 3390, which is also used for the electrical characterization of the sample, with fast rise and fall time of $< 10\,\mathrm{ns}$ for build-in waveforms and $< 30\,\mathrm{ns}$ for arbitrary waveforms. It can provide up to 50 MHz frequency pulses and 10 V output voltage for the high impedance used in our experiment. Simultaneously to the electric field cycling, X-rays were diffracted from the surface of the device. The test device is connected from the top electrode via BNC cables to a tungsten needle of about 5 µm diameter. Silver paste was used to connect the metallic bottom electrode buffer layer to the metallic sample stage to which a BNC cable was connected to record the current flow through the device. The X-ray detector was triggered by the FG and thus recorded

X-ray diffraction intensities that could be assigned to a relative time with respect to the rise of the electrical pulse sequence. We measured in Bragg geometry using $\theta/2\theta$ scans. The time between the detector start signal and the voltage pulse is adjusted by electronically delaying the trigger signal of the detector gate with help of a delay generator (Stanford Research Systems, DG645). In this mode, the detector and the FG are not synchronized to the bunch frequency of the BESSY storage ring, hence the full output from the synchrotron is used, which includes the grass and the single bunch.

For the measurement of RSMs on the other hand, the Pilatus area detector was used. We set a measurement time window for the detector such that it records only X-rays arriving within this time interval thus neglecting a significant fraction of the X-ray flux. The detector gate, triggered by the FG, is shifted relative to the electrical pulse onset then the diffracted photons arriving the detector within its set time window are collected for the $\theta/2\theta$ scan. This process is repeated until the whole pulse period is mapped. It requires about 5 to 6 hours to measure the RSMs for a 2 kHz pulse sequence with this procedure, depending on the length of the detector measurement time window. To speed up the measurement, $\theta/2\theta$ scans with the point detector as opposed to full RSMs were measured, but then the in-plane components of the dynamics were not measured.

For the measurements with the point detector, trigger from the FG is shifted relative to the electrical pulse onset and the diffracted intensities collected at each angle θ during the scan are assigned to a time delay relative to the detector gate pulse with help of a LabView (National Instruments Inc.) software program. Our TCSPC module can only integrate signals up to 33 μs because the most coarse time resolution of 512 ps per channel results in the 33 μs time window for 65536 available channels. Thus the detector gate was shifted in 33 μs steps and the measurement was repeated untill the whole pulse period was mapped. This required about 2 hours for measuring a complete period of a 2 kHz pulse sequence.

With either detection scheme, for each point in time on the electric pulse pattern, the field was applied hundreds of times to record a complete Bragg peak. The sample is mounted on an automated XY stage sitting on the four circle goniometer in the vacuum chamber and measurements are done at room temperature. With the XY stage, the sample can relative to the fixed needle be moved in order to access a new electrical contact without reglueing the sample. Under vacuum, scattering from air was reduced and about a factor of 2 was gained in photon flux was observed at 9 keV.

Sample alignment and spatial overlap

The sample surface is aligned parallel to the direct beam by performing a half cut scan. In order to determine the lattice constant of the layers accurately, we put the direct beam onto the detector to determine the pixel of zero angular position, then align the substrate's Bragg peak to it. The samples consist typically of three layers: the top electrodes followed by the FE layer deposited on a metallic layer. This stack is deposited on a substrate typically $SrTiO_3$ or (110) oriented $DyScO_3$. The top electrodes are typically sputtered metals like Platinum or Indium tin oxide, sometimes also $SrRuO_3$. To apply the voltage to only one of the devices, defined by a top electrode and the continuous bottom electrode layer, an electrically controllable needle is moved onto a selected device by lifting the needle up and shifting the sample in-plane on the X- and Y-stages respectively (Figure 3.10). The needle is then slowly put down thanks to an electrically powered induction coil that damps the motion. The slow landing of the needle on the sample surface minimizes the scratching of the sample.

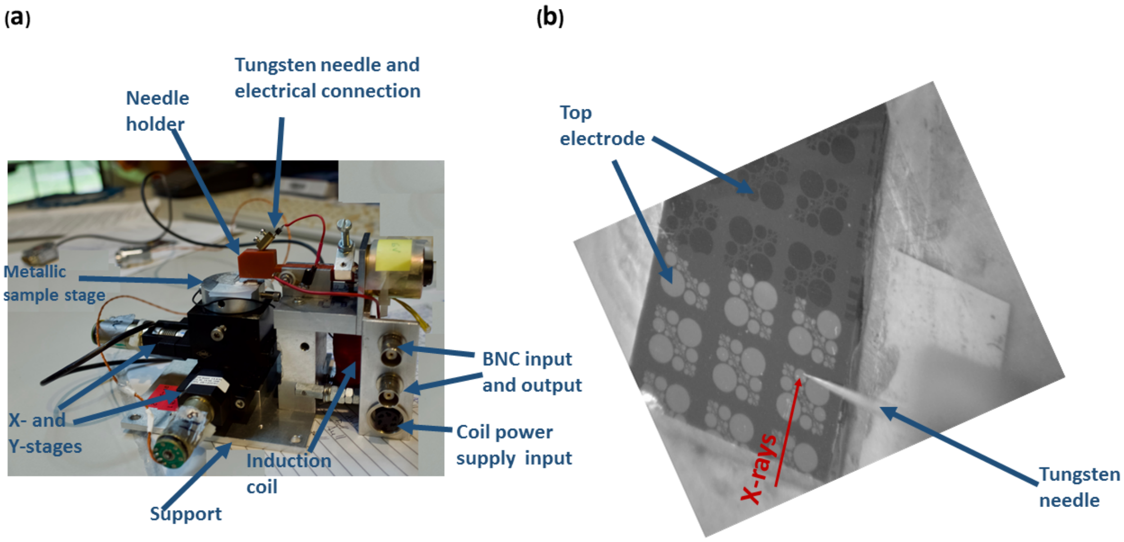

FIGURE 3.10: Photograph of the sample holder. (a) Showing the motorized X-and Y-stages, needle, sample stage, coil and electrical connections inputs. (b) Top view of a mounted sample, showing the needle on a device and the relative direction of X-rays.

Since we excite just the area under the selected electrode, it is important that the incident X-rays be aligned onto the device under bias. To ensure that, we move the incident beam close enough to the movable needle tip and record a Bragg peak of the FE layer without any excitation. Then we apply a high enough field to cause some significant PE displacement and measure the Bragg peak under the field. A comparison of these two measurements gives an idea of how far one is from the best spatial overlap position on the top electrode, since there would be little or no change in the region outside the top electrode during the field cycling. In the second step, for a fixed angle, we scan the sample surface (X and Y scans respectively) around the tungsten needle tip to get the position where the PE distortion is maximum. This will be seen as a decrease or increase in the Bragg peak intensity, depending on what side on the peak we are (LHS or RHS of Bragg peak). After these adjustments the TR-XRD measurements can start.

For the experiments presented in this thesis, unless specified, we used X-rays of 9 keV photon energy that corresponds to a wavelength of 1.377 Å where the extinction depth of X-rays is sufficiently large to probe all the layers constituting the sample but also the diffracted X-rays are sensitive to the anomalous scattering from lead and titanium ions [125, 126, 127, 128].

Data analysis and normalization

The lattice spacing change of the measured plane can be reconstructed during the field sequence via Equation 3.4 or 3.8, with θ being the center-of mass or peak position of the measured reflection. To compensate for long-term changes in the intensity of the incident X-ray beam, the collected diffracted intensity was normalized to the incoming X-rays flux from the storage ring, which was particularly important for measurements performed when the synchrotron was not operated in top-up mode.

3.3 Laser-Assisted Switching

The spontaneous polarization of ferroelectrics is most commonly reversed by application of external electric field. We want to investigate the effect of propagatiing strain through the FE layer on the spontaneous polarization direction. To achieve this, we synchronized a square electrical pulse with an amplitude below the coercive field, to a Ti:Sapphire laser system emitting 250 fs long laser pulse at 1 kHz repetition rate and measured the induced displacement current. The laser system delivers pulses at 800 nm, far below the band gap of BTO (3.2 eV [129]) and PZT (3.5 eV [130]). The laser excitation of the bottom SRO electrode layer of a test device is expected to launch a compressive wave that propagates through the FE layer and the transient change in the latter is monitored through the displacement current as the switching is mediated by the strain wave.

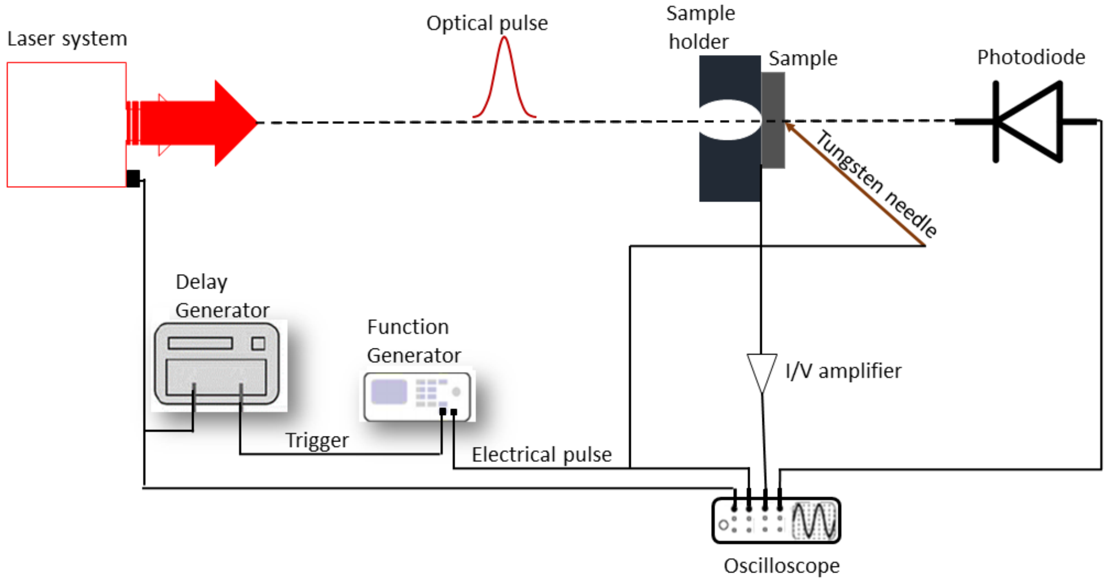

FIGURE 3.11: Schematics of the laser-assisted switching setup showing the different components and connections.

Figure 3.11 shows a schematic diagram of the experimental setup for the electrical measurement of the electric field induced laser-assisted switching. The trigger signal originating from the laser system is fed onto a delay generator (DG 645, Stanford Research System, Ltd.) which generates a trigger signal for the function generator. The function generator is operated in burst mode, thus outputs one cycle of the set waveform each time a trigger signal is received. By delaying the pulse generator trigger relative to that of the laser pulse, we can vary their relative arrival time on the sample. The arrival time of the laser (time zero) is confirmed by the photo-induced current in a photodiode placed behind the sample holder. The sample response to this simultaneous electrical and laser excitation is evidenced in the displacement current, measured by connecting the sample to a current-to-voltage amplifier whose output is then fed into the high impedance input of an oscilloscope (Figure 3.11). The latter is also triggered by the laser internal trigger signal.

Chapter 4

Simultaneous characterization of charge and structural motion during polarization switching

4.1 Introduction

The polarization reversal is one of the intriguing properties of FEs. This involves processes on the microscopic (unit cell) but also on the macroscopic (domains) level. Up to now, the complex interaction between these two scales is not completely disentangled [131, 132, 133]. A variety of experimental and theoretical techniques have been used to investigate this process, from piezoelectric force microscopy where the local deformation of a ferroelectric caused by an applied electric field with the tip of a scanning force microscope can be detected [134, 135] through electrical measurements where the change in macroscopic polarization can be detected via the displacement current (with its shape containing information about domain nucleation and growth) [136, 137], to XRD where the mechanical deformation of the ferroelectric can be assessed through the change of the crystal structure [20, 138]. Advantages of X-ray diffraction as compared to other methods include the use of continuous well-defined electrodes that allows measurements under homogeneous electric field conditions.

Electrical and structural studies have mostly been conducted independently on different devices even though sometimes grown under similar conditions. However, the strain state and domain structure can vary easily from one sample to another depending on growth condition and sample history [139], thus altering the polarization reversal dynamics and making it difficult to correlate between such individual measurements. Under external stimuli, the charge state on the surface of the FE capacitor is coupled to the domain state in the film; hence their simultaneous investigation is fundamentally useful for the understanding of the switching dynamics.

In this chapter we simultaneously investigate electrical and structural changes in a PZT-based ferroelectric test device during electric field-induced polarization reversal using time-resolved synchrotron X-ray diffraction. This provides the opportunity to correlate the real time evolution of the charge flow with the structural dynamics in the FE. We also dissociate the PE induced changes from the FE changes.

4.2 Experimental details

The sample, which is schematically shown in Figure 4.1, consists of a $\sim 250\,$nm thick ferroelectric $Pb(Zr_{0.2},Ti_{0.8})O_3$ layer grown by pulsed laser deposition on a $\sim 50\,$nm thick metallic $SrRuO_3$ bottom electrode grown epitaxially onto a (001) oriented $SrTiO_3$ substrate. The details of the deposition are described in [140]. This sample was provided to us by Marin Alexe from the University of Warwick, United Kingdom.

Hexagonally shaped Pt top electrodes with thickness of ~ 20 nm were prepared by sputtering and exhibit an edge length of 0.3 mm and diameter of 0.5 mm. The large electrode area yields a slow RC time constant of $\tau_{RC} = 1\,\mu s$ observed for charging and discharging the test device. The detailed measurement scheme is described in more detail in Chapter 3. For this part of this thesis, the structural investigations are limited to the (002) planes of PZT, SRO, and STO.

In order to ensure a complete polarization reversal during the TR-XRD experiment, electric field pulses with an amplitude far above the coercive field of the test device, which has been determined from the polarization-electric field $P-E$ hysteresis loop shown in Figure 4.2 are applied. That is, we apply fields with $U > 4\,$V but below the damage threshold in order to avoid fatigue and electrical breakdown during the experiment.

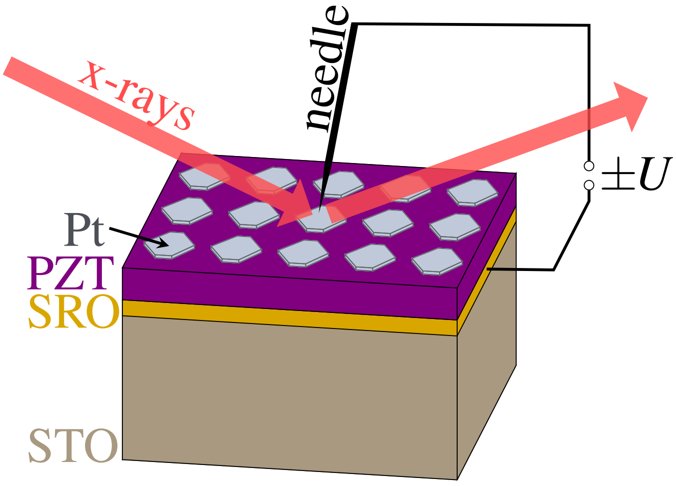

FIGURE 4.1: Schematic of the sample structure showing the stacking sequence of the different layers, connections to the external bias, and direction of the X-ray beam. The X-ray beam is focused on the electrode that is connected by the W needle.

The P-E loop measured at 4 kHz frequency under application of a triangular wave pulse of maximum amplitude ±8 V is shown in Figure 4.2. The measured displacement current j plotted in green in Figure 4.2 shows maxima around the coercive field, E_c, and the polarization reaches the saturation value P_s already at ±7 V.

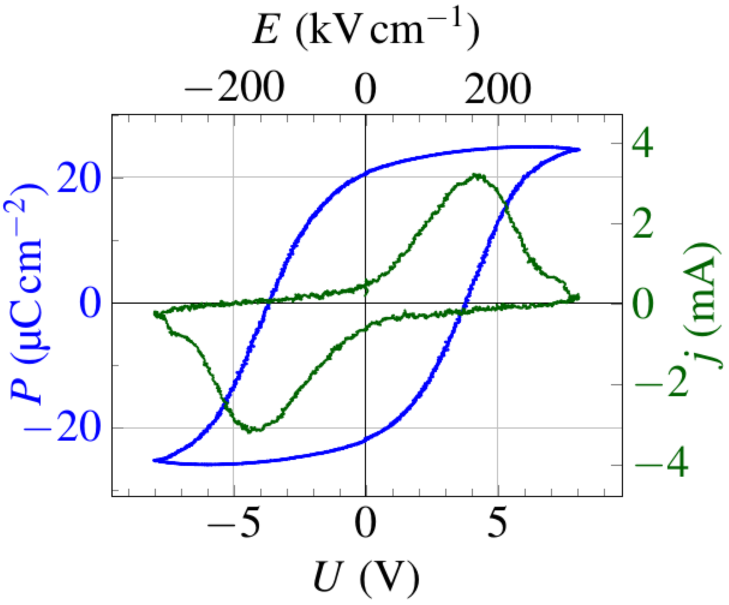

FIGURE 4.2: Polarization-electric field hysteresis loop and switching current j recorded at 4 kHz with an applied triangular voltage ramp.

The typical device lifetime of the test devices is between 10^6 to 10^9 switching cycles, which is satisfactory for the TR-XRD experiments. The time required for a complete cycle characterization was about 1-3 hours for a 2 kHz frequency pulse sequence, which corresponds to approximately 7×10^6 switching cycles per hour.

4.3 Results and discussion

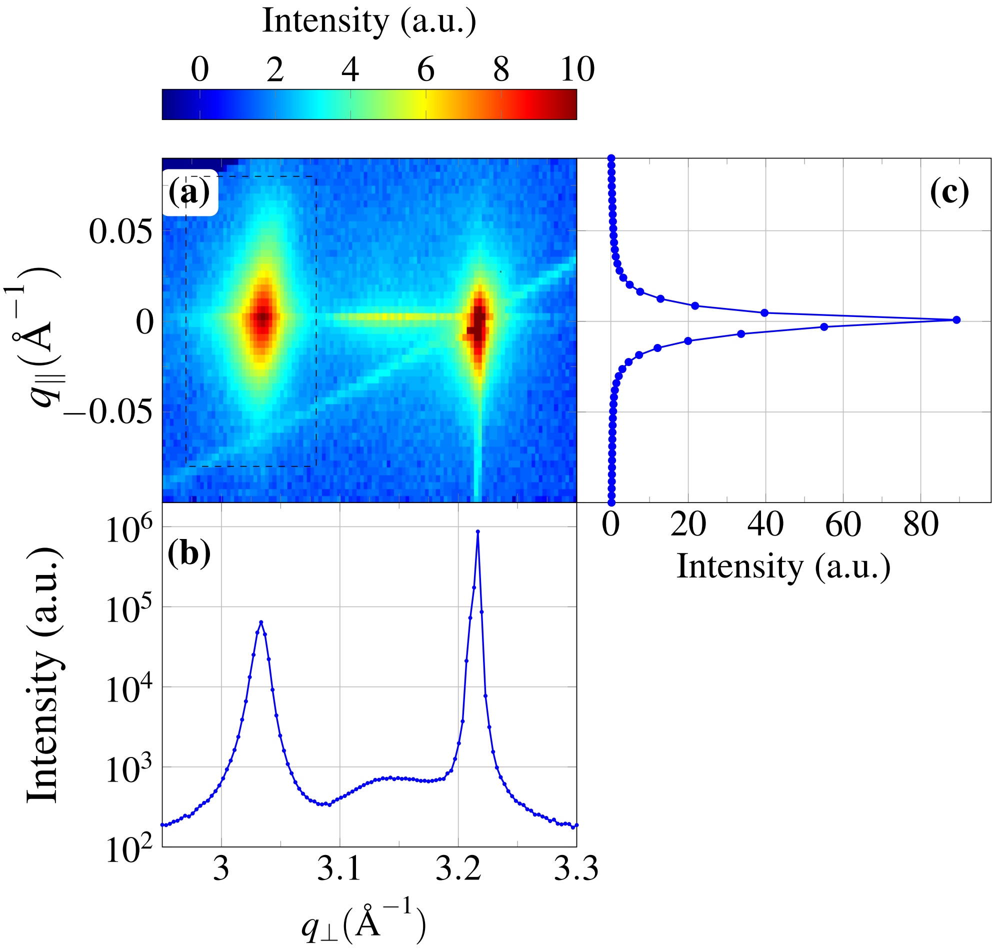

FIGURE 4.3: Static sample characterization: (a) Typical RSM around the 002 Bragg reflections of PZT, SRO, and STO of the as-grown film and substrate. (b) Line profile obtained from panel (a) at $q_{\|} = 0$. (c) Line profile obtained from the marked region inside the box of panel (a) in order to obtain the peak width of the PZT reflection.

A typical static reciprocal space map (RSM) of the pt/PZT/SRO//STO structure is shown in Figure 4.3(a). A $\theta/2\theta$ scan measured with the point detector is essentially a scan along $q_{\perp}$ at $q_{\|} = 0$. Figure 4.3(b) shows a line profile along $q_{\perp}$ extracted from Figure 4.3(a) around $q_{\|} = 0$. From the RSM, the in-plane information can be obtained by extracting the line profile along $q_{\|}$. In Figure 4.3(c) this is demonstrated for the in-plane line profile for the PZT 002 Bragg reflection by intergrating the region in inside the dotted rectangle in Figure 4.3(a). From the center of mass of the PZT peak, we obtained a lattice constant of ~ 4.143 Å.

Our operando study allows us to follow the sequence of electrical and structural events taking place during the polarization reversal of the ferroelectric.

4.3.1 Switching dynamics under a positive-up negative-down pulse sequence

A PUND pulse sequence as described in Section 3.1 of Chapter 3 was applied to the test device, and simultaneously the electrical and time-resolved structural changes were recorded as function of time, which we measure relative to the onset of the first positive-up pulse. The first positive (negative) pulse will be in the following referred to as the "switching pulse", whereas the following second positive (negative) pulse will be referred to as the "non-switching pulse", which allow to determine the charging characteristic of the investigated test device. The electrical current measurement allows us to determine the charge of the capacitor (see Section 3.1) and subsequently enables us to determine the polarization of the FE device. Our concurrently measured structural data are analyzed by the calculation of the center-of-mass that determines the Bragg peak position. The standard deviation of the peak yields what we will in the following call "peak width" of the Bragg reflection of the PZT layer.

Figure 4.4 summarizes all the simultaneously measured electrical and structural responses to the applied rectangular PUND sequence displayed in panel (a). The data presented in Figure 4.4(d) and (e) were extracted from $\theta/2\theta$ scans with the point detector while those in Figure 4.4(f) and (g) were extracted from RSM measured with the Pilatus 2D detector.

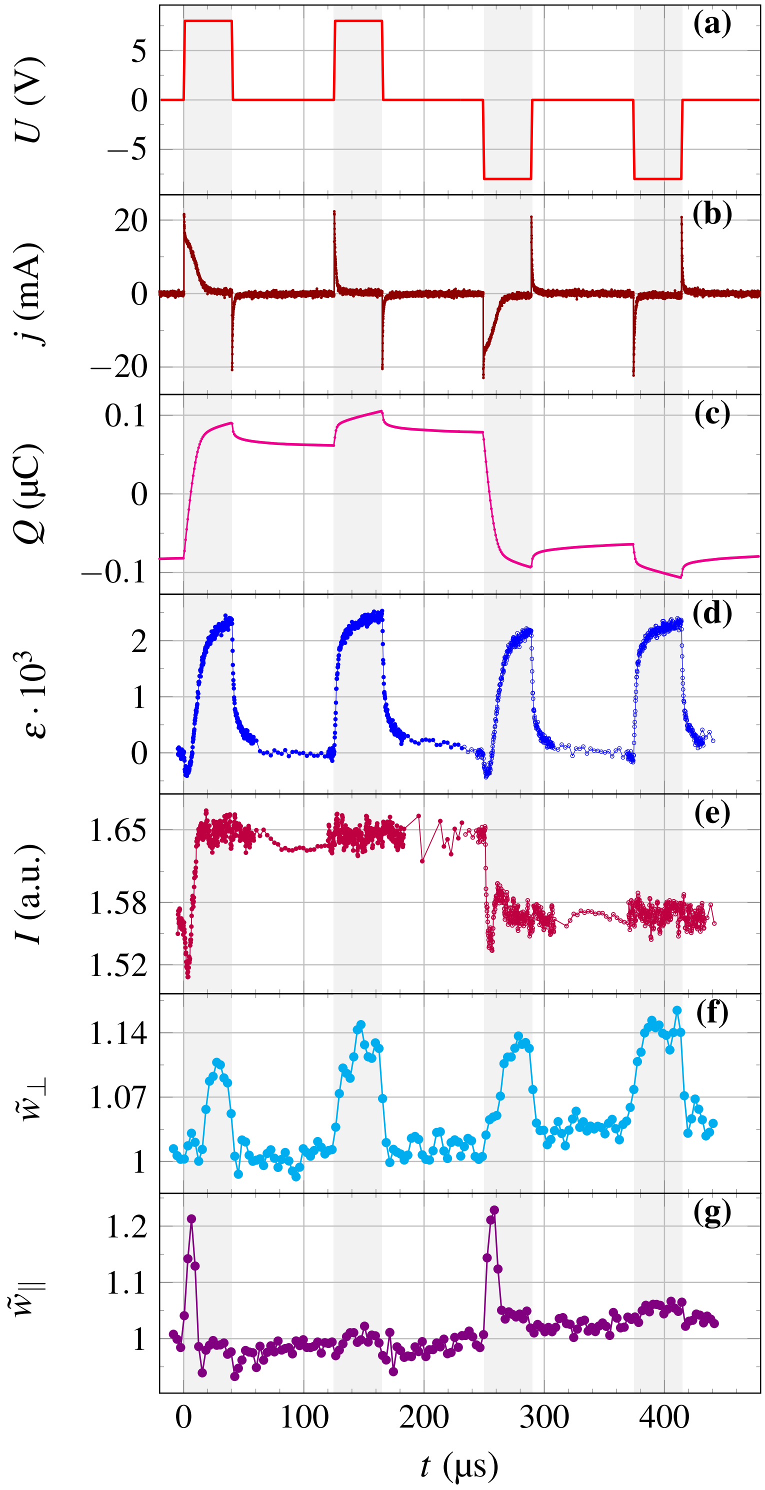

FIGURE 4.4: Device response to the applied rectangular PUND sequence. (a) Applied PUND voltage sequence $U(t)$. (b) Measured current response $j(t)$. (c) Corresponding charge $Q(t)$ obtained after integrating the current signal in (b) over time. (d) Strain $\varepsilon(t) = \frac{c(t)-c(t=0)}{c(t=0)}$ obtained from the out-of-plane lattice constant $c(t)$. (e) Integrated intensity $I(t)$. (f) Normalized FWHM of the out-of-plane Bragg peak $\tilde{w}_\perp(t)$. g) Normalized FWHM of the corresponding scattering vector parallel to film surface $\tilde{w}_\parallel(t)$.

A Maximum voltage of ±8 V was applied, which is equivalent to a maximum field strength of ±320 kV/cm. A complete PUND cycle lasts 500 μs and the individual pulses are 40 μs long. In Figure 4.4(b) the measured transient current is shown. The current rises and decays within the duration of the pulse. Leakage does not play a role in this device, since the presence of leakage would lead to a constant background in the measured current traces [103]. *j(t)* shows a fast rise within the first microsecond and an additional slower contribution during the switching pulses due to the polarization reversal. The integrated current over time shown in Figure 4.4(c) measures how much charge has flown on the device surface during the application of the pulse. From this quantity it is possible to calculate the polarization via Equation 3.2.

As shown in Figure 4.4(d) during the switching pulses, the lattice shows a fast contraction (negative ε) right after the pulse onset. The contraction lasts a few microseconds, then the the FE starts to expand once a larger volume fraction of the dipoles has been reversed. The non-switching pulses yield solely a lattice expansion that seems to be more faster compared to the expansion during the switching pulse. The slow additional strain at later times, despite the constant external field, is ascribed to domain-wall creep motion, which means that the sample is not yet in a monodomain FE state, despite the fact that the polarization is already reversed. This leads to the increasing charge flow observed in Figure 4.4(c) even when the field is constant and directly after the field is switched off. Such non-linear piezoelectric response to external bias has been reported before in references [141, 142, 143] on PZT FE samples. The integrated peak intensity *I(t)* presented in Figure 4.4(e) is a measure of the average structure factor (seee Section 3.2 and [144]). At the switching pulse onset, it shows a fast decrease and then stabilizes at a constant value. On the other hand, during the non-switching pulses, it remains constant indicating that no relative atomic displacement occurs within the unit cell. The constant *I(t)* at later times is an indication that the polarization reversal is completed within the duration of the switching pulse. The observed intensity difference between the up and the down polarization states is $\sim 5\%$ and the transient minimum shows additional $\sim 3\%$ suppression. The intensity difference between $00l$ and $00\bar{l}$ reflections can be calculated from the structure factor as discussed in Section 3.2 of Chapter 3. Considering the atomic positions for PZT listed in Table 4.1 and atomic form factors given in Table 4.2, an intensity difference of about 7% was obtained between the 002 and $00\bar{2}$ reflections at 9 keV. Calculations yield higher structure factor change when the central atom and the surrounding oxygen octahedron are displaced upwards [19, 145, 146]. This is in accordance with our measurements that show a larger peak intensity after switching the device with a positively charged top electrode.

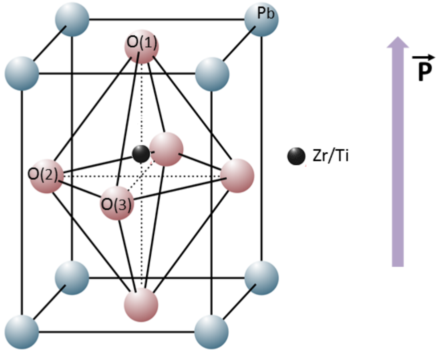

FIGURE 4.5: Schematic of the unit cell of Pb(Zr,Ti)O_3 showing the constituent atoms relative positions and direction of polarization for the case where the central atom is displaced upwards.

Ion	f^0	f'	f''
Pb^{2+}	79.858	-1.221	7.084
Zr^{4+}	35.946	3.884	1.833
Ti^{4+}	17.971	4.350	1.482
O^{2-}	5.248	2.794	0.025

TABLE 4.2: Atomic scattering factors for the ions in the unit cell of PZT for 9 keV photon energy. Taken from [11].

Atom	**u**	**v**	**w**
Pb	0	0	0
Zr or Ti	0.5	0.5	0.4517
O(1)	0.5	0.5	-0.1027
O(2)	0.5	0	0.3785
O(3)	0	0.5	0.3785

TABLE 4.1: Fractional coordinates of Pb, Zr, Ti, O atoms in the unit cell of tetragonal PZT [12].

The quantity $\tilde{w}_\perp(t)$ in panel (f) of Figure 4.4 represents the normalized FWHM of the out-of-plane Bragg peak to its value at t=0: $\tilde{w}_\perp(t) = w_\perp(t)/w_\perp(t=0)$. It shows an increase during the switching and non-switching pulses whereas the normalized FWHM of the in-plane Bragg peak ($\tilde{w}_\parallel(t) = w_\parallel(t)/w_\parallel(t=0)$) increases only during the switching pulses and decreases within $\sim 20\,\mu s$.

During the switching pulse, $\tilde{w}_{\perp}(t)$ starts to rise only after $\tilde{w}_{\|}(t)$ has already started to decrease back to its initial value. For this sample, the responses to positive and negative PUND pulses are identical, which is expected from the symmetric $E-P$ hysteresis loop shown in Figure 4.2. This symmetric behavior is remarkable, especially since the top and bottom electrodes of the device are made of different materials and hence different Shottky barriers are expected [147]: It is argued that devices with different top and bottom electrode materials exihibit an asymmetric coercivity due to the different work functions of the constituent (electrode) materials [148, 149]. The increase of $\tilde{w}_{\perp}(t)$ is associated with inhomogeneity of the PE response across the large electrode area [150, 151] . The internal field distribution across the ferroelectric layer is not homogeneous, likely due to the different distribution of domains size, defects, and screening charges.

As discussed in Section 3.1, FE contribution from the displacement current is obtained by subtracting the non-switching (up) pulse response from the switching (positive) pulse response. Just like for the FE current, we can obtain the pure ferroelectric contribution to the switching charge, the peak width, the structure factor, and the c-axis strain by subtracting the non-switching pulse response from that of the switching pulse where piezoelectric and ferroelectric responses are superimposed. The result of the subtraction is shown in Figure 4.6, where the gray background indicates the time when the bias voltage is on. Figure 4.6(a) and (b) depict the FE current $j_{FE}(t)$ and the subsequently calculated FE charges $Q_{FE}(t)$ respectively. The FE current rises instantaneously and, reaches its maximum after $5\,\mu s$ and decreases to zero after another $15\,\mu$s. Thus, after about $20\,\mu s$, the switching current stops and hence a constant $Q_{FE}(t)$ is observed. From the change of the c-axis lattice constant, we calculate the FE strain $\varepsilon_{FE}(t)$ that is shown in Figure 4.6(c). During the polarization reversal, the FE strain is purely compressive and we will show later that it also develops on a slower timescale than the PE strain. The minimum of $\varepsilon_{\mathrm{FE}}$ occurs after the maximum of j_{FE}. The FE contribution to the integrated intensity change, $I_{FE}(t)$ in Figure 4.6(d), ressembles the signal during the switching pulses in Figure 4.4(e), as the subtracted "up" pulse contribution is essentially constant.

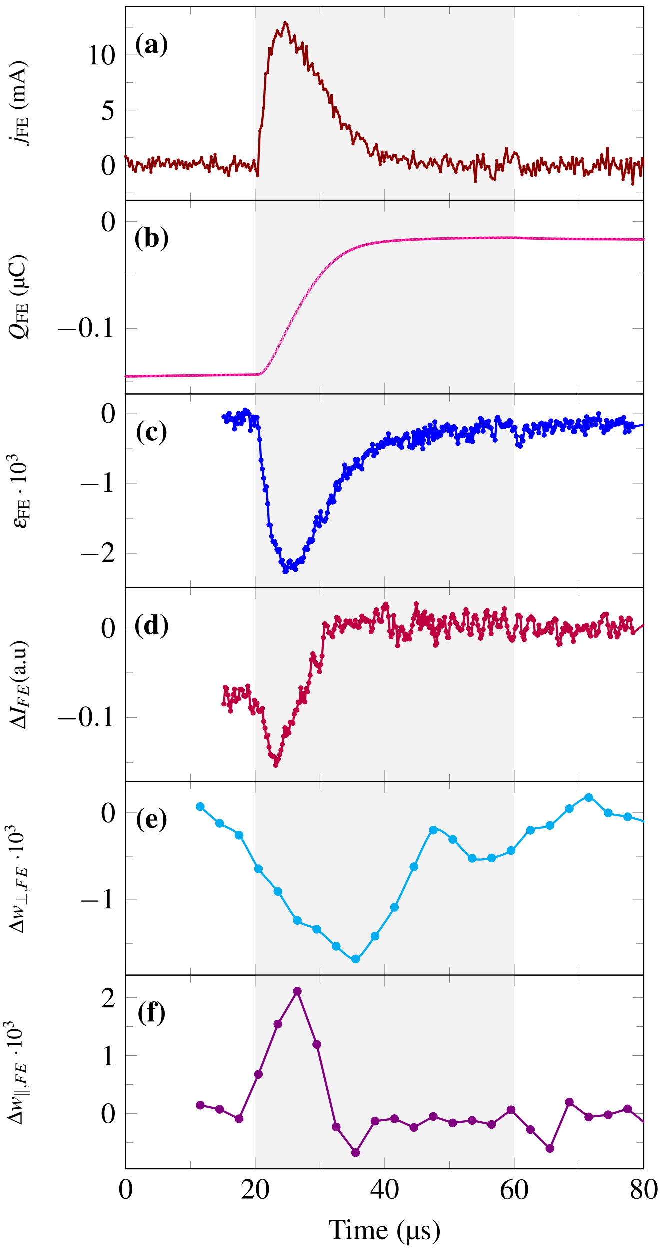

FIGURE 4.6: Pure ferroelectric response to the applied rectangular PUND sequence extracted from Figure 4.4 for the positive bias. (a) Calculated FE current response $j_{FE}(t)$. (b) Corresponding FE charge $Q_{FE}(t)$ obtained after integrating the current signal in (a) over time. (c) Strain induced by FE polarization reversal $\varepsilon_{\mathrm{FE}}(t)$. (d) Integrated intensity change due to FE switching $I_{FE}(t)$. (e) Change in FWHM of the out-of-plane Bragg peak due to FE switching $w_{\perp_{FE}}(t)$. (g) Change in FWHM of the corresponding scattering vector parallel to film surface due to FE switching $w_{\parallel_{FE}}(t)$.

The transient minimum observed here is ascribed to the transient structural disorder in the relative positions of the Ti atom and the O octahedra, analogous to the thermal disorder described by the Debye-Waller effect. The difference $\Delta w_{\perp,FE}(t)$ of the peak width change out-of-plane in Figure 4.6(e) shows a clear minimum that arises from the delay of the response of $\tilde{w}_{\perp}\ (t)$ between the switching and the non-switching pulses. Figure 4.6(f) shows $\Delta w_{\parallel,FE}\ (t)$ that rises and decreases within $20\,\mu s$ similar to $j_{FE}(t)$. $\Delta w_{\parallel,FE}(t)$ resembles the signal during the switching pulse, which confirms that this represents a purely FE contribution and can be ascribed to loss of in-plane coherence due to domain formation and domain wall motion.

Correlation between the simultaneously measured properties

In order to highlight the sequence of events during polarization reversal, we compare and interprete the main features of the simultaneously collected signatures close to the onset of the switching pulse of the PUND sequence in Figure 4.7. We restrict the discussion here to positive bias as we have discussed before in section 3.3 that the device is symmetric and the same explanations are valid for negative bias. In order to highlight that $Q(t)$ for positive and negative polarity exhibits a compensation point, we plot additionally the $Q(t)$ and $Q_{FE}(t)$ for positive bias.

Panel (a) of Figure 4.7 shows the measured switching current $j(t)$ in red color, which rises quasi-instantaneously after the application of the external bias. The dark red circles represent the FE current $j_{FE}(t)$ associated with the FE switching. The inferred charge flow is plotted in Figure 4.7(b). The solid lines represents $Q(t)$ during the positive switching pulse in red and $Q(t)$ during the negative switching pulse in blue. Similarly, the darkred circles represent Q_{FE} obtained from the positive pulse switching while the darkblue circles depict that obtained from the negative switching. As shown by the dotted lines in panel (b), the compensation point of the charges leading to the FE switching appears later than that of the total charge. The delay between these crossing points is about the τ_{RC} of our device. We attribute this to the delayed screening of the polarization charges during FE reversal.

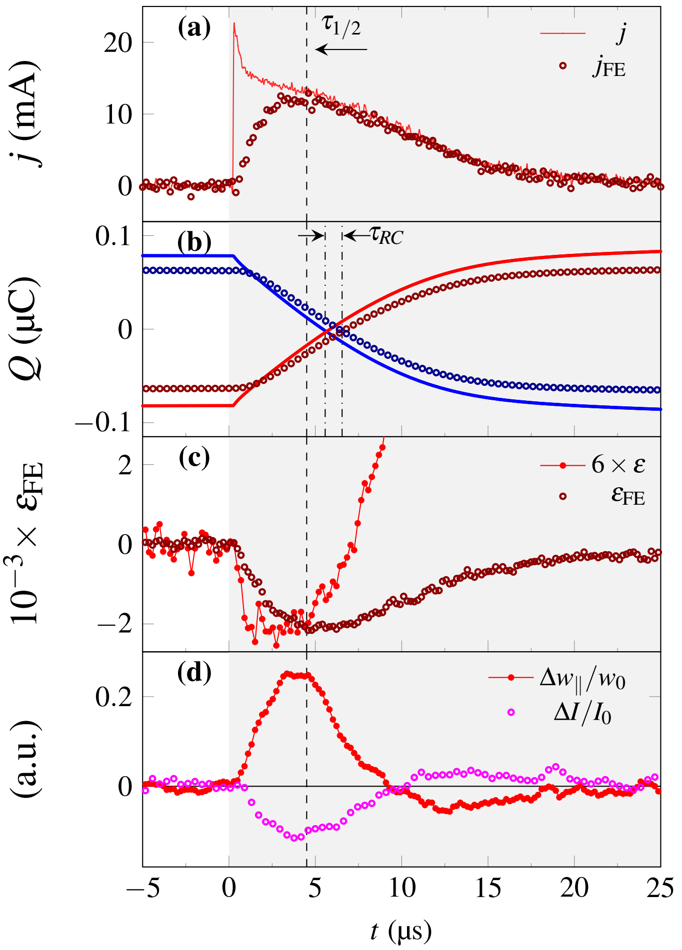

FIGURE 4.7: Sequence of events during polarization reversal. (a) Current $j(t)$ (solid red line) as measured during the polarization reversal plotted together with the current $j_{FE}(t)$ due to the FE switching. (b) The calculated charges $Q(t)$ (solid lines) and $Q_{FE}(t)$ (symbols) associated to the FE switching for positive (in red) and negative (in blue) bias. (c) The strain $\varepsilon(t)$ (filled red circles) as measured compared to the strain due to the FE polarization reversal$\varepsilon_{FE}(t)$ (open symbols). (d) Transient intensity reduction $\Delta I(t)/I(t=0)$ and transient in-plane peak width increase $\Delta w_{\|}/w_{\|}(t=0)$. The gray background defines the time when the field is on.

In Figure 4.7(c) the transient strain $\varepsilon(t) = (c(t) - c(t=0))/c(t=0)$, as obtained from Figure 4.4(d), is plotted in red together with the FE transient strain $\varepsilon_{FE}(t) = (c_{FE}(t) - c_{FE}(t=0))/c_{FE}(t=0)$ (dark red) as obtained from Figure 4.6(c). As can be seen, the compression due to the external field starts earlier than the compression due to the polarization reversal. The transient in-plane peak width change $\Delta w_{\|}/w_0 = (w_{\|}(t) - w_{\|}(t=0)/w_{\|}(t=0))$ obtained from rocking curve measurements with the point detector yields a better time resolution and is presented in Figure 4.7(d) by the red line, instead of the RSM data presented in Figure 4.4 (g), together with the peak intensity change $\Delta I(t)/I_0 = (I_{tot}(t) - I_{tot}(t=0))/I_{tot}(t=0)$ (magenta) where we define $I_{tot}(t) = I^{+}(t) + I^{-}(t)$ as the sum of the positive and negative field switching peak intensities, which is a measure of the structural disorder in the system, similar to the Debye-Waller factor for thermally induced disorder. Both $\Delta w_{\|}/w_0$ and $\Delta I(t)/I_0$ reach their extremal points at the same time.

We relate the point where the maximum compression ε due to the FE switching appears and at the same time the overall FE compression ε_{FE} of the PZT layer stops as the time $\tau_{1/2}$, which is represented by the dashed vertical line in Figure 4.7, where half of the sample volume has been switched. After this time, the PE compression turns into an expansion, and the j_{FE}, ε_{FE}, the transient peak width, and intensity begin to return to their initial values, indicating that now the coalescence of the switched domains begins.

4.3.2 Switching dynamics under a triangular ramp

The sawtooth pulse form is conveniently used to measure $P-E$ hysteresis loops. In addition, the resulting switching strain results in a butterfly hysteresis loop where the slope of the non-switching branch allows to calculate the longitudinal piezoelectric coefficient d_{33}. In the following, we will discuss the response of the PZT device to an applied a triangular pulse with 2 kHz frequency and maximum amplitude of ±8 V similar to the PUND sequence discussed in the previous section.

Figure 4.8(a) shows the applied saw pattern $U(t)$. Figure 4.8(b), (c), and (d) depict the out-of-plane lattice strain $\varepsilon\ (t)$, normalized FWHM of the out-of-plane Bragg peak $\tilde{w}_{\perp}(t) = w_{\perp}(t)/w_{\perp}(t = 0)$, and normalized FWHM of the corresponding scattering vector parallel to film surface $\tilde{w}_{\parallel}(t) = w_{\parallel}(t)/w_{\parallel}(t = 0)$, respectively. Before $t = 0$, the device has been switched by the negative half wave of the triangular pulse sequence, hence its polarization has been been completely reversed and saturated (see the $P-E$ loop in Figure 4.2). The onset of the positive pulse triggers the polarization reversal in the opposite direction, while the second half of the pulse starting at $t > 250\,\mu s$ repeats the process in the opposite polarity. The increasing ramps of the pulse reverse the polarity, while the decreasing ramps measure the PE response. At the onset of the switching ramps, the lattice shows a small contraction confirming the negative PE response at the initial stage of the switching already observed with the PUND sequence. When the field across the film reaches the coercive field, the lattice constant shows a rapid and strong PE expansion. The non-switching branches, where the field is reduced linearly to zero, result in linear PE response.

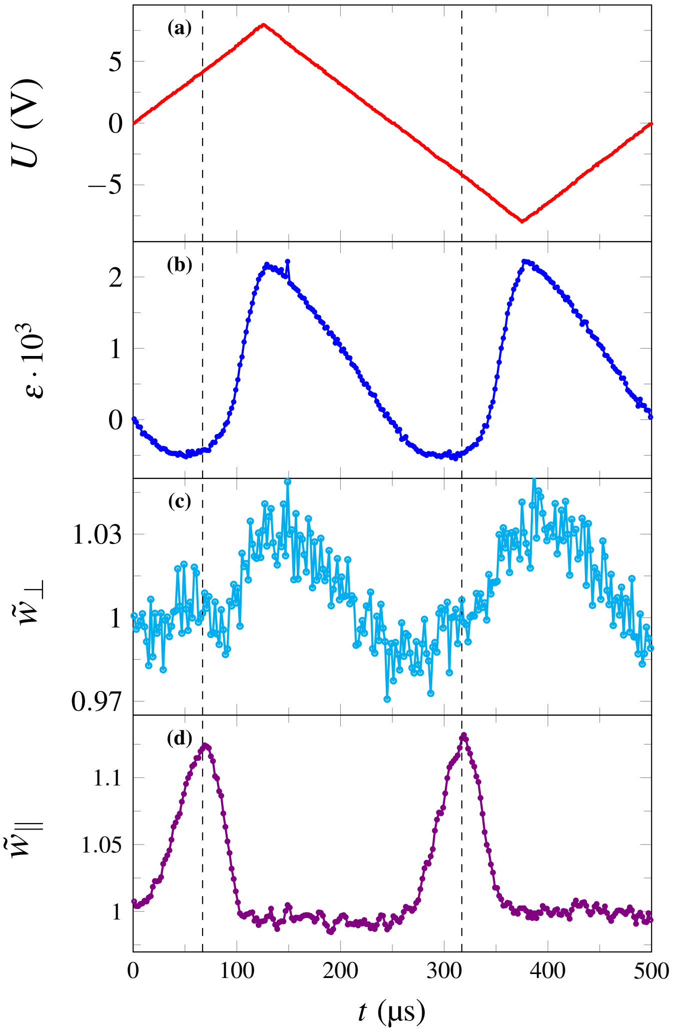

FIGURE 4.8: Switching dynamics of PZT under a triangular voltage ramp. (a) Voltage drop across the device U(t). (b) Strain $\varepsilon(t)$ obtained from the change in out-of-plane lattice constant $c(t)$. (c) Normalized FWHM of the out-of-plane Bragg peak $\tilde{w}_\perp(t)$. (d) Normalized FWHM of the corresponding scattering vector parallel to film surface $\tilde{w}_\parallel(t)$. The dashed lines mark the time t_{min} where the PE response changes sign for each polarity.

The peak width $\tilde{w}_\perp(t)$ along $q_\perp$ resembles the applied field, as soon as the coercive field is surpassed unlike the peak width $\tilde{w}_\parallel(t)$ parallel to the film surface that increases from the switching field onset. It reaches a maximum near the coercive field and then rapidly decreases as the voltage is increased further. Here again, $\tilde{w}_\parallel(t)$ stays constant during the non-switching ramp of the pulse sequence. These observations confirm the previous conclusions for the case of the polarization switching by a PUND pulse; namely that the application of the bias first leads to a fast contraction of the lattice, followed by the structural disorder seen as an increase of $\tilde{w}_\parallel(t)$. The linear change of $\tilde{w}_\perp(t)$ with the applied external field when $\tilde{w}_\parallel(t)$ starts to relax indicates that the PE strain distribution is inhomogeneous and field-dependent. The maximum PE contraction that is concomitant with the inflection points of $\tilde{w}_{\|}(t)$ observed here is larger than that observed in Figure 4.7(c) despite the lower external field ($\sim 4.1\,\mathrm{V}$ here as compared to $\sim$ 8V during the rectangular PUND). This is somehow counter-intuitive since one would expect a higher PE response with higher applied field. This effect is further discussed in Chapter 6.

4.4 Summary and Conclusion

We have simultaneously investigated the charge flow and the structural motion during polarization reversal of a PZT-based FE device. As soon as a switching bias is applied between the electrodes of a ferroelectric capacitor, it sets an electric field which adds up to the depolarization field already present in the capacitor. A piezoelectric compression about five times smaller than the observed expansion for the same field amplitude develops since the dipoles in the film are antiparallel to the applied field. This contraction is quasi-instantaneous as the PE expansion in the case of a non-switching pulse, but shows a saturation after about $1\,\mu s$ although at this time only $\sim 5\%$ of the total charge has been switched.

The screening of the ferroelectric polarization switching charges lags behind the structural response by the RC time constant of the device. This partially cancels the applied external electric field, which could explain why the amplitude of the compression is smaller than the following expansion. This is consistent with the reduction of the Bragg peak intensity as a result of lower structural order. In addition, the onset of the disorder and the onset of j_{FE} lag behind the PE contraction. In other words, the disorder and the FE switching current proceed while the potential barrier between both polarization states is suppressed by the compressive strain in the domains that are not yet switched. For the observed compressive strain of $\varepsilon_{min} = 4.2 \times 10^{-4}$ and expansive strain $\varepsilon_{max} = 2.5 \times 10^{-3}$ we estimate the modulation of the potential barrier to be 1 to 5.6 meV, based on ab-initio calculations that predict a barrier suppression from 0.23 eV for a tetragonal distortion c/a $\approx$ 1.06 to 0.1 eV for c/a $\approx$ 1 [54]. We conclude from this transient reduction of the potential barrier that the charge imbalance and the resulting strain facilitate the polarization reversal of the PZT FE device. During the polarization switching with a PUND sequence, j_{FE}, ε_{FE}, $\Delta w_{\|}$ and ΔI all have their extrema at the time $\tau_{1/2}$ that we assign to the time when 50%

of the dipoles have switched. The continuous switching arising from domain wall creep motion at later times gives rise to the additional increase of $Q(t)$ and $c(t)$ observed.

Applying a sawtooth wave confirms the interpretation of the observations with the PUND sequence. The PE response measured during polarization reversal showed intrinsic and extrinsic origins. The intrinsic contribution originates from lattice expansion or contraction of the individual unit cells while the extrinsic contribution arises from domain wall motion. The detailed comparison of the PE compression during switching with the different pulses will be discussed in Chapter 6.

Chapter 5

Investigating sub-coercive field induced structural dynamics

5.1 Introduction

The electromechanical behavior of ferroelectrics has enabled applications in transducer devices [152]. Most FE memory applications rely on the storage of the boolean algebraic logic information states "0" and "1" in the form of polarization states "up" and "down" of the FE storage layer, respectively. However, this involves the polarization reversal of the FE that promotes fatigue of the FE, limiting the device lifetime [76]. Device lifetime can be increased either by reducing the number of switching cycles during operation, or the switching field amplitude, or better still not reversing the polarization at all [153, 154]. In the latter case, one has to apply fields below the coercivity of the device. In this "sub-coercive field" regime, it is possible to induce remnant polarization states [155], which are related to the domain structure and thus lead to different piezoelectric strain [156]. This has been successfully demonstrated not only in magnetic [157, 158] but also in FE materials [159, 160]. The possibility to generate different strain states as the applied field strength is varied opens new possibilities for multi-state memories. In such devices, the remanent strain allows distinguishing between different memory states as demonstrated for a ferromagnetic test structure on a FE substrate [161, 162].

For special actuator applications requiring a precise length change, the time-dependent response of the ferroelectric layer already at low fields is important as reproducibility is paramount. In this chapter, TR-XRD experiments that have been introduced in Chapter 4, with sub-coercive field pulses are presented. The experiments are performed on the same sample used and discussed in

Chapter 4, however, a different device has been used and will be discussed below. The electric field-induced structural changes and stability of the domain structure especially after field removal are investigated at low fields as well as at high fields. In addition, an unpolarized state of the FE is realized using a "deletion pulse" as suggested in [161] and the domain state is compared with the standard switching cycle experiment.

5.2 Experimental details

Epitaxial Pb($Zr_{0.2}$,$Ti_{0.8}$)O_3 (PZT) thin film capacitors with Pt top and SRO bottom electrodes were prepared by pulsed laser deposition. Details about the sample structure were already described in Chapter 4. The evolution of the 002 Bragg reflection of PZT was monitored using X-rays of 9 keV photon energy.

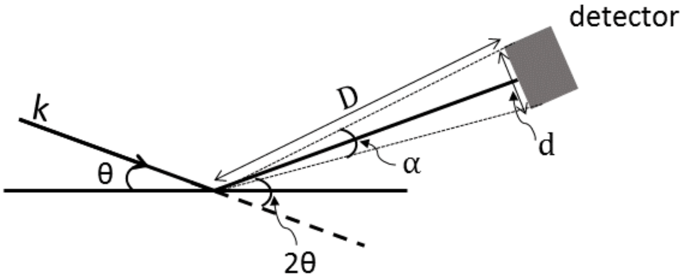

FIGURE 5.1: Schematics of the scattering geometry, showing the incident wave vector k, the symmetrically and asymmetrically scattered wave vectors, and the angles between them.

For collecting the scattered photons, the home-built point detector described in Chapter 3 placed at a distance D $\approx$ 65 cm away from the sample was used without detector slits. The detector opening, d, without slit is on the order of 1 cm, giving rise to an angular acceptance of the diffracted X-rays $\alpha = \tan^{-1}(\frac{d}{D}) \approx 0.9^\circ$ (Figure 5.1), about three times larger than the FWHM of the PZT reflection (0.3°) and thus collectting both symmetrically and asymmetrically diffracted photons even while performing a $\theta/2\theta$ scan, similar to the case where the sample is rocked. Rocking curves represent a well established method to determine the domain size of crystals and the mosaicity of thin film [163, 164, 165]. Crystal imperfections such as lattice dislocations, mosaicity and domains result in broadening of the rocking curve, which is visible from its FWHM [166]. A rocking curve around the 002 Bragg reflections of the different layers in the sample is presented in Figure 5.2.

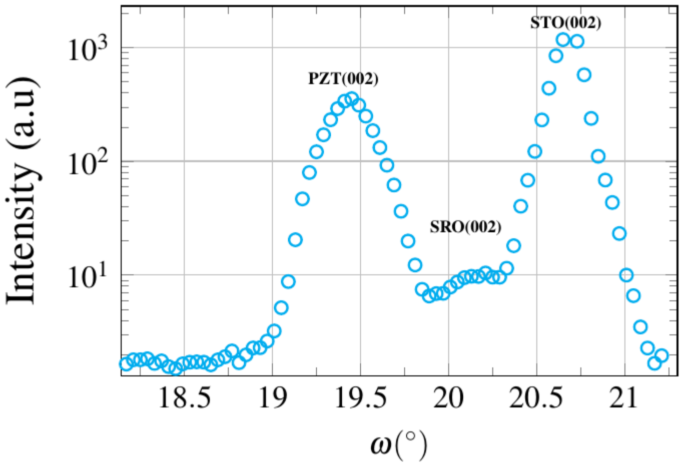

Figure 5.2: Rocking curve of the 002 Bragg reflections of PZT, SRO and STO of the as-grown film where ω is equivalent to θ in Figure 5.1.

For probing the structure at selected time delays after the "deletion pulse", an area detector was used to record full RSMs as described in Chapter 3.

5.3 Results and discussion

PUND measurements on the device used for this experiment revealed a small asymmetry in structural response between the positive switching pulse and the negative one, although the asymmetry is almost not discernible in the electrical response measured simultaneously (Figure 5.3(b)). Figure 5.3 summarizes the structural and electrical changes observed during the switching pulses of the PUND sequence, where the red trace represents positive bias and the blue trace the negative bias. In Figure 5.3(a) the measured voltage dropping across the device as a function of time is plotted, unlike in Figure 4.4(a) where the applied voltage was shown. We observe a slight reduction of the applied voltage while the strong charging and switching current flow, during the first 20 μs.

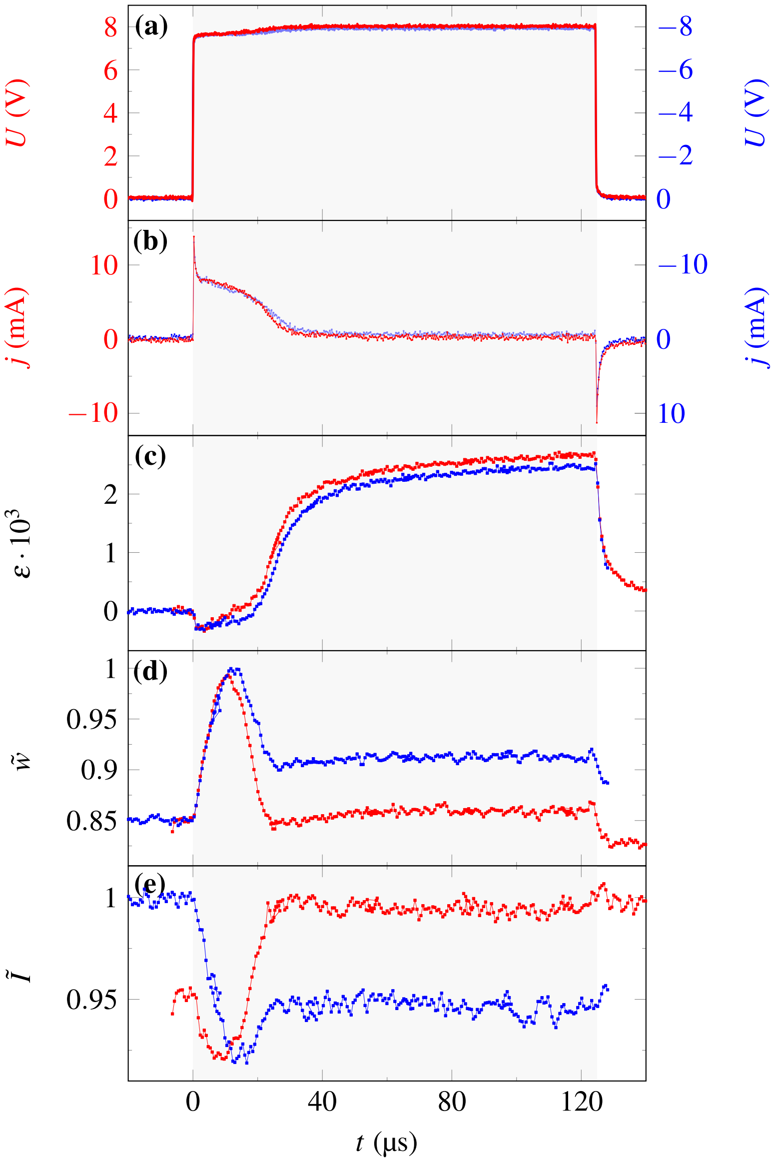

Figure 5.3: Device response to positive (red) and negative (blue) switching pulses. (a) Applied voltage $U(t)$. (b) Measured current response $j(t)$. (c) Calculated strain from the measured c-axis response. (d) Normalized FWHM $\tilde{w}$ of the Bragg reflection. (e) Corresponding normalized integrated intensity $\tilde{I}$.

The measured current displayed in Figure 5.3(b) shows that the additional charge flow due to FE polarization reversal has a slightly higher maximum and also decays earlier during the positive pulse. The strain $\varepsilon = \Delta c(t)/c(t=0)$ represented in Figure 5.3(c) shows clearly the signature of FE polarization reversal in both cases since the sign of the PE response changes from compression at the beginning to expansion at later times. Even though the maximum PE contraction is reached at the same time for both polarities, the following expansion is ~ 10 µs delayed during the negative bias resulting in an overall higher PE expansion during positive bias. The $\tilde{w}$ and $\tilde{I}$ extrema that mark the time when the disorder associated with the polarization reversal is maximum occurs about $0.5\,\mu$s earlier under positive bias. Thus, one has to keep in mind when interpreting the the results of the following experiments that in this device positive bias induces a faster polarization reversal. Such effects are often attributed to pinning and imprint.

5.3.1 Sub-coercive to above-coercive field dynamics

The coercive voltage of our device is $\sim 4.5\,$V when measured at 4 kHz with a bipolar triangular pulse (see Section 4.2). In this chapter, we investigate the dependence of the transient response of the FE layer at different field levels. Thus, temporally long square pulse sequences of different amplitude are applied, which are shown in Figure 5.4(a). We analyzed the dynamics of the 002 reflection of PZT as described in Chapter 3.

The pulse sequence consists of the electrical field pulses *P1-P4* as indicated in Figure 5.4(a). The pulses marked *P1* and *P4* of $120\,\mu$s duration are the poling pulses used to initialize the film's polarization state to "up" in a reproducible manner. Their amplitude is the same and well above the coercive field U_c of the device, however, their polarity is opposite. Although it is not always possible to fully recover the exact domain state in the FE layer because of domain wall pinning at defect sites and other imperfections, we assume that the successive application of pulses *P4* and *P1* defines comparable initial conditions for the $200\,\mu$s long pulses *P2* and *P3* whose amplitudes we vary. Pulses *P2* and *P3* also have the same amplitude but opposite polarity. Each pulse is separated from the next one by a $90\,\mu$s field-free time. The full sequence is repeated with frequency of 1 kHz. The time $t = 0$ is defined as the onset of pulse *P2*, since we are interested in the sub-coercive field dynamics.

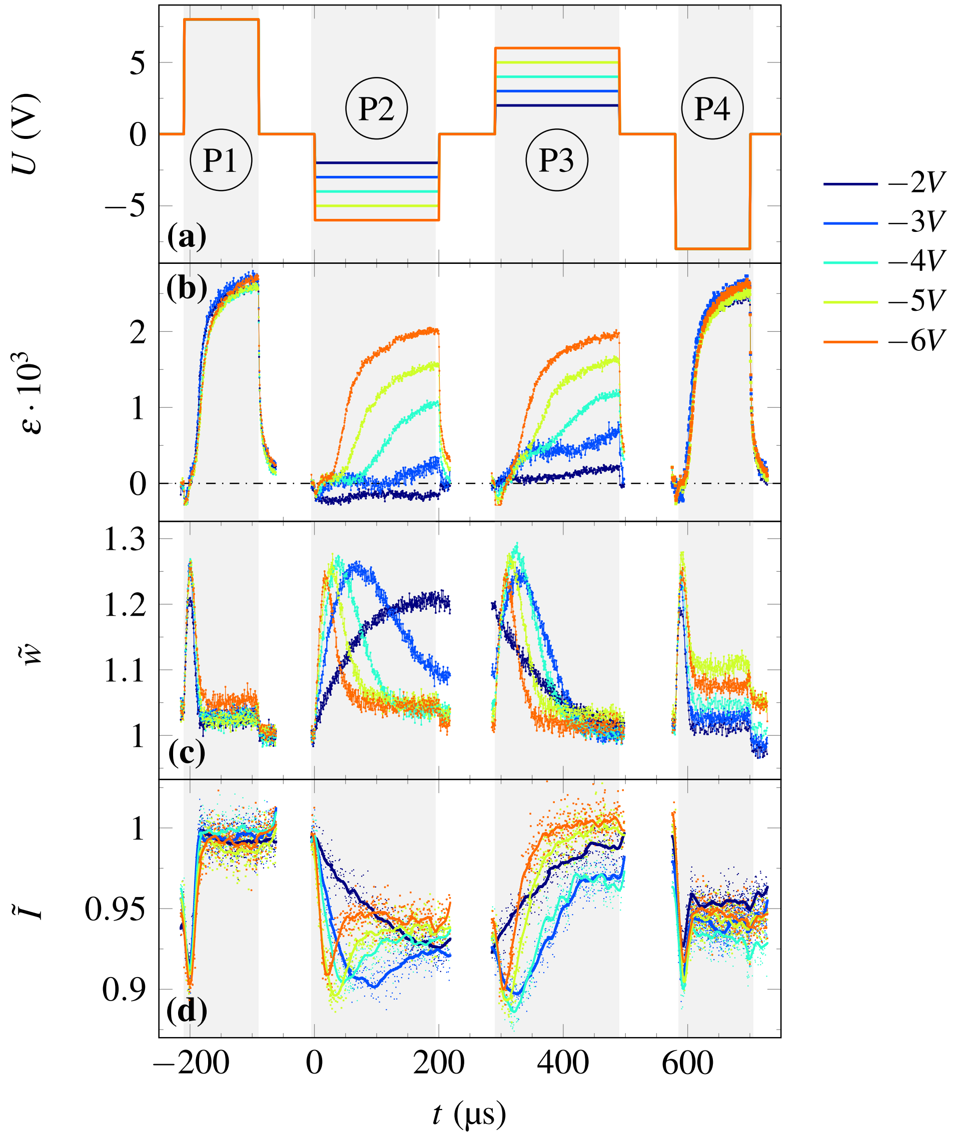

FIGURE 5.4: Time-resolved X-ray diffraction during sub-coercive and above-coercive field loading. (a) Applied waveform, (b) out-of-plane lattice response to the applied field, (c) normalized angular broadening of the measured peak, and (d) integrated intensity. The dots are the measured data and the solid lines are smoothed using a 6^{th} degree polynom.

The transient data of PZT upon the application of an electric field of ±2 V during the pulses *P2* and *P3* are represented by darkblue lines in Figure 5.4. A purely compressive strain is measured during *P2* that indicates that most of the sample under the electrode did not reverse the polarization at such low field. The simulateneous analysis of the normalized peak width $\tilde{w}$ plotted in Figure 5.4(c) shows that it increases slowly when the field is turned on and reaches saturation after about 150 μs with an overall width change of $\sim$ 20%. Note that $\tilde{w}$ stays at this value even after the field is switched off at about 200 μs and even though the strain relaxes back to zero. The increase in $\tilde{w}$ suggests structural disorder associated with the inhomogeneous nucleation and domain growth parallel to the applied field direction perpendicular to the FE layer's surface. The contributions of domain nucleation and growth is difficult to separate from our data since both take place in parallel. This is accompanied by the decrease of the normalized integrated intensity $\tilde{I}$ in Figure 5.4(d)) by $\sim 7.5\%$, much more than the 5% reduction observed during full polarization reversal. This decrease in intensity cannot be associated with the violation of *Friedel's law* since obviously only a very small fraction of the thin film has switched its polarization as indicated by the purely negative PE response. Such decrease in intensity is attributed to disorder, induced by the nucleation process. Pulse *P3* with opposite polarity is applied after a short field-free time and recovers w and I, thereby resetting the domain state in the film. The observed stability of w during the time between the electrical pulses, i.e., at zero fields, proves that the disordered domain configuration induced by sub-coercive fields is remanent and this property could be exploited for domain logic devices. In contrast, the small PE c-axis contraction, which is induced by Pulse *P2*, relaxes back to its zero-field value. Pulse *P3* with opposite polarity then leads to an expansion with similar amplitude, which is consistent with the small applied field below U_c. This leaves the majority of the FE film in the initial polarization state.

In a next step, the field strength of the pulses *P2* and *P3* was increased to ± 3 V, which is already about 2/3 of the coercive field strength of the device. The blue data points in all panels of Figure 5.4 represent this measurement. The PE response starts changing sign after $\sim$50 μs after the application of *P2*, an indication that a bit more than 50% of the thin film has reversed polarization after considerable waiting time from the pulse onset. This confirms that U_c measured during dynamic field cycling is not an absolute threshold; both the pulse amplitude and duration define the switching threshold. The transient PE strain during *P2* is accompanied by an increasing peak width w and decreasing peak intensity I at early times. Both show extrema and then slowly start decreasing (increasing) until the end of the pulse. Since $\tilde{w}$ does not yet reach its initial value at the end of *P2*, we think that the device remains in the sub-switched state by the end of this pulse. The transient strain at the beginning of *P3* confirms this reasoning since it is purely expansive. On the other hand, the still increased value of the peak width at the onset of *P3* confirms the stability of the induced domain state by *P2*. The remanent values of $\tilde{w}$ during sub-switching fields indicate stable domain states that could be exploited.

The amplitudes of the square pulses *P2* and *P3* are further increased towards the coercive field and above. As a reminder, the coercive field of PZT in this device is around 4.5 V, hence the dymanics of the FE layer is measured at *P2* amplitudes right below (4 V) and just above (5 V) the coercive field. For the data measured with an applied field amplitude of 6 V, which is well above U_c, we expect a close resemblance of the features of ε, $\tilde{w}$, and $\tilde{I}$ as we have seen and discussed in chapter 4 for similar structure and in section 5.3 for this same device with the switching field around saturation. The major difference is that for the measurements presented in this section, we now have extended the duration of the pulses to 200 μs whereas before the duration was limited to 120 μs. In standard models of polarization switching in thin films under saturation fields, the polarization reversal is mediated by the nucleation of new domains with reversed polarization, their subsequent propagation across the film thickness, and a subsequent slow lateral motion of DWs perpendicular to the field direction which finally leads to a merging of the reversed domains [167, 168, 169]. In the following, we identify these steps from our transient structural data of the FE layer. Our analysis compares the response of the sample to the pulse *P2* at different field amplitudes. Figure 5.5 shows a magnified view of the data only around *P2*. For comparison, the data obtained from a short pulse with $U = 8$ V amplitude, presented in section 5.3 where we already know that the dynamics is much faster than the $\sim 200\,\mu$s window that is required for the sub-coercive field measurements are included.

Figure 5.5(a) schematically shows the pulse waveform, amplitude and timing with respect to $t = 0$. Panels (b), (c) and (d) summarize the X-ray analysis of the structural dynamics of the PZT film during *P2* . From the measured strain, a clear evidence of switching is the sign change of the PE response but this can be observed also in the case of partial switching as soon as the switched volume is higher than the un-switched volume (see blue data in Figure 5.5(b)). However, the subsequent PE expansion is much larger under larger fields. Under high electric field, the domain nucleation and propagation is more efficient and leads to a more rapid positive PE expansion and thus the steeper and steeper gradient of the expansion dynamics for larger fields.

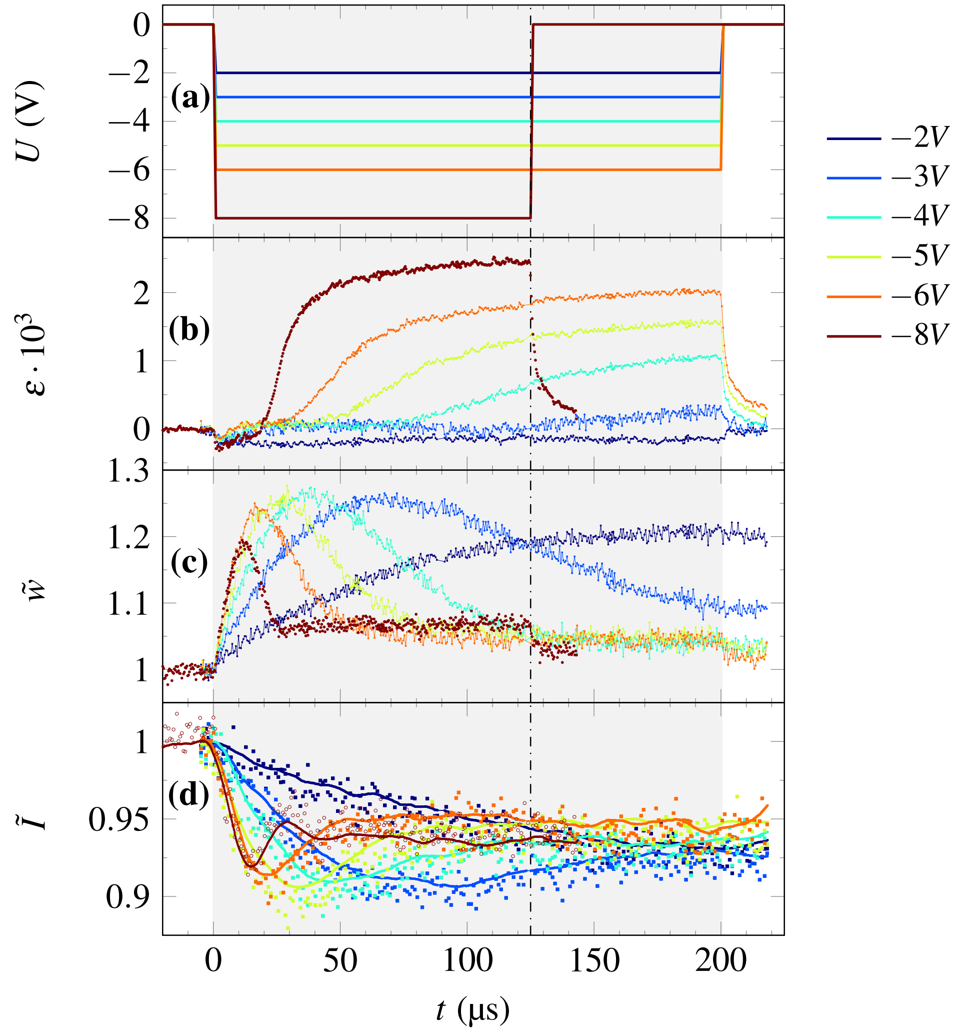

FIGURE 5.5: Time-dependent X-ray diffraction under switching pulses *P2* of varying amplitude U. (a) Schematic of the applied waveform, (b) strain due to the applied field as a function of time, (c) normalized FWHM from the recorded rocking curves, and (d) corresponding integrated intensity to its value at $t = 0$).

As mentioned earlier, the simultaneous increase of w was attributed to the structural disorder in the FE layer due to the formation of the reversed domains. For applied fields $|U_a| \geq 3\,\mathrm{V}$, the width decreases again as domains grow and merge, thus decreasing the disorder. For $U_a = -3\,\mathrm{V}$, some disorder remains when Pulse *P2* comes to an end and this disorder remains under zero field for $t > 200\,\mu\mathrm{s}$. For $U_a = -2\,\mathrm{V}$ the pulse ends in the state of maximum peak width, and also this signature of large domain disorder is remanent. A small increase of the peak width remains after switching off pulse *P2* even for the largest applied field. This indicates an inhomogenous PE strain distribution across the device even after the polarization reversal. For high fields of

$-6\,\mathrm{V}$ and $-8\,\mathrm{V}$, the normalized diffracted intensity plotted in Figure 5.5(d) confirms the expected structure factor change for full polarization reversal. However, for low field switching, the intensity decreases by more than the 5% value expected for the structure factor change. The polarization is only reversed in a small fraction of the sample and hence it is not the structure factor but rather disorder associated with inhomogeneous domain nucleation and motion that induces the intensity reduction. The time at which the peak width and integrated intensity reach their simultaneous extrema varies with the field amplitude. This is not unexpected since increasing field amplitude will lead to a decrease of the switching time due to amplification of the electrical driving force.

The significant signatures of sub-coercive field induce polarization reversal from Figure 5.5(b)-(d) were extracted and plotted as a function of the field amplitude U in Figure 5.6. The violet color data in Figure 5.6 represent the strain extracted from the c-axis of PZT at $t = 200\,\mu\mathrm{s}$. Each of the strain transients above $|U_a| \geq -3\,\mathrm{V}$ in Figure 5.5(b) shows a pronounced kink where the rate of expansion $d\varepsilon/dt$ changes. It occurs at the time t_{kink} that shows a very similar field dependence as the time $t_{\mathrm{w,max}}$ at which the maximum of the peak width is reached. The latter indicates maximum structural disorder and marks the point where reversed domains start merging. The times t_{kink} and $t_{\mathrm{w,max}}$ are represented in Figure 5.6 by the open and closed squares, respectively. $t_{\mathrm{w,max}}$ precedes the time t_{kink} of the sudden increase of the strain by a constant factor of $t_{\mathrm{kink}}/t_{\mathrm{w,max}} = 2$.

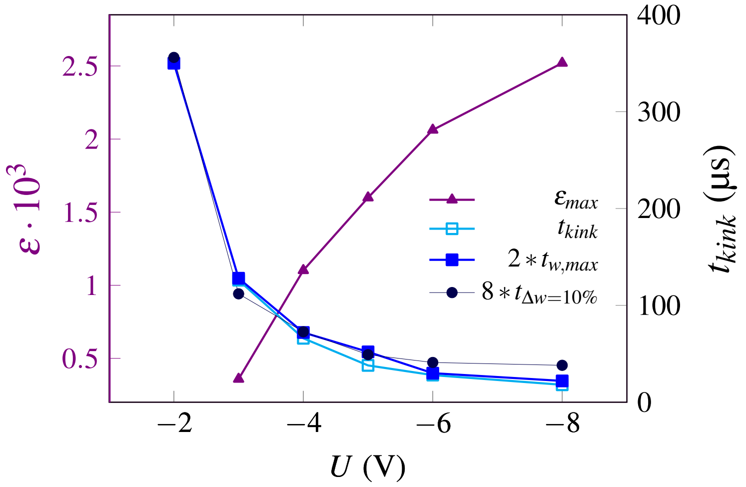

Figure 5.6: Strain ε at $t = 200\,\mu\mathrm{s}$ as function of the applied field U (filled triangles) as measure of the FE polarization extracted from Figure 5.5(b). We compare the times t_{kink} of the sudden increase of the strain (open cyan symbols) to the time $t_{\mathrm{w,max}}$ (blue solid squares) that characterizes the time when the maximum of w occurs and $t_{\Delta w,max=10\%}$ (filled black symbols) it takes to increase the peak width by 10%. The times have been scaled by appropriate parameters given in the legend.

The time $t_{\Delta w,max=10\%}$, full black circles in Figure 5.6, indicate the time after which the peak width has increased by 10% and it shows the identical voltage-dependent behavior as t_{kink} and $t_{\text{w,max}}$. Also, $t_{\Delta w,max=10\%}$ precedes t_{kink} by a constant factor of $t_{\text{kink}}/t_{\Delta w,max=10\%} = 8$.

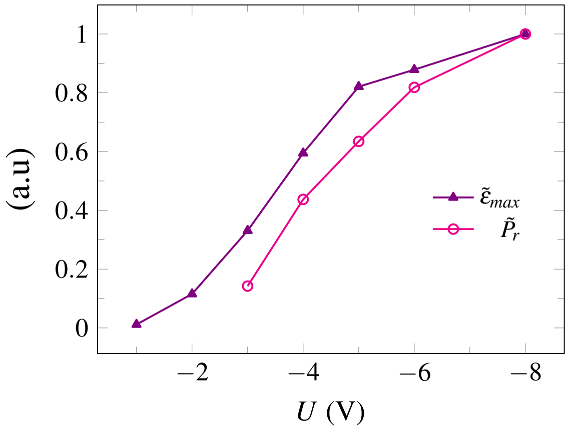

Figure 5.7: Normalized maximum strain $\tilde{\varepsilon}_{max}$ extracted from Figure 5.5 and remanent polarization $\tilde{P}_r$ from electrical PUND measurement on similar device on the same sample, as a function of the applied field amplitude.

The switched polarization P_r measured via a PUND sequence on similar device is represented by the magenta symbols in Figure 5.7. $\tilde{P}_r$ is the normalized value of P_r to its value at 8 V. Its dependence on the applied field is similar to that of the normalized maximum strain $\tilde{\varepsilon}$. This correlation confirms that the structural changes observed in TR-XRD experiments can be used to investigate the dynamics of polarization switching in ferroelectric materials and form the basis of a qualitative and partially even quantitative analysis. We interpret $t_{\text{w,max}}$ as the time where the polarization reversal speeds up because the reversed domains start merging. This reversal speed is measured by the initial slope $t_{\Delta w,max=10\%}$ of the peak width. the open square symbols in Figure 5.6 demonstrate that t_{kink} is another good indicator of the field dependence of polarization switching.

5.3.2 Domain structure and re-polarization dynamics

For technological applications, especially for the safe deletion of stored data, a "delete operation" is necessary. Delete operations without necessarily reversing the polarization of the device could reduce failiures. We have shown in the preceding sections that pulse sequences with sub-coercive field strengths can be used for creating new domains states but also for resetting the former polarization states. However, this is not equivalent to an unpolarized sample before any polarization treatment. An appropriate "erasing pulse" sequence just like that suggested by Kundys *et al.,* for recovering the strain in a ferroelectric substrate can be used to depolarize the device [161]. It is difficult to fully depolarize a FE device because of domain wall pinning and other similar effects. We investigate how such an unpolarized state upon the application of the "erasing pulse" evolves structurally in the FE. The structural dynamics during the switching pulse that followed the "erasing" sequence presented in Figure 5.8 (a).

From the measured current response in Figure 5.8(b) the surface charge flow during the positive-up pulses that followed the "erasing sequence" was calculated. As shown in Figure 5.8(c), this is about 2/3 of the charge flow measured during reversal from polarization up to polarization down state.

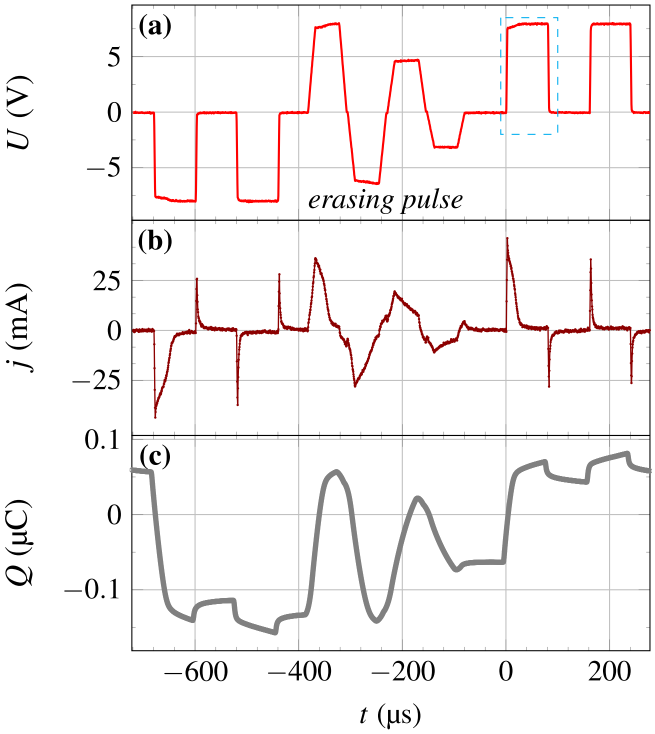

FIGURE 5.8: Electric field-induced non-polarized state. (a) Applied pulse pattern showing the *erasing* sequence. (b) Measured current response. (c) Corresponding charge obtained from integrating the current over time.

For this experiment, the 002 Bragg reflection of the PZT layer was measured as the writing pulse with 8 V amplitude shown by the cyan rectangle in Figure 5.8(a) was applied. But this time we used the area detector for this measurement, which allows to extract the time resolved RSM as explained in chapter 3. In Figure 5.9, we display the measured structural changes after the "erasing pulse" sequence was applied, in other words, the initial polarization dynamics of the FE.

Figure 5.9(b) shows the peak shift, which is only present while the electric field is applied. The absence of PE compression and also the slow increase of ε at the onset confirms the macroscopic polarization of the device was neither oriented anti-parallel nor parallel to the poling pulse.

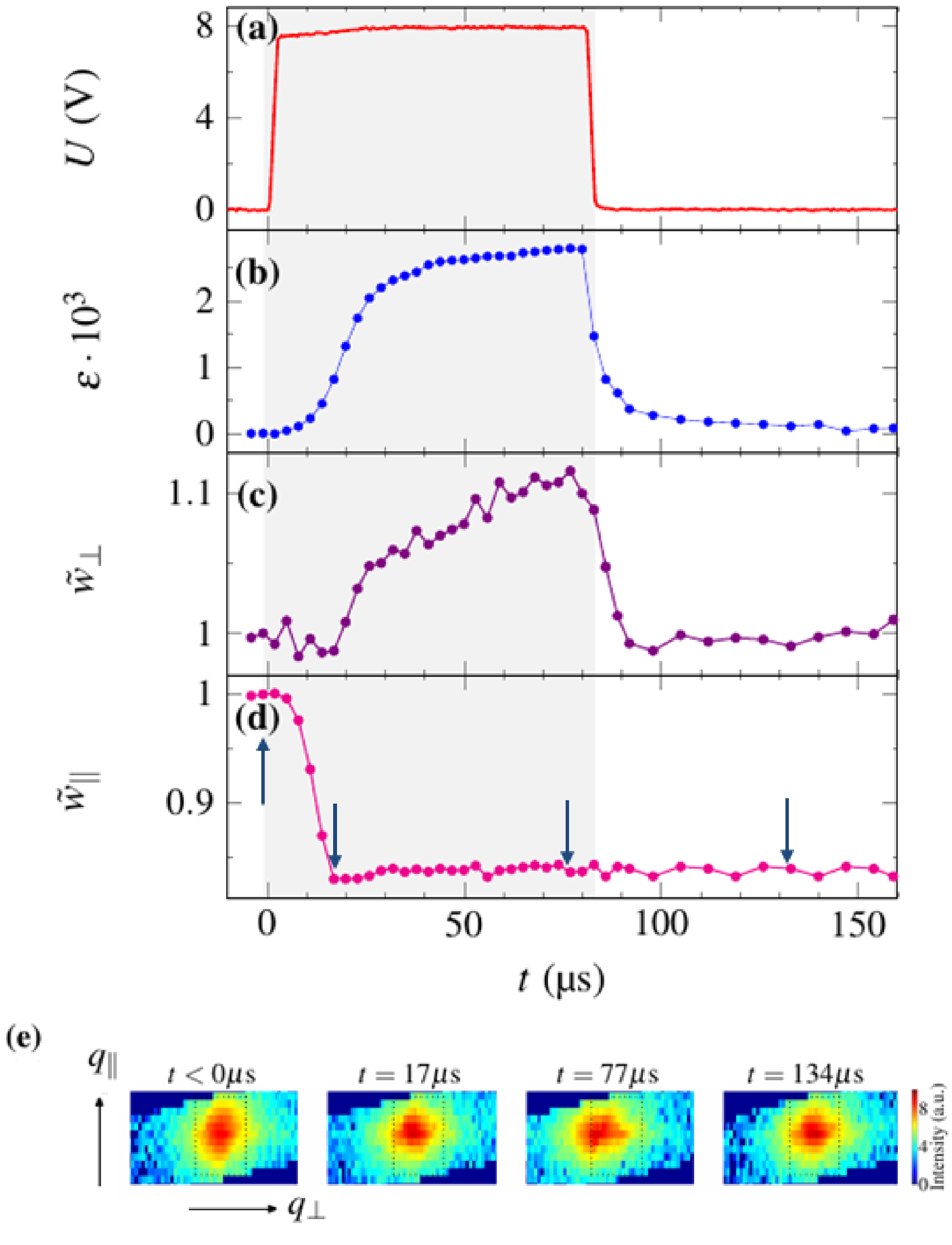

FIGURE 5.9: Device structural response to a poling pulse directly after the "erasing" sequence (cyan rectangle in Figure 5.8 (a)). (a) Voltage across the device. (b) Strain obtained form the change in out-of-plane lattice constant. (c) Normalized FWHM of the out-of-plane Bragg peak $\tilde{w}_\perp$. (d) Normalized FWHM of the corresponding scattering vector parallel to film surface $\tilde{w}_\parallel$. (e) RSMs at different times wih respect to the switching pulse. The width and the height of the displayed RSM corresponds to $q_\perp = 0.09\text{Å}^{-1}$ and $q_\parallel = 0.07\text{Å}^{-1}$ respectively. The arrows in panel (d) show the data points for which the RSMs are plotted in panel (e).

From the RSMs, the normalized in-plane and out-of-plane peak widths of PZT, labelled $\tilde{w}_\perp$ and $\tilde{w}_{||}$, respectively were extracted. Thus we can separate, for this data set disorder due to domains density from that due to change of the in in-plane coherence length. As soon as the pulse is switched on the FWHM of the in-plane component $\tilde{w}_{||}$ (Figure 5.9(d)) decreases abruptly and ε increases. The high value of $\tilde{w}_{||}$ measured after the “erasing“ sequence, before the poling pulse onset confirms high density of domains. Its decrease suggests the reduction of disorder due to domain coalescence and the concomitant increase of $\tilde{w}_\perp$ after the recovery of $\tilde{w}_{||}$ indicates the inhomogeneous distribution of strain in the device averaged over the probe area, likely resulting from imperfect screening. This latter peak width change also disappears after the external field is switched off. In contrast, the change in in-plane peak width was permanent. This is an indication that the ordering of the domain structure again is remanent and states of different degrees of disorder are stable states in the thin film. Figure 5.9(e) shows the structural changes directly in the RSM for selected time delays.

5.4 Summary and conclusion

In this chapter, we have demonstrated that sub-coercive field switching of FE devices can occur. Our experiments show that these processes are significantly slower than the switching dynamics at high field strength. The TR-XRD experiments allow to follow the domain nucleation and domain wall motion in the test structure "operando" under working device conditions. The information is contained in the transient response of the peak width of the FE material as well as the diffracted intensity. The FE polarization reversal is inferred from the sign-change of the PE response at the switching threshold. For measurements far below the coercive field, the stability of the domain structure after field removal has been demonstrated, which opens new routes for multi-level memory applications. We demonstrated that an unpoled state of remanent ferroelectric domain disorder can be obtained after the application of an "erasing pulse" sequence. Such unpoled state can be used as a reference state for multi-level data storage. Finally, the initial polarization dynamics of a FE device has been investigated structurally after the "erasing pulse" sequence has been applied. This confirmed that the erasing pulse sequence leads indeed to an unpolarized sample and opens new routes for data deletion.

Chapter 6

Lattice dynamics during dynamical electrical loading

6.1 Introduction

Saturated $P-E$ hysteresis loops measured with triangular voltage pulse provide in many cases ample evidence for ferroelectricity in materials. The main advantage of performing electrical measurements to investigate ferroelectricity is that they are easy to realize. However, some artifacts such as $p-n$ junctions and Schottky contacts at the interfaces can give rise to ferroelectric-like hysteresis loops in non-ferroelectric materials [170]. Fortunately, such artifacts can be identified by checking the frequency-dependence of parameters such as the switching current and saturation polarization [85, 170]. Ideally, $P-E$ loops are elliptically shaped Lissajous figures with the edges converging at high field towards the saturation polarization where the area inside the the hysteresis represents the energy dissipation within one cycle of domain reversal. Sample imperfections such as oxygen vacancies lead to leakage or Ohmic conduction and sometimes hinder the saturation of the hysteresis due to polarization screening and give rise to a rounded non-saturated hysteresis loop [171, 172, 173]. Scott investigated a non-saturated hysteresis on the skin of a banana [174] claming that only well-saturated $P-E$ loops should be used as evidence for ferroelectricity. Thus, one has to be careful when interpreting non-saturated $P-E$ loops. Unlike electrical measurements that are often subjected to controversy, structural measurements are more conclusive. Although they are more time-consuming, structural investigations are helpful for the investigation of ferroelectricity. For example in FE materials, the measured strain as response to a triangular field ramp gives rise to the "butterfly" loop as shown in Figure 2.2 of Chapter 2. Although the strain can be investigated using optical interferometry [175, 176], time-resolved synchrotron X-ray diffraction has recently been shown to be a practical tool for studying the electromechanical response of FE thin films with good spatial and temporal resolution [177, 178].

In this chapter, the relation between $\varepsilon - E$ loops and $P - E$ loops is studied by TR-XRD as the frequency of the applied field is varied. We observed the influence of domain wall motion on both hysteresis. The piezoelectric response before polarization reversal displayed a non linearity with respect to the external field. To elucidate this, we investigated the influence of the applied field rate on the electromechanical response. Such structural investigation is fundamentally useful in understanding polarization reversal in ferroelectric thin films.

6.2 Experimental details

Our sample for this study is a (001) $Pb(Zr_{0.52}Ti_{0.48})O_3$ thin film of 200 nm thickness. This sample was provided to us by Bertrand Vilquin and Pedro Rojo-Romeo from the Ecole centrale de Lyon, France. This composition of PZT is close to the morphotropic phase boundary (MPB), well-known for having highest polarization and piezoelectric response, which makes it particularly suitable for applicatons in PE actuator devices [179, 180, 181]. The MPB is not exactly defined but exists between 45% and 50% of Ti content. XRD measurements show that Ti-rich compositions are marked by a phase coexistence region of rhombohedral and tetragonal symmetry whose width in the phase diagram depends on the compositional homogeneity and on the sample processing conditions [182, 183, 184]. Using synchrotron X-ray powder diffraction, Noheda *et al.*,, confirmed the existence of the tetragonality of the $Pb(Zr_{0.52}Ti_{0.48})O_3$ ferroelectric phase for a bulk sample [180].

The investigated PZT thin film was grown by sputtering on a 30 nm (001)$SrRuO_3$ layer deposited on an $SrTiO_3$ buffer layer, supported by an SiO terminated Si substrate. The sample was annealed afterwards to ensure better crystallinity of the PZT layer. Top electrodes of circular shape with radii varying between 150 μm and 300 μm were made by sputtering SRO on one half of the sample surface and evaporating Pt on the other. It is worth noting that in this chapter, we will not compare the symmetric SRO/PZT/SRO and asymmetric Pt/PZT/SRO capacitor configurations as their different annealing treatment conditions and electronic boundary conditions result in different domain configurations and hence also different switching dynamics. The symmetric devices were annealed after top SRO deposition, while the asymmetric ones were annealed before Pt deposition.

Reciprocal space maps shown in Figure 6.1 around the 002 Bragg reflections from the differently treated electrode regions of the sample directly show the differences. For instance, the peak width of the PZT reflection is broader under the SRO electrodes (Figure 6.1(a)) as compared to the Pt covered part shown in Figure 6.1(b). The broader SRO reflection on the SRO/PZT/SRO device (Figure 6.1(a)) as compared to the Pt/PZT/SRO device (Figure 6.1(b)) indicates strain relaxation through the PZT film, since the broadening probably originates from different lattice constants in the bottom and top SRO layers.

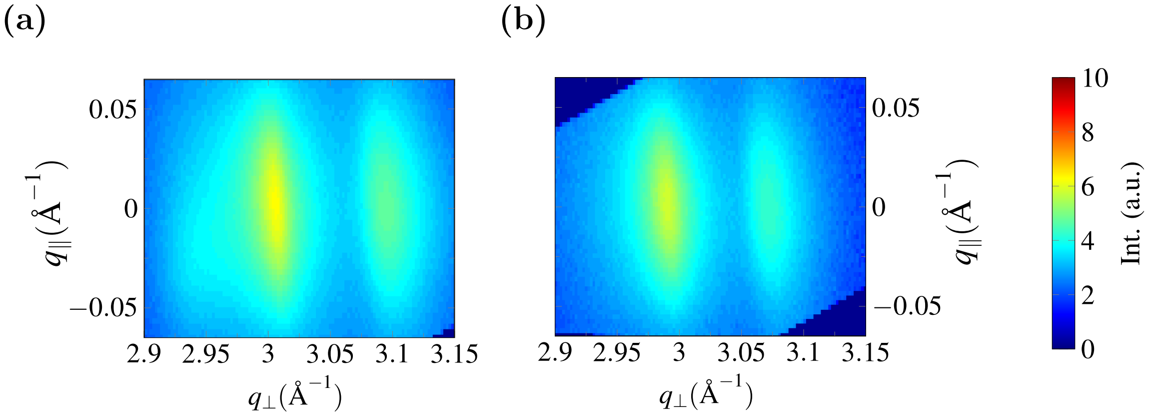

FIGURE 6.1: RSM around the 002 Bragg reflections of PZT and $SrRuO_3$ of the annealed film under (a) the $SrRuO_3$ top electrode (b) the Pt top electrode.

In Figure 6.1, $q_{\perp}$ represents the momentum transfer perpendicular to the sample surface and $q_{||}$ the corresponding in-plane component parallel to the sample surface. The PZT reflection in Figure 6.1(a) shows a nonuniform broadening along $q_{\perp}$, which we associate to the annealing treatment after the deposition of the SRO top electrode.

The setup for the TR-XRD experiment was described in Chapter 3 where the diffracted X-rays are detected using the fast APD. However, for the following experiments, a detector slit was placed in front of the detector in order to ensure that only symmetrically diffracted photons were collected.

6.3 Results and discussion

6.3.1 Polarization-electric field hysteresis and the electromechanical response

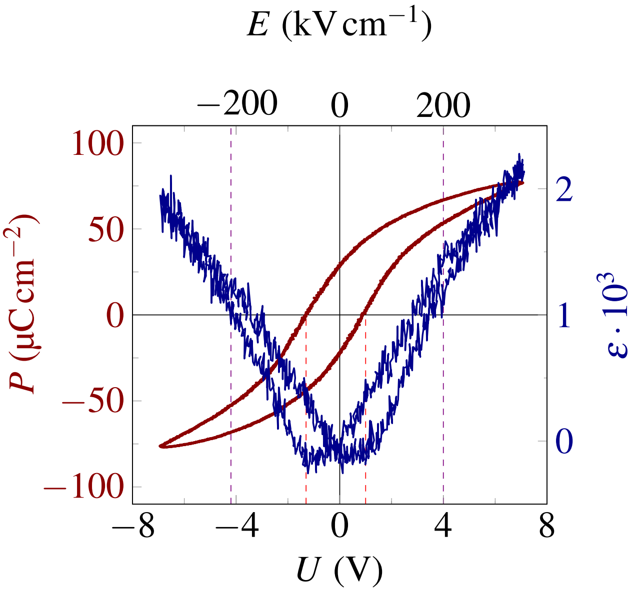

FIGURE 6.2: $P - E$ (red) and $\varepsilon - E$ (blue) hysteresis loops measured on a SRO/PZT/SRO test device at 1 kHz.

Mechanical strain, ε, in a FE material is induced by an electric field E through the inverse piezoelectric effect. In Figure 6.2 we plot, in the same diagram, the $P - E$ and $\varepsilon - E$ loops of a Pt/PZT/SRO device measured at 1 kHz and compare the changes of polarization and strain as a function of the electric field. At the coercive field, marked by the dashed red line, the macroscopic polarization is null and the expansive strain develops. The beginning of saturation of the P-E loop around 4 V marked by the dashed violet line is concomitant with the non-hysteretic part of the butterfly loop, which illustrates that above this electric field, the strain is mainly piezoelectric. Both the P-E and the $\varepsilon - E$ hysteresis loops are driven by the converse PE effect of the crystal lattice and domain wall motion induced by FE switching [29]. The asymmetry of the positive and negative coercivity is also observed in the measured expansive strain, which shows maxima at the maximum positive and negative applied field just like the saturation polarization.

6.3.2 Frequency-dependence of the $P - E$ and $\varepsilon - E$ hysteresis

For the design of new technological applications, the measurement of P-E loops is important as it allows to determine critical parameters such as remanent polarization and coercive field. Frequency-dependent measurements of the P-E hysteresis are important, especially for high speed memory applications as they allow to determine the frequency above which device failure might occur.

SRO/PZT/SRO capacitor device

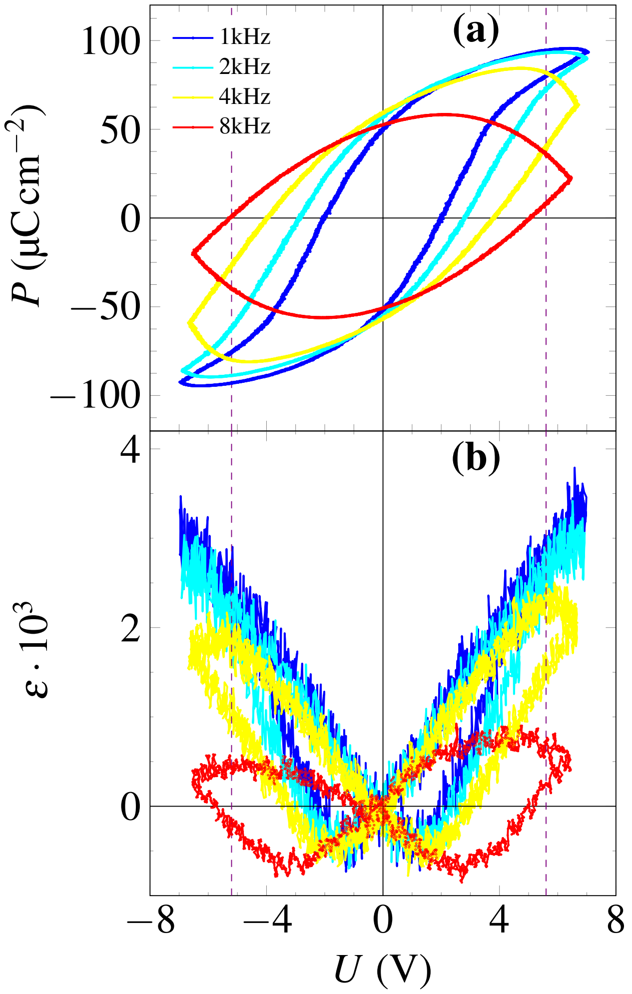

FIGURE 6.3: Frequency-dependence of the $P-E$ and $\varepsilon-E$ hysteresis loops measured on a SRO/PZT/SRO device. U is the measured voltage drop across the device.

In Figure 6.3(a) we show the evolution of the $P - E$ hysteresis loop for the SRO/PZT/SRO device structure at different frequencies between 1 and 8 kHz. The measurement at 1 kHz reveals a positive coercivity of $\approx 1.8\,\mathrm{V}$ and a negative coercivity of $\approx$ -2 V. Thus, the maximum of the applied field $U = 7\,\mathrm{V}$ which is about 3 times the coercive voltage U_c is sufficient to reach saturation.

During these measurements, the amplitude of the driving field was kept constant. As the frequency increases to 4 kHz, the $P - E$ hysteresis becomes more and more rounded and the saturation polarization P_s decreases. However, P_r in this frequency range depends only weekly on the frequency. For increasing frequency, the loop flattens towards a horizontal major axis ellipse. Our measurements confirm the frequency-dependence of E_c reported in literature [185, 186]. Similar unsaturated rounded loops have been attributed to leakage [187, 188]. The frequency-dependent $P-E$ loops at 4 and 8 kHz presented in Figure 6.3(a) show that the polarization increases while the field is being ramped down from its maximum to zero. This is concomitant with an increase of the strain as can be seen in Figure 6.3(b). Already at a frequency of 4 kHz, which is represented by the yellow color in Figure 6.3, the non-hysteretic part of the butterfly loop is not reached. The same is true for the maximum polarization value, which starts to decrease at 4 kHz.

Figure 6.4 shows the simultaneously recorded variables as function of the normalized time. The dotted vertical lines in all panels represent the time when the maximum positive and negative field are applied, which correspond to 1/4 and 3/4 of the cycle respectively. As shown in panel (a), the voltage drop across the device weakly decreases with increasing frequency although the output of the function generator is kept constant. For easy visualization, the polarizations shown in Figure 6.4(b) have been adjusted to start from zero. Figure 6.4(c) shows the c-axis dependence on the field cycle. For the measurements at 1 and 2 kHz, the polarization and the strain have their maxima close to the same time where the maximum of U is observed.

At 4 kHz, even though the field is already ramping down from the maximum of $U = 7\,V$ of the applied triangular pulse, the strain still continues to increase for further 15 µs which corresponds to 6% of the total field period after which the strain finally starts to decrease linearly to zero. Similar behavior is observed for the polarization that increases while the field is being ramped down and reaches its maximum at about the relative same time as the maximum strain. The time lag between the maximum applied field and the occurrence of the maximum strain is the origin of the rounded $\varepsilon - E$ loop observed in Figure 6.3.

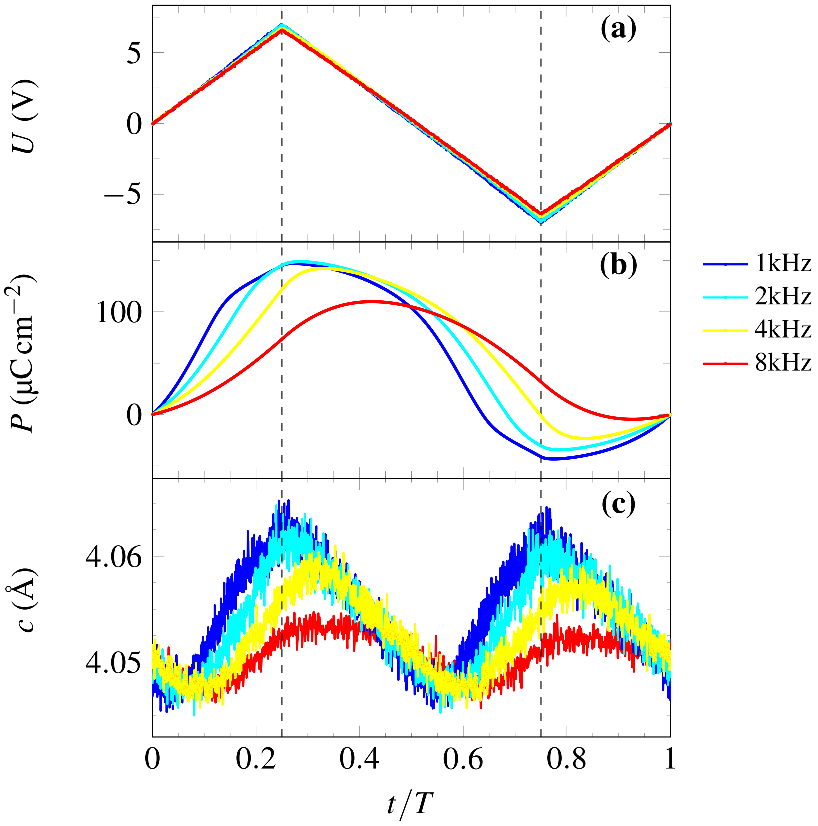

FIGURE 6.4: Frequency-dependence of (a) the voltage drop U across the capacitor, (b) charge density P on the surface and (c) lattice constant c against the normalized time t/T, where t is the time and T is the period of the corresponding measurement given by the frequency.

The origin of this delayed electromechanical response is likely related to the relatively slow domain wall velocity known in ferroelectrics [189, 190]. The maximum expansive strain at this frequency is roughly 35% lower than that observed during the 1 and 2 kHz measurements. Doubling the frequency once more up to 8 kHz additionally reduces the maximum expansive strain by about 80%, where again a phase lag between the maximum applied field and the maximum of the expansive strain of about 30 µs is observed. The time by which the electromechanical response lag behind the electric field seems to depend on the ac field frequency. This would explain why at low frequencies the effect is not observed since the time delay is small compared to the overall pulse period and for sufficiently low frequencies, the time needed for domain motion is much smaller than the pulse period and the phase delay is negligible. The measurements at 4 and 8 kHz show higher c lattice constant at zero field (Figure 6.4(c)) compared to the measurements at 1 and 2 kHz, which is due to the fact that at high frequency the domains do not get enough time to return to their equilibrium state before the next tail of the triangular pulse sequence arrives.

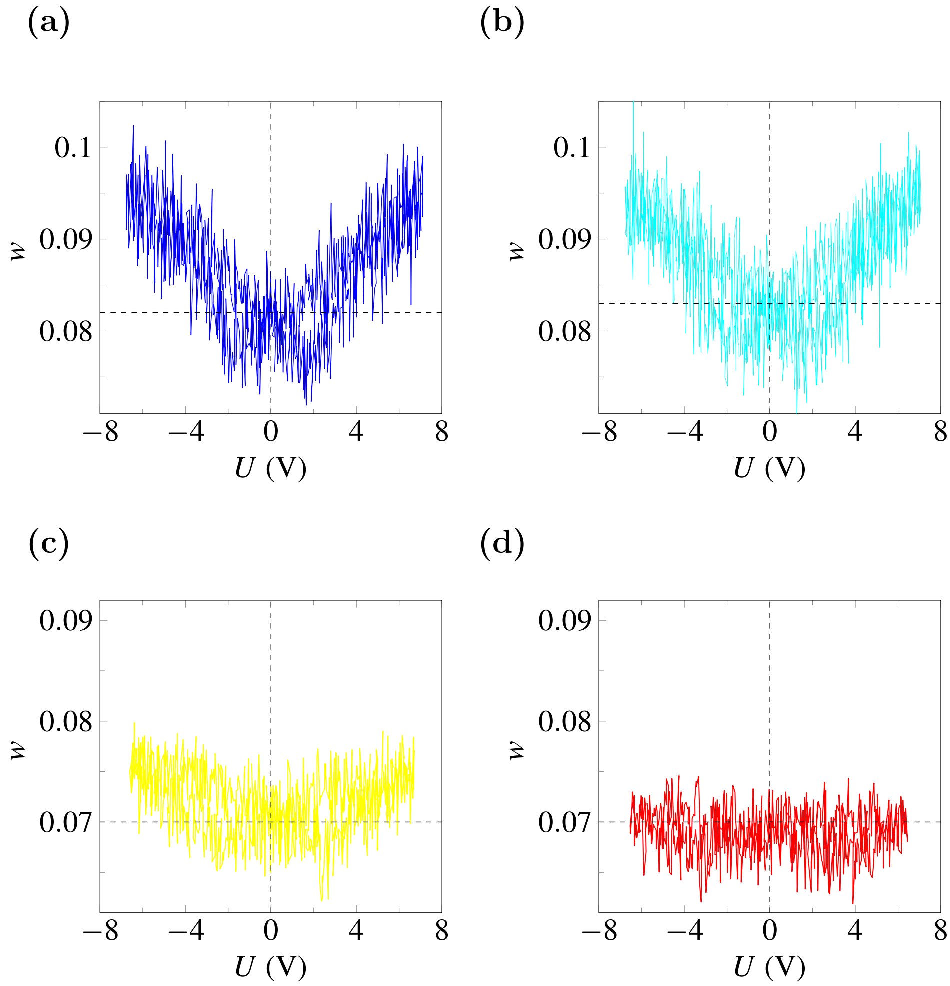

FIGURE 6.5: Normalized FWHM of the Bragg reflection as a function of electric field during (a) the 1 kHz, (b) the 2 kHz, (c) the 4 kHz and (d) the 8 kHz bipolar electrical pulses.

In Figure 6.5 the FWHM of the PZT peak w is plotted against the applied field amplitude at different frequencies. They exhibit a close resemblance to the $\varepsilon - E$ butterfly loop that characterizes the electromechanical response of the FE. For example, for the measurement at 1 kHz , at the onset of the field w first decreases and then mimics the change of the electric field with time when the coercive field is surpassed. As the frequency increases (Figures 6.5(a-d)), the shape of the w(E) loop changes from the butterfly-like shape to a constant value. We attribute this effect to incomplete polarization reversal at higher frequencies where the maximum of the applied field is not enough to reach saturation. Similar behavior was observed in Chapter 4 and 5 where the $w_\perp$ of the PZT peak, extracted from the RSMs, only start increasing when the reversed domains started merging together (that is inferred from the observed maximum of $w_\|$).

While the *P*-*E* loops and $\varepsilon - E$ loops remain symmetric during the low-frequency measurements up to 2 kHz, a pronounced asymmetry emerges at higher frequencies, particularly visible on the $\varepsilon - E$ loops in Figure 6.3(b). This behavior is attributed to imprint effects arising from a built-in internal field, likely due to trapping of free charge carriers [191, 192, 193].

An increasing expansive strain is expected to result in an increased polarization as the dipole volume parallel to the electric field is increased: $P = N \cdot p_i$. Since at high frequency the additional contribution from domain propagation is phase delayed, this leads to the observed rounding of both hysteresis loops. Such delayed structural response was experimentally observed by Daniels *et al.,* in bulk PZT ceramic samples with tetragonal symmetry [194]. They measured a phase lag between the (111) lattice strain and a sinusoidal applied waveform already at a cycling frequency of 3 Hz. This confirms the conclusions from previous works, which showed that the domain propagation velocity does not only depend on the elastic material properties but also depends on more parameters such as the defect structure in the film [195], device size, and ac field amplitude and frequency [196].

Pt/PZT/SRO capacitor device

In this section, we present the corresponding measurements on an asymmetric Pt/PZT/SRO device from the same sample. A triangular waveform of amplitude $U = 7\,V >> U_c$ yields the curves shown in Figure 6.6 for different frequencies between 2 and 40 kHz. Similar to the symmetric device, a well saturated hysteresis is observed at low frequency. With increasing frequency, the maximum polarization decreases monotonously whereas the remanent polarization first increases untill an ac frequency of 20 kHz, then decreases with even higher frequencies.

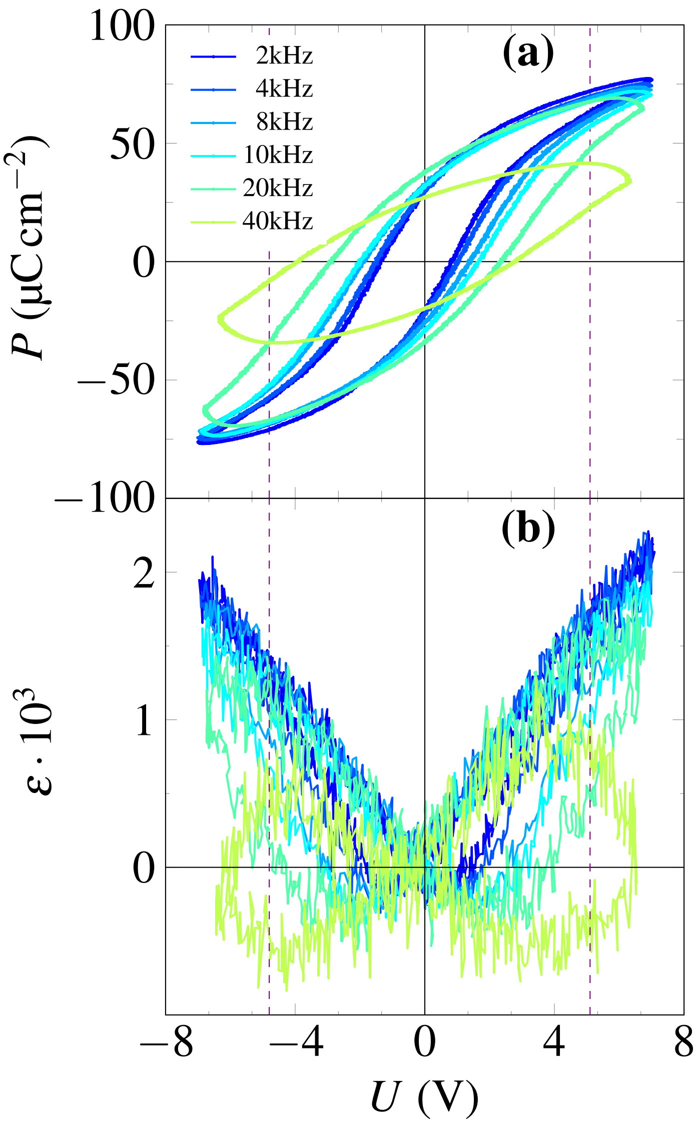

FIGURE 6.6: Frequency-dependence of the P-E and $\varepsilon - E$ hysteresis loops as measured on a Pt/PZT/SRO device.

As shown before in section 6.2, the domain morphology in this asymmetric device, observed from the RSM (Figure 6.1) differs from the symmetric one. The $P-E$ and $\varepsilon-E$ hysteresis loops displayed in Figure 6.6 were measured on a device with area 4 times smaller than that used for the previously presented results from the symmetric SRO/PZT/SRO devices. Nonetheless, measurements on an asymmetric device of comparable size as the symmetric one showed a similar coercive field but smaller PE strain and a complete polarization reversal up to 4 kHz ac frequency. This suggests that the frequency threshold at which the hysteresis loops cease to saturate does only weakly depend on the electrode size. This confirms findings of Merz on BTO single crystals who already suggested that the switching time does not depend on the electrode area [197]. The measurements presented here were performed on a device with smaller area because it could sustain the electrical pulse sequences for longer time before electrical breakdown as compared to the larger area devices.

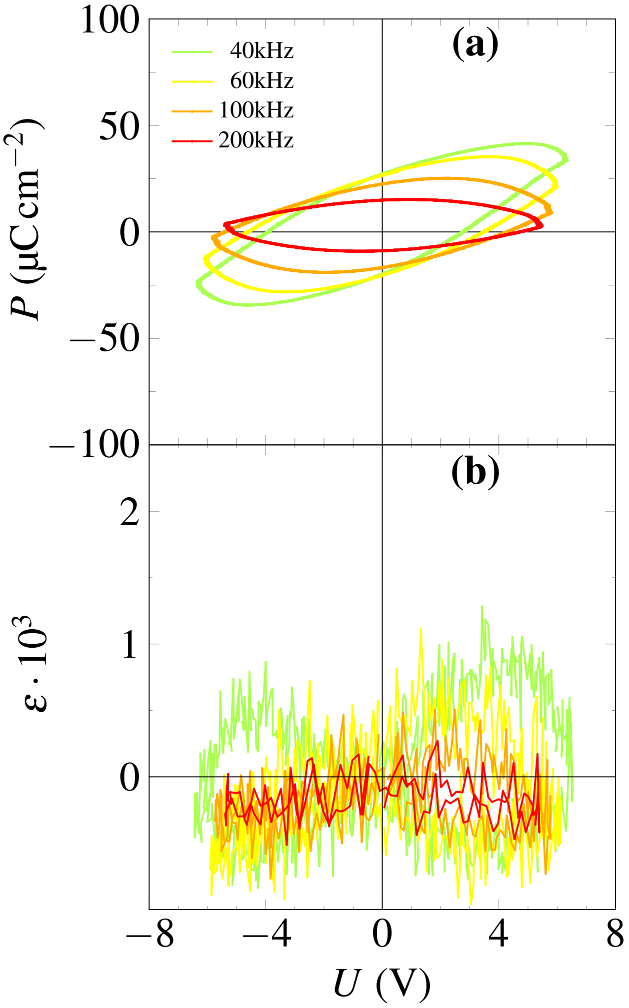

FIGURE 6.7: High frequency dependence of the P-E and $\varepsilon - E$ hysteresis loops measured on a Pt/PZT/SRO device.

A further increase of the frequency with constant field strength leads to further reduction in both hysteresis. A reduction of the voltage drop across the device is also observed with increasing frequency. Figure 6.7 shows the $P - E$ and $\varepsilon - E$ loops for frequencies between 40 and 200 kHz. At 200 kHz, the $P - E$ loop is almost centered around the horizontal axis and the electromechanical response is purely compressive.

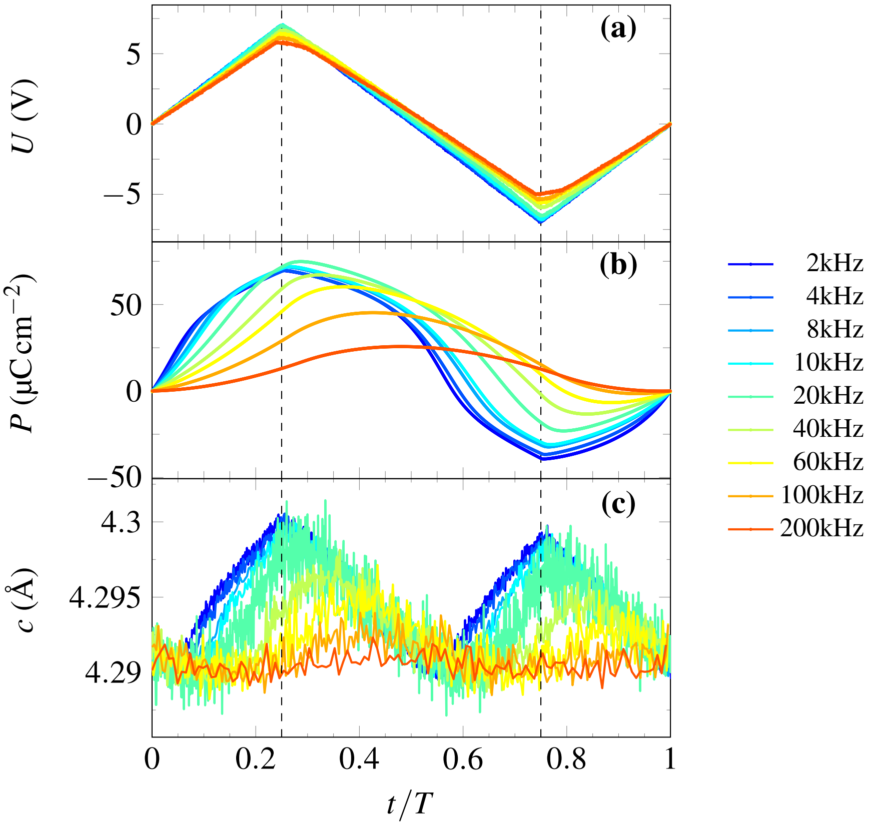

FIGURE 6.8: Frequency-dependence of (a) the voltage drop U across the capacitor, (b) charge density P on the surface and (c) lattice constant c against the normalized time t/T.

Figure 6.8 summarizes the simultaneously recorded variables, from Figure 6.6 and 6.7 against the normalized time. A pronounced phase shift between the strain and the voltage drop across the capacitor is observed at 40 kHz ac cycling frequency and higher. Again, the maximum voltage (Figure 6.8(a)) decreases with increasing ac frequency and the polarization and c lattice constant show their maxima at about the same time (Figure 6.8(b) and (c)). At 200 kHz, the lattice constant continuously decreases while the field is ramped from zero to its maximum, then increases while the field is being ramped down to zero from its maximum. The negative polarity of the pulse reproduces the same behavior. This suggests a 180° phase shift between the lattice response and the applied external field.

For the symmetric SRO/PZT/SRO device, the maximum polarization and strain, measured at 4 and 8 kHz, are reached after unloading from ± 7 V whereas for the Pt/PZT/SRO device such behavior is observed for frequencies between 20 and 100 kHz. For both devices, the maximum electric field applied, 7 V, is more than 3 times the coercive voltage measured at the lowest applied frequency of 1 kHz. In both cases, the coercive voltage increases with increasing frequency. In ferroelectric materials, the frequency dependence of $E_c = \frac{U_c}{d}$ has been demonstrated [185, 186] and the origin attributed to domain motion that is time- and field-dependent [198]. Our measurements confirm as demonstrated in Figure 6.9 the empirical relation $E_c \propto f^{\beta}$ [199] between E_c and frequency f where the value of the exponent β is proportional to the effective dimension n of the switching domains ($\beta = n/6$ [198]) and the waveform of the applied field [200]. Thus, a smaller value of β suggest a reduced dimensionality of the domain shape. The average coercive voltage $U_c = \frac{|U_{c+}|+|U_{c-}|}{2}$ is extracted from the P-E loops presented above and is plotted against the measurement frequency together with the fitted function f^{β}. Here U_{c+} refers to the cross point of the P-E loop with the positive x-axis and U_{c-} to the cross point with the negative x-axis. We observed β values of 0.69 for the symmetric device and 0.33 for the asymmetric device. The different β exponents indicate that both devices exhibit different domain structures during the switching process.

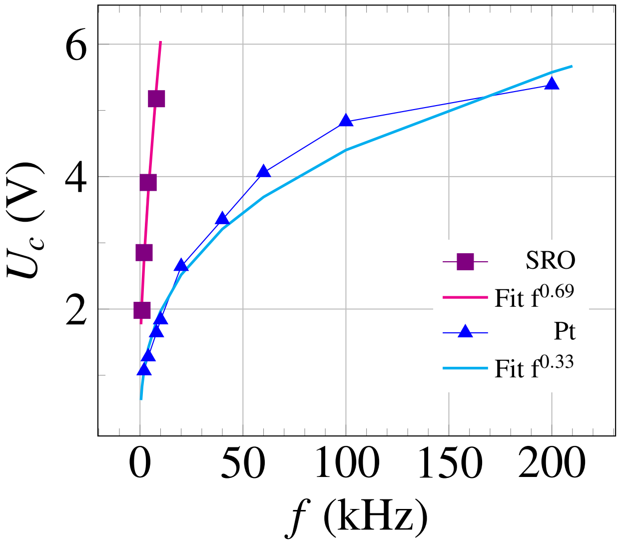

Figure 6.9: U_c as a function of the measurement frequency for the symmetric SRO/PZT/SRO and asymmetric Pt/PZT/SRO devices. The solid lines are calculated from the relation f^{β} and the values of β is given in the figure legend.

The incomplete saturation of the $P-E$ loop observed at high frequency has been rarely discussed. The hypothesis of leakage is not considered here since the contribution of leakage currents to the hysteresis has been shown to reduce with increasing measurement frequency [201, 202, 203] due to reduction of the measurement time. In particular, leakage does not explain the $\varepsilon - E$ dependence because Joule heating would lead to a negative thermal expansion of PZT, i.e., lead to the opposite effect [204]. The dependence of the hysteresis area A on the frequency f of the cycling field is presented in Figure 6.10. The hysteresis area represents the energy dissipated during one cycle of domain reversal.

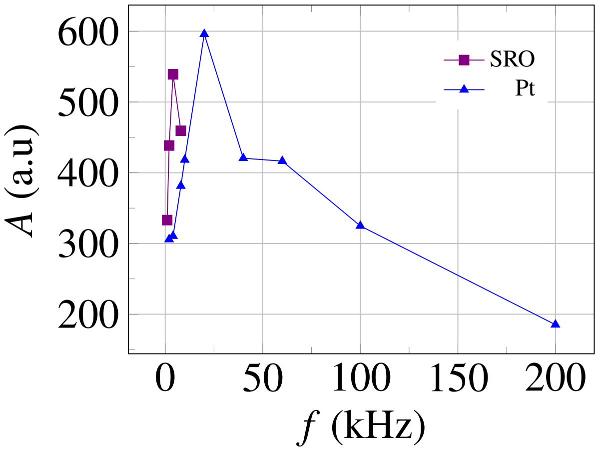

FIGURE 6.10: Area A of the $P-E$ hysteresis loop as a function of the measurement frequency for the symmetric SRO/PZT/SRO and asymmetric Pt/PZT/SRO devices.

The hysteresis area is small at low frequency because of the small U_c, then increases up to its threshold frequency f_0 because U_c increase, and then subsequently decreases with increasing frequency due to the decrease of the maximum polarization at high frequency. The difference in f_0 between the 2 devices is not proportional to the diffrence between the device size. Such "single-peaked" pattern in the dependence of the hysteresis area on the frequency has been discussed for similar compositions of PZT [205, 206, 207]. On the other hand, 2D phase field simulations of the frequency dependence of the hysteresis loop show that in dislocation-free ferroelectrics the coercive field and remanent polarization increase with increasing frequency [208] while in crystals with dislocation arrays the simulation results show similar dynamic behavior as obtained in our measurements. The decrease of A is concomitant with the incomplete polarization reversal, as seen from the $\varepsilon - E$ loops. This confirms the conclusions from Liu *et al.*, who stated that given an applied field U, the frequency at which A is maximal is the marginal frequency at which all domains achieve a complete reversal so that the energy dissipated during the reversal reaches its maximum [206].

6.3.3 The effect of loading time on the electromechanical response

For applications such as actuators, the mechanical strain which ferroelectrics exhibit under the effect of an electric field is particularly useful. The piezoelectric strain ε usually relates linearly to the driving field E via $\varepsilon = d_{33} \cdot E$. During FE polarization reversal, this relationship no longer holds because of the movement of domain walls in the material. In the previous section, domain wall movement has been shown to depend on the electric field cycling frequency, which leads to a delayed strain-electric field response at high frequencies. Over the whole investigated frequency range, the PE contraction measured before the polarization reversal is much smaller than the following expansion after reversal. This is partly due to the clamping of the film to the substrate that hinders the compression of the thin film.

As highlighted in Chapter 4, the PE contraction induced during polarization reversal by a square voltage pulse is always smaller than that induced during switching by a slowly ramping field despite the higher external field for the square pulse at the time when the maximum contraction is observed. As a reminder, the sample presented in Chapter 4 has the following structure: Pt/Pb($Zr_{0.2}Ti_{0.8}$)O_3/SRO//STO. Figure 6.11 shows in panel (a) the strain response of the PZT FE layer during polarization reversal by a square voltage pulse and in panel (b) the response to a 2 kHz ramping field, for this sample. The voltage presented in the upper panel of Figure 6.11(a) was measured on a different device as the strain in the lower panel but still on the same sample.

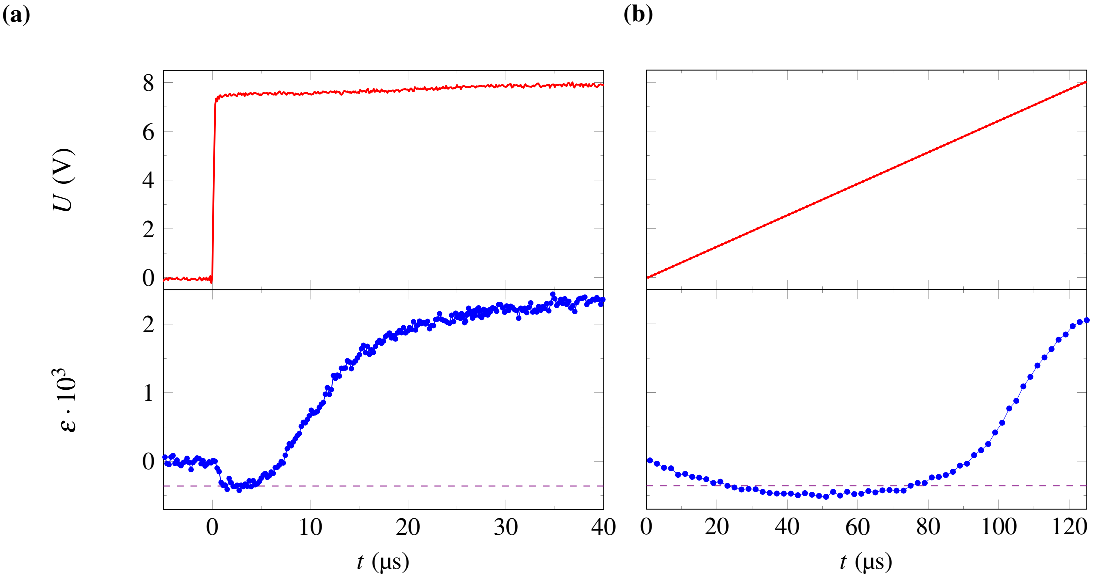

Figure 6.11: Applied electric (upper panels) and induced strain (lower panels) as a function of time for the Pt/Pb($Zr_{0.2}Ti_{0.8}$)O_3/SRO device during polarization reversal with (a) a square voltage pulse (b) the positive ramp of a triangular pulse with 2 kHz frequency.

The dotted line in the lower panels of Figure 6.11 illustrates the amount of compressive strain triggered during the square pulse. The latter amounts to $\sim 0.36 \cdot 10^{-3}$ as compared to $\sim 0.52 \cdot 10^{-3}$ during the ramping field. The square pulse could be regarded as a 2 MHz pulse since its rising edge is less than $\sim$ 0.5 µs long. During the ramping pulse, the voltage at which the minimum strain is measured corresponds to $U_c \approx 3.8$ V, that is far less than the 8 V applied during the square pulse. This effect is even more pronounced for the MPB PZT composition where the contraction is observed just for $\sim$ 5 µs during the square pulse. Figure 6.12 shows the strain response of the PZT FE layer during square voltage pulse switching (panel (a)), during a 4 kHz ramping field (panel (b)) and during to a 2 kHz ramping field (panel (c)). Here again, the dotted line insert in the lower panel represents the amount of compressive strain induced during the square pulse.

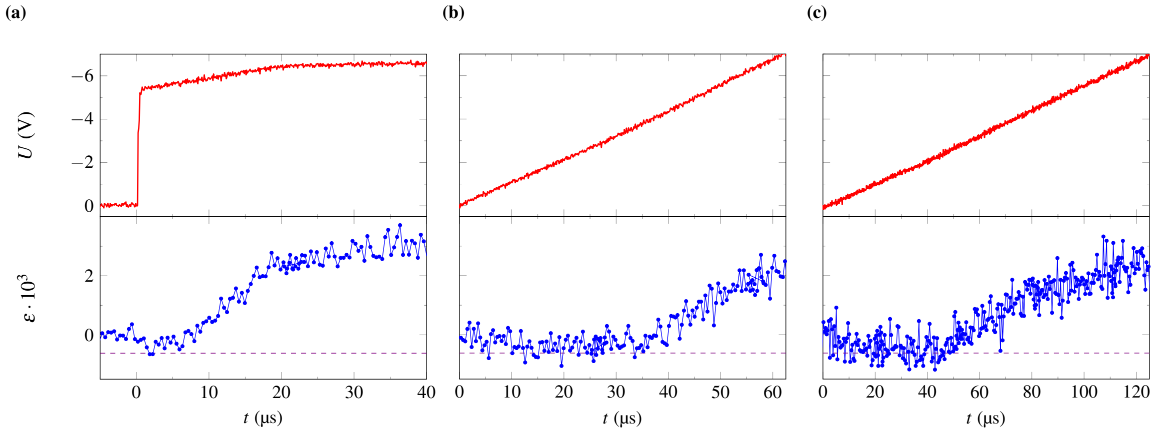

Figure 6.12: Voltage drop across the capacitor (upper panels) and induced strain (lower panels) as a function of time for the Pt/Pb($Zr_{0.52}Ti_{0.48}$)O_3/SRO device during polarization reversal with a (a) square voltage pulse, (b) 4 kHz ramping pulse and (c) 2 kHz ramping pulse.

The contraction induced during the 4 kHz ramp is approximately equal to that triggered during the square pulse even though present for a longer time. The 2 kHz ramp induced an additional strain of $\sim 0.28 \cdot 10^{-3}$.

The results presented in Figure 6.11 and 6.12 indicate that the maximum contraction induced during polarization reversal for fully switching pulses decreases with increasing frequency. This is surprising since the field at which it occurs is larger at high frequency. Generally, it is argued that high negative strain is mainly due to contribution from non-180° (ferroelastic) domain switching events during the increase of the applied field from 0 to the coercive field [209, 210]. We did not observe any signature of 90° domains from the RSM measured during the field cycling.

To investigate the relation between the loading time of the FE capacitor and the amount of compressive strain, the amplitude and frequency of the applied pulse were kept constant and the loading time of the device was varied by inserting an additional Ohmic resistance R$_{ext}$ in the measurement scheme as depicted in Figure 6.13, and we performed simultaneous TR-XRD and electrical measurements as previously described.

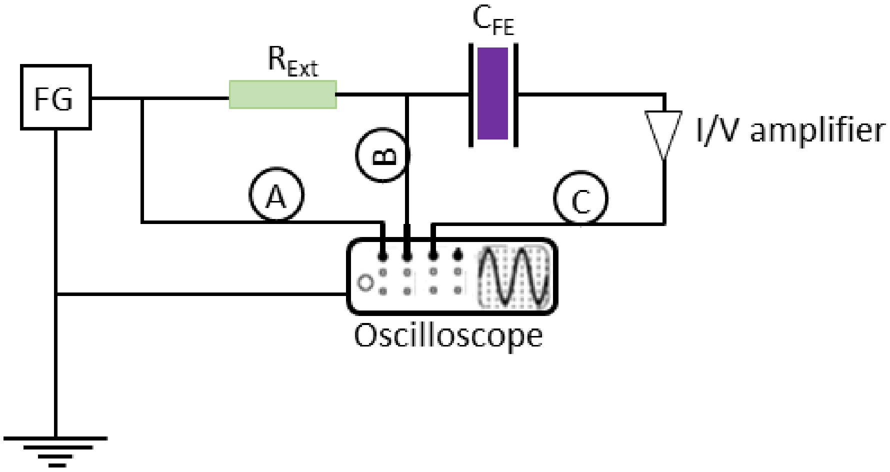

FIGURE 6.13: Schematic of the measurement scheme. The function generator FG is used to supply voltage pulses. A resistance R$_{ext}$ is connected in series with the FE capacitor C$_{FE}$. The current flowing through the circuit is measured by connecting a current-to-voltage amplifier I/V between the FE and the oscilloscope. A, B and C are different channels of the oscilloscope used to record the current and voltage across different branches of the circuit.

Figure 6.13 shows the circuit of the measurement scheme. The applied voltage U_a and the voltage drop across C$_{FE}$ are measured through the oscilloscope channel A and B, respectively, while the current flow is measured through channel C.

Since the time needed to fully charge the device is given by the RC time constant τ_{RC}, the charging time could be modified by inserting a resistance R$_{ext}$ in series between FG and the FE device. Inserting R$_{ext}$ modifies τ_{RC} and thus the build up time of the potential across C$_{FE}$. During this experiments, bipolar triangular voltage pulses were applied but only the positive ramp of the pulse is discussed here. Figure 6.14(a) shows the voltage drop U_{FE} (measured from channel B in Figure 6.13) across the Pt/Pb(Zr$_{0.52}$Ti$_{0.48}$)O$_3$/SRO device for the different values of R_{ext} used: The experiments have been performed for the values R_{ext} of 51, 100, 200, and 390 Ω. For small R_{ext}, the 125 µs long ramp does not exhibit a significant difference from U_a (measured from channel A in Figure 6.13). As R_{ext} is increased, $U_{FE} = U_a$ - U_{Rext} shows a weak decrease around 30 μs that is seen in Figure 6.14(a), when the current, shown in Figure 6.14(b) approaches its maximum and then recovers once the maximum current is surpassed. This is expected from electrostatics since in resistors the voltage drop increases with both increasing current flow and resistance as $U_{Rext} = R_{ext} \cdot$I.

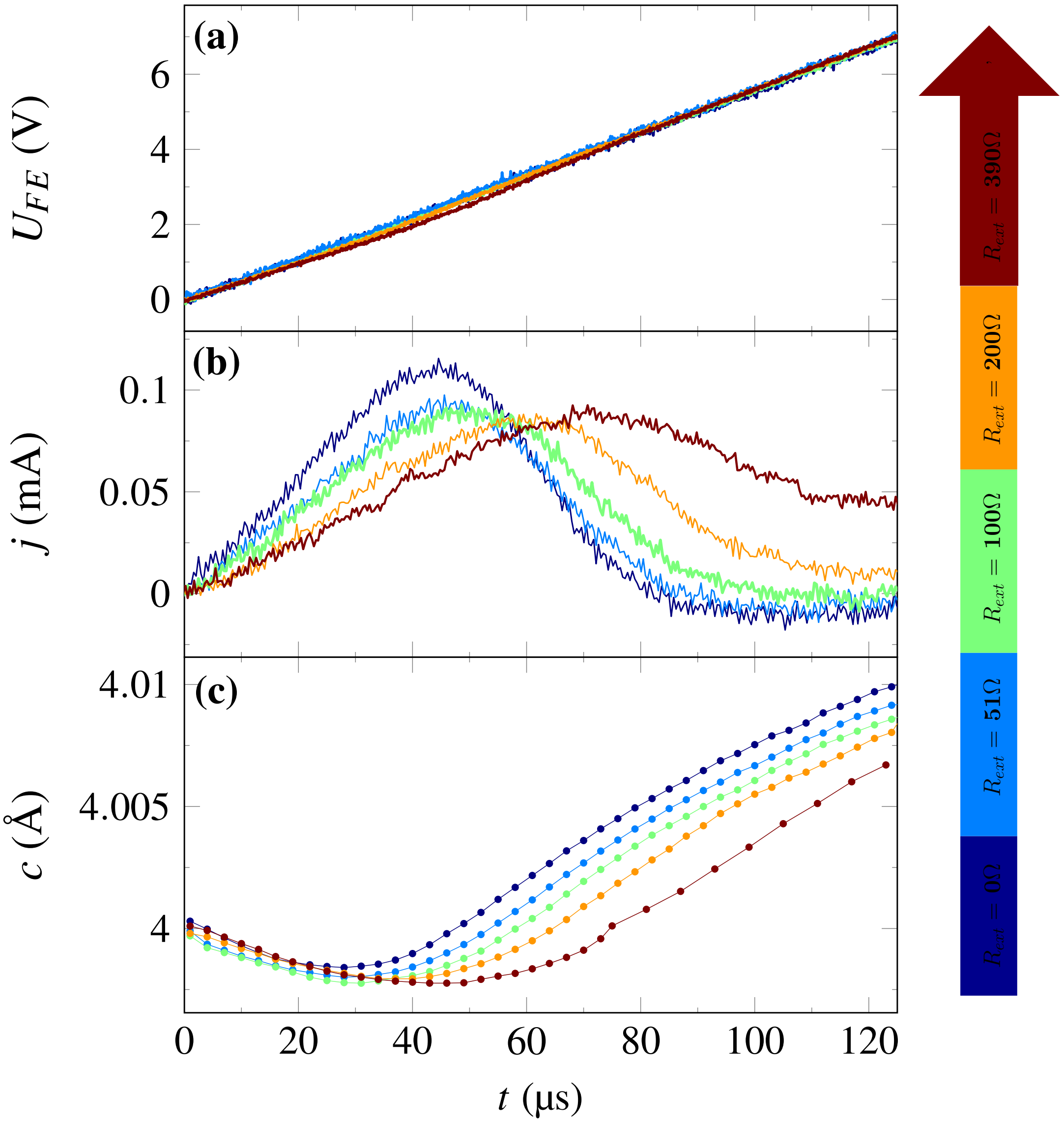

FIGURE 6.14: Structural and electrical dynamics under varying loading time. (a) Voltage drop across the FE layer. (b) Measured current flow. (c) c-axis response to the applied field as a function of time.

The simultaneously recorded current transient and lattice strain are presented in Figure 6.14(b) and 6.14(c) respectively. They both show time-dependent responses depending on the value of R_{ext} although U_{FE} is almost unchanged. The coercive field, marked here by the maximum of the displacement current, decreases with increasing R_{ext} and shifts to later times although U_{FE} is only weakly reduced. The decrease of the current amplitude can be predicted by using Kirchhoff's law to describe the circuit. The current flow j through each element of the circuit is the same:

$$\begin{aligned} j_{FE} &= j_{Rext} \\ &= \frac{U_{ext}}{R_{ext}} \\ &= \frac{U_a - U_{FE}}{R_{ext}} \end{aligned} \tag{6.1}$$

Equation 6.1 shows that current decreases with increasing R_{ext} in accordance with our observation. Concomitantly, the amount of compressive strain increases and shifts in time.

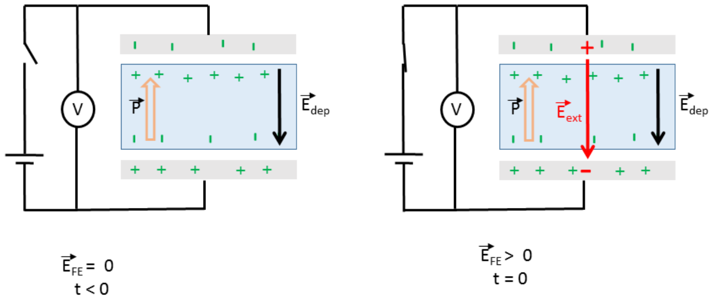

FIGURE 6.15: Schematic of a FE capacitor showing the directions of the depolarization field E_{dep} and applied field E_{FE} at $t = 0$.

The internal field $\vec{E}_{int}$ acting on the FE layer is a combination of the applied electric field $\vec{E}_{FE}$ ($E_{FE} = U_{FE}/\mathrm{d}$) and depolarization field $\vec{E}_{dep}$ arising from the alignment of the electric dipoles within the layer and is given by $\vec{E}_{int} = \vec{E}_{FE} + \vec{E}_{dep}$. When no external field is applied, $\vec{E}_{int} = \vec{E}_{dep}$. The strength of $\vec{E}_{dep}$ depends amongst other things on the amount of charges on the metal electrodes compensating the polarization; the more compensation charges are present, the weaker is the depolarization field. At time $t = 0$, $\vec{E}_{FE}$ parallel to $\vec{E}_{dep}$ is applied to reverse the polarization direction. At the onset, the depolarization field assists the switching process. With time, the already switched dipoles form domains that tend to weaken this field's influence thus changing the τ_{RC} in a way controls the depolarization field strength and thus the internal field within the device. The maximal lattice distortion before switching was increased from ~ -0.5 ‰ to ~ -0.6 ‰ by inserting $R_{ext} = 390\,\Omega$. For this resistance, $\varepsilon(t)$ presents a slower turn at the lowest strain point than for the fast loading measurement. One can argue that with the slow loading rate, where the domains effectively get longer exposure to a given instant of the field, a higher degree of finalization of domains switching should be achieved. Hence, a larger negative strain develops and shifts of the measured coercive field is observed. In addition, domain wall creep motion might become important on such long timescales resulting in the slower subsequent expansion of $c(t)$. On the other hand, for a slowly varying field the switched charges have enough time to be screened and can thus reduce the depolarization field assisting the switching process and hence the shift in measured coercive field due to increasing switching time.

6.4 Summary and Conclusions

Simultaneous measurements of the dynamic polarization-electric field and electromechanical hysteresis is important for understanding the coupling between electric and mechanical properties in FE thin films. The limited speed of domain motion has been observed to cause a phase shift between the external loading and material response, resulting at characteristic frequencies to anomalies in the $P-E$ hysteresis that could, without structural investigations, be attributed to leakage. The anomalies are evidenced as an increase in strain and polarization during the unloading process due to the phase lag between the strain and the driving field. The critical frequency f_0 at which this begins to emerge depends on the ac field amplitude and domain structure of the film. A further increase of the frequency leads to the complete disappearance of the butterfly shape of the $\varepsilon - E$ hysteresis loop with a purely compressive electromechanical response at 200 kHz suggesting a 180° phase lag. These results highlight the important role of domain wall motion during polarization reversal. Similar observations were reported by Bhattacharyya *et al.,* for bulk ceramics [211]. The dynamic response at such high frequency is interesting since it is more directly related to device performance in ferroelectric memories.

We have used a FE capacitor in series with an ohmic resistance to measure the electrical and structural dynamics in the FE layer during polarization reversal under different RC time constant. High external resistance increases the build up time of voltage across the FE (U_{FE}) that leads to slower polarization switching dynamics. This shifts the switching current peak in time hence increasing the coercive field, and widens the electromechanical hysteresis loop, achieving higher piezoelectric strain within the crystal. These experiments confirm once more that the time-dependent response of FE during polarization reversal depend considerably on experimental conditions such as frequency, amplitude, and even the RC time constant of the test structure.

Chapter 7

Static and dynamic characterization of $BiFeO_3$ thin films

7.1 Introduction

Just like for other ferroelectrics, the piezoelectric property of multiferroic $BiFeO_3$ (BFO) can be exploited for applications such as sensors and actuators. The coupling between its weak magnetization and large electric polarization makes it a good candidate for memory applications where magnetic information can be written electrically and read magnetically [212, 213, 214]. This is a huge advantage since writing data with an electric field requires less energy than what is neccessary to write with a magnetic field that is induced by a current. In addition, magnetic field data readout is non-destructive unlike electric readout. The desire for lead-free compounds in addition to the aforementioned reasons accounts for the increasing interest in studying this system [60, 215].
X-ray diffraction studies on BFO single crystal showed that its room temperature structure is rhombohedral [216]. Electric field induced polarization switching in such rhombohedral structures is more complex than observed in other tetragonal perovskite ferroelectrics. Studies on BFO revealed rotation of the oxygen octahedra under electric field and a shift of the Bi^{3+} and Fe^{3+} ions along the <111> direction during polarization reversal with the Fe^{3+} ion shift being 4 times less than that of the Bi^{3+} ion [63, 65, 67, 217]. XRD studies of FE polarization reversal in BFO are rare [218, 219].

In this chapter, XRD characterization of BFO thin films with different FE domain variants is presented in the first part. In the second part, TR-XRD is used to follow the dynamics of the (001) lattice plane of BFO under an electric field applied along the <001> direction, perpendicular to the film surface.

7.2 Experimental details

Label	**Top electrode**	**Top layer**	**Buffer layer**	**Substrate**	**Comments**
Sample I	Pt	$BiFeO_3$ (150 nm)	$SrRuO_3$ (8 nm)	$DyScO_3$ (110)	pure 71° stripes
Sample II	Pt	$BiFeO_3$ (300 nm)	$La_{0.7}Sr_{0.3}MnO_3$ (25 nm)	$DyScO_3$ (110)	pure 109° stripes
Sample III	Pt	$BiFe_{0.95}Mn_{0.05}O_3$ (200 nm)	$SrRuO_3$ (26 nm)	$SrTiO_3$ (001)	dominant 71° stripes
Sample IV	ITO	$BiFe_{0.95}Mn_{0.05}O_3$ (280 nm)	$SrRuO_3$ (26 nm)	$SrTiO_3$ (001)	dominant 109° stripes

Table 7.1: BFO samples investigated in this chapter with the different top electrode material, constituent layers and their nominal thicknesses, substrate material and orientation.

The samples used for this experiment were grown by pulsed laser deposition. Sample I consisted of a BFO film on a thin $SrRuO_3$ (SRO) bottom electrode grown on a (110)-oriented $DyScO_3$ substrate. Sample II had a similar tri-layer structure with $La_{0.7}Sr_{0.3}MnO_3$ as bottom electrode. Samples I and II were grown by Alan Brunier at the University of Warwick, United Kingdom. For both samples, Pt top electrodes were deposited by e-beam evaporation and patterning was done by either using a shadow mask or conventional UV photolithography techniques. Samples III and IV were made of BFO doped with 5% Mn on an SRO buffer and $SrTiO_3$ (STO) substrates. Doping is usually introduced to reduce leakage current which is an issue for pure BFO thin films, and thus improving device lifetime [220, 221]. Mn-doping increases the polarisation in BFO films without affecting its weak magnetisation [222]. Both samples are grown onto (001) oriented STO substrate. In (001) oriented films, 71° and 109° domain walls are equally favorable [58, 223]. In such films, the domain structure can be tuned to 71° or 109° by the strain induced from the substrate but also by controlling growth parameters such as oxygen pressure, deposition rate, substrate temperature or doping content of the target [223]. On the sample's top surface, electrodes were deposited by thermal evaporation of Pt for sample III and Indium Tin oxide (ITO) for sample IV, using a shadow mask. These samples were grown by Houssny Bouyanfif from the University of Picardie Jules Verne, France. The sample descriptions and layer thicknesses are summarized in Table 7.1. Similar to the samples described in previous chapters, a capacitor device is defined by one metallic electrode together with the continuous BFO and SRO layers.

The static characterizations were performed on the as-grown films. For the XRD measurements under electric field, only the volume under the 300 μm large biased electrode was probed with the 100 μm wide X-ray beam.

7.3 Results and discussion

7.3.1 Static characterization : RSM characterization of domain structure

Reciprocal space maps obtained from $\theta - 2\theta$ scans around the 002 Bragg reflection of the different layers are presented in Figure 7.1 where $q_\perp$ is the momentum transfer perpendicular to the sample surface, and $q_{||}$ the corresponding in-plane component parallel to the sample surface. In panel (a), the RSM obtained from sample I is shown. From left to right one can identify the pseudocubic 002 BFO peak and the 220 DSO substrate peak, respectively. The very thin SRO layer peak which should appear on the right of the DSO peak cannot be clearly identified due to the broadness of the peak of this very thin films. Its reflections is masked by the intense substrate reflection.

In Figure 7.1(b) the RSM of the BFO/LSMO/DSO sample (sample II) shows a splitting of the BFO peak along the in-plane momentum transfer vector direction. The intense peak at its right is the reflection from the DSO substrate. The reflection from the LSMO layer appears at larger angles. The clear oscillations on both sides of the peak are the Laue oscillations that confirm the high crystallinity of the film and smooth interface between the film and the substrate [224, 225]. Their periodicity provides information about the film thickness $t = \frac{2\pi}{\Delta Q_z}$ of a layer [226]. From the period of the observed oscillations in Figure 7.1(b), we obtained a coherent thickness of ~ 30.83 nm, corresponding to the LSMO layer thickness, which is about 10% higher than the nominal thickness provided by the sample grower.

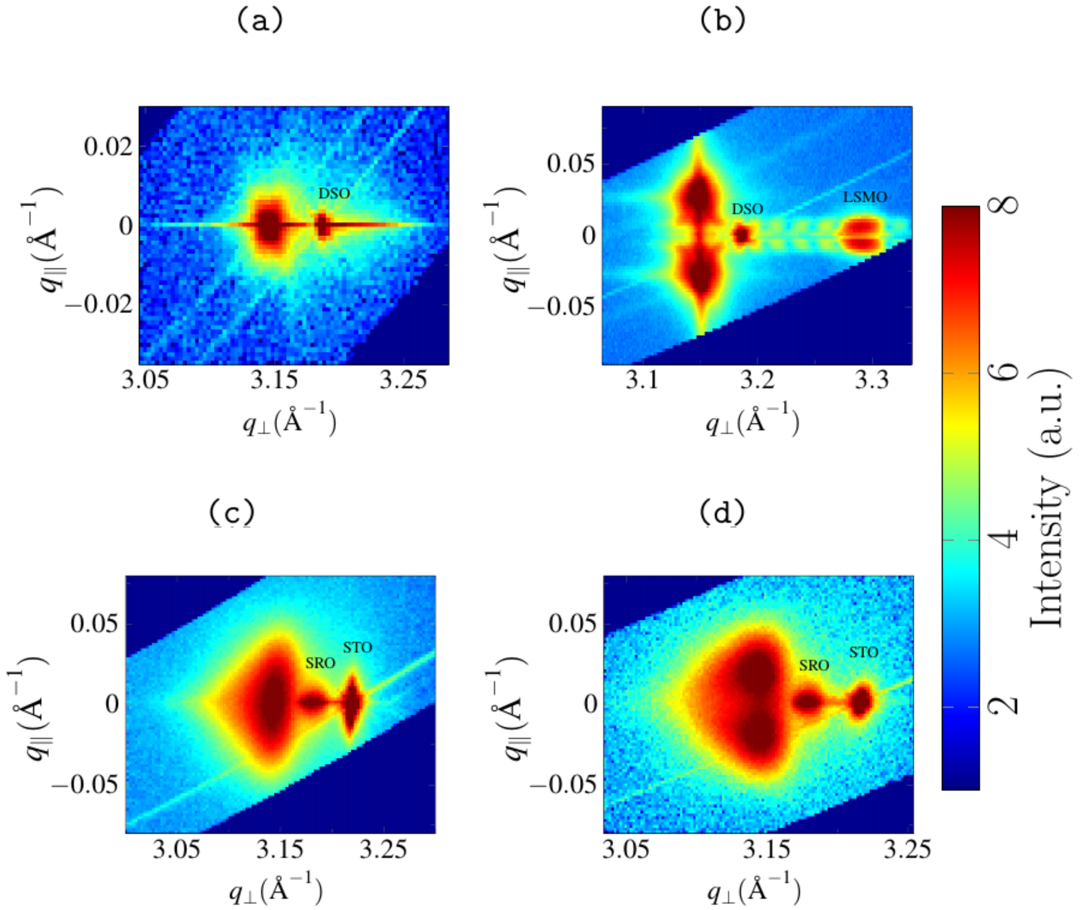

FIGURE 7.1: Reciprocal space map of the as-grown films near the Bragg reflections of the substrates of (a) Sample I (BFO/SRO/DSO) (b) Sample II (BFO/LSMO/DSO) (c) Sample III (BFMO/SRO/STO) and (d) Sample IV (BFMO/SRO/STO). In each map, the substrate and buffer layer are labelled.

Figure 7.1(c) and (d) RSMs show (vertically elongated) 90° rotated heart-shaped Bragg peaks of BFMO obtained from the BFMO/SRO/STO samples, with the thicker film exhibiting a little splitting along $q_{\|}$ that can be seen in panel (d).Thin films of BFO can contain up to 4 ferroelastic domain variants. DSO (110) substrates were used for sample I & II as the (110) surface imposes a small in-plane strain anisotropy, reducing the number of ferroelectric domain variants to two in as-grown films [227]. Also by controlling the thickness of the SRO layer, one can obtain either purely 71° or 109° domains [228]. The investigation of sample I by PFM revealed the presence of pure 71° domain stripes similar to those observed by Lee *et al.,* [229]. Its in-plane line profile is a very sharp Gaussian centered around $q_{\|} = 0$ (blue line Figure 7.2). PFM measurements on samples similar to sample II showed 109° domain stripes similar to those observed by Folkman *et al.,* [230]. And the observed line profile with two peaks centered around $\pm\ 0.03\text{Å}^{-1}$ is typical of samples with such FE domain configuration [229]. The peak splitting has been attributed to the alternating canting angle of adjacent domains in the $(00l)$ planes known as puckering while the weak peaks centered around $\pm\ 0.0015\text{Å}^{-1}$ contain information about the the average domain period [229].

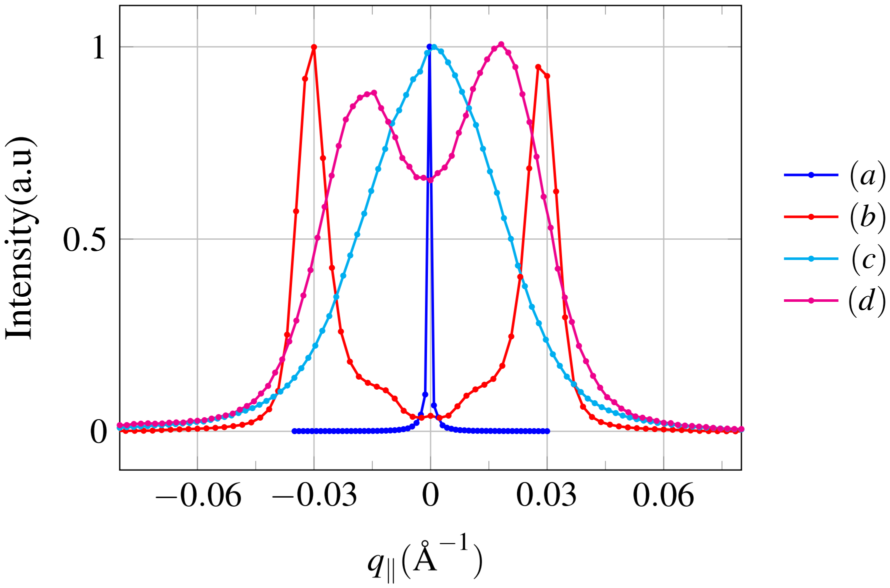

FIGURE 7.2: Line profiles of the BFO peaks along the in-plane direction obtained from integrating the RSMs in Figure 7.1 along $q_{\perp}$.

For sample III and IV, PFM measurements were not performed. We try to estimate their domain configuration by comparing their RSMs to those of samples I and II. From the RSM of sample III (Figure 7.1(c)) and based on the observations in sample I, we can infer that 71° domains are prevailing in this film but the more broad in-plane peak suggests presence of 109° domains. Its in-plane peak width (cyan line in Figure 7.2) is about 14 times larger than in pure 71° film (blue line in Figure 7.2) which is an indication of significant crystal mosaicity. Sample IV, with thicker BFMO layer shows a slightly split peak centered around $\pm\ 0.02\text{Å}^{-1}$ (magenta line in Figure 7.2), suggesting a dominance of 109° domain walls in this case. The fact that the two peaks are not well separated suggests an inhomogeneous canting of the planes, may be due to the presence of few 71° domains stripes. 109° walls have been reported to be more conductive than the 71° ones that have less defects [231]. The latter are most often observed in films grown on (001) STO substrates [232]. The thickness of the BFO layer seems to affect the type of domain pattern that is predominantly formed. As observed from RSM measurements, for the thinner film mostly the 71° walls remained.

Increasing the thickness of BFO (while keeping the SRO thickness constant) led to a change in the dominant domain pattern from 71° to 109°. This is an indication that the compressive in-plane stress due to substrate-film lattice mismatch relaxes with increasing film thickness giving rise to the formation of new domain patterns. Hence, this confirms that the FE domain state is coupled to the distortion of the unit cell structure, undergone to accommodate epitaxial strain.

The above observed relation between ferroelectric domain structure and XRD Bragg peak are considered for further investigation of the dynamics of polarization reversal in BFO thin films.

7.3.2 Polarization reversal in BFO capacitor devices

Although a lot of studies have been carried out on the electric field-induced strain in BFO, its structural dynamics during polarization reversal has not been unambiguously established [218, 233]. We applied coercive and above coercive fields to samples III and IV to follow their structural dynamics by TR-XRD. The field is applied between the SRO bottom electrode and a Pt top electrode of 400 µm diameter in the direction parallel to the pseudocubic c-axis .

We first discuss time-resolved experiments performed on sample III. A line cut from the RSM presented in Figure 7.1(c) at $q_{||} = 0$ showing the Bragg peak positions for each of the constituent layers is presented in Figure 7.4(a). From the BFO Bragg peak positions, its out-of-plane lattice constant was determined to be 3.998 Å which is larger than its bulk lattice constant of 3.96 Å [234]. The experimental procedure is as described in Chapter 4. The RSMs around the BFO (002) Bragg reflection were recorded as a function of time while the electric field was cycled.

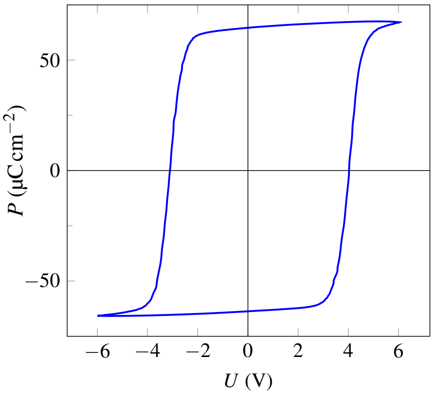

Figure 7.3: $P-E$ hysteresis loop measured on a Pt/BFO/SRO device (sample III) at 2 kHz.

$P-E$ hysteresis measured with a bipolar triangular pulse of 6 V amplitude and 2 kHz frequency is presented in Figure 7.3. The hysteresis shows an asymmetric and fully saturated loop with negative coercivity of about $\sim$ -3.2 V and positive coercivity of 4 V. Since the sample shows fast degradation evidenced by electrical breakdown under above coercive bias, the maximum field applied was restricted to the coercive field.

Pulses of 63 µs ramp time, 50 µs duration and ± 4 V amplitude were applied to the device at a repetition rate of 1 kHz. The time-dependence of the applied pulse sequence is shown in Figure 7.4(b) comprising of two positive and two negative polarity pulses. In ferroelectrics, such double-pulse sequence is used to probe the polarization reversal dynamics under the first pulse, then the dielectric response under the second pulse of the same polarity. Line profiles extracted from the RSMs measured under the electrical pulse sequences are plotted in Figure 7.4(c) and show the diffracted intensity evolution near the BFO Bragg reflection as a function of time and momentum transfer $q_\perp$.

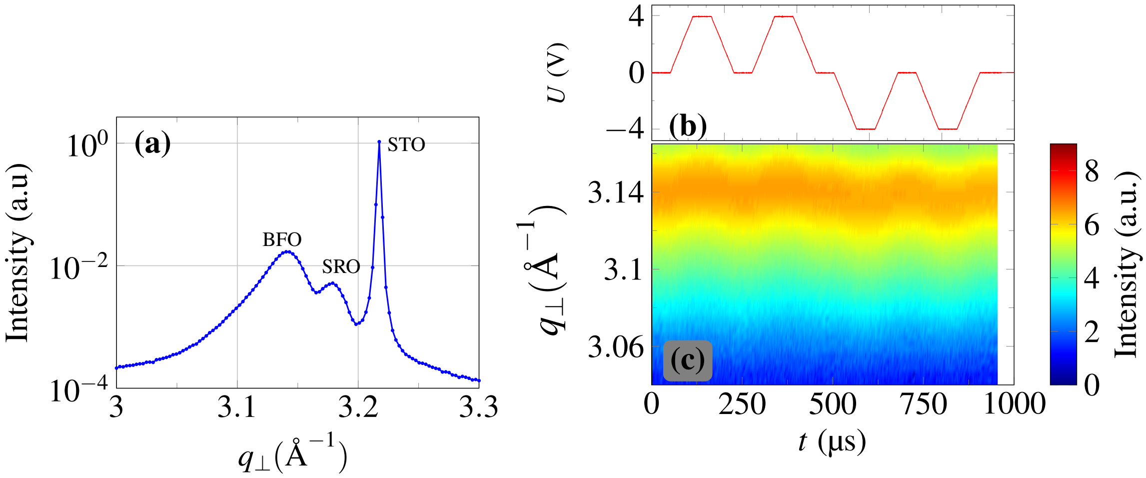

Figure 7.4: Response of the 002 diffraction profile of BFO under applied electric field. (a) Out-of-plane line profile obtained from a cut of the RSM in Figure 7.1(c) around $q_{||} = 0$. (b) Time-dependence of the applied pulse sequence. (c) Colour map of the diffraction intensity as a function of time (horizontal axis) and momentum transfer (vertical axis).

Each vertical line in Figure 7.4(c) is a line profile, similar to that shown in Figure 7.4(a), at one point in time during the electric pulse. The diffracted intensity shifts to to higher $q_\perp$ values when the positive field pulses are applied due to the contraction of the lattice along the applied field direction and returns to its zero-field value when the field is switched off. The application of the negative bias pulses shift the diffracted intensity to lower $q_\perp$ values; indicating a lattice expansion along the c-axis. The center of mass of the intensity versus $q_\perp$ profile of the BFO peak is used to calculate the c-axis at each point in time using Equation 3.8 and thus the strain $\varepsilon = \frac{\Delta c}{c}$ experienced by the BFO layer in the out-of-plane direction. Figure 7.5 summarizes the simultaneously collected information via reciprocal space mapping as a function of time and applied field amplitude.

Panel (b) in Figure 7.5 shows an almost instantaneous lattice response at the onset of the electric field. The field-induced peak shift increases and decreases linearly with the applied field due to the piezoelectric effect. At the maximum applied field, a piezoelectric strain of $\sim 0.8‰$ under positive bias and $\sim 0.9‰$ under negative bias was measured. Domain wall creep motion has been shown in Chapter 4 to induce additional strain in PZT under constant electric field. In this BFO film, the strain is constant during the 50 µs duration of the pulse. The piezoelectric coefficient d_{33} calculated from the strain are 40 pm/V when a positive field is applied to the top electrode and 45 pm/V when the negative bias is applied. These values are in good agreement with previously reported values of 55 pm/V for BFO thin film on STO substrate at field amplitudes less than 150 MV/m [235], that for sample III corresponds to an applied electric voltage of about 30 V.

The width of the out-of-plane momentum vector transfer $w_\perp$ presented in Figure 7.5(c) measures the strain state of the film (the variation in interplanar spacing within the device). The change in $w_\perp$ under electric field implies that the device was not homogeneously strained. The presented quantity $\tilde{w}_\perp$ is the measured width $w_\perp$ normalized to its value at $t = 0$ to facilitate comparison with the different bias polarity. The relative change in $\tilde{w}_\perp$ is about 2% during positive bias and is almost twice higher during negative bias. The normalized peak width of the momentum vector transfer parallel to film surface $\tilde{w}_{||}$ shown in Figure 7.5 (d) is inversely proportional to the applied field, similar to $\tilde{w}_\perp$. The change of $w_{||}$ is related to disorder in the film associated with domain density. The decrease of $w_{||}$ under positive bias as opposed to its increase under negative bias might be an indication that positively charged top electrode create less domain in the film. The relative change in $\tilde{w}_{||}$ is reversible and amounts to $\sim 2\%$ for each polarity. The applied field of 4 V here is just about the macroscopic coercive field value, much smaller than the 6 V at which the $P - E$ hysteresis showed saturation. Thus the results presented here describe minor hysteresis loop. It is therefore not straight-forward to conclude if the dynamics observed is related to polarization switching or only to the piezoelectric effect.

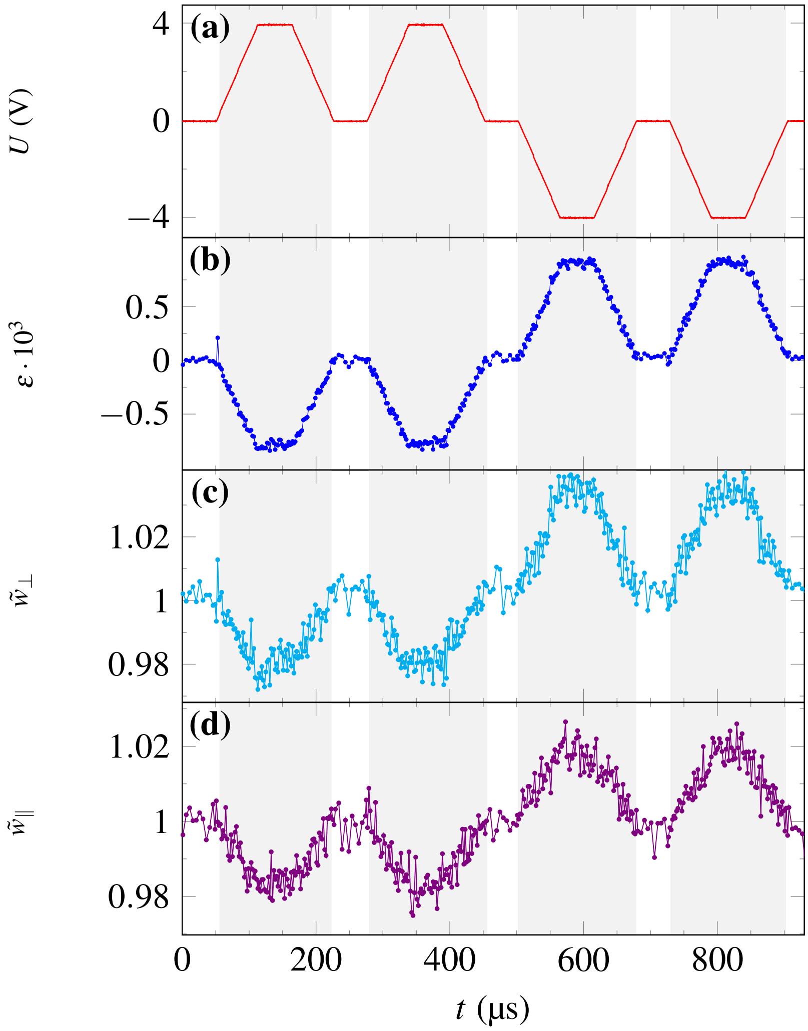

FIGURE 7.5: Time-resolved dynamics of the (002) pseudo-cubic plane under applied electric field. (a) Applied pulse sequence $U(t)$. (b) Out-of-plane lattice strain $\varepsilon(t)$. (c) Normalized FWHM of the out-of-plane Bragg peak $\tilde{w}_\perp(t)$. (d) Normalized FWHM of the corresponding scattering vector parallel to film surface $\tilde{w}_\parallel(t)$.

Sample IV showed higher coercivity due to the thicker BFO layer and resisted longer against the electrical breakdown. Bipolar triangular pulses of 8 V amplitude were applied to a single Pt electrode, and the measured lattice dynamics are presented in Figure 7.6. The switching current presents its maximum at about 6.2 V under positive bias, and -6.4 V under negative bias; thus, the 8 V applied here is largely above the coercive field. The *c*-axis shows a contraction under positive bias and an expansion under negative bias, similar to sample III where near coercive field pulses were applied. The $P-E$ loop calculated from Figure 7.6(b) is presented in Figure 7.7(a). It shows a maximum polarization of $\sim$ 30 µC cm^{-2}, which is only 43% of the saturation polarization of $\sim$ 70 µC cm^{-2} observed in Figure 7.3 for the thinner sample. The absence of a butterfly hysteresis loop as observed from Figure 7.7(b) suggests the absence of 180° polarization switching, from up to down or vice versa, as observed in tetragonal PZT thin films.

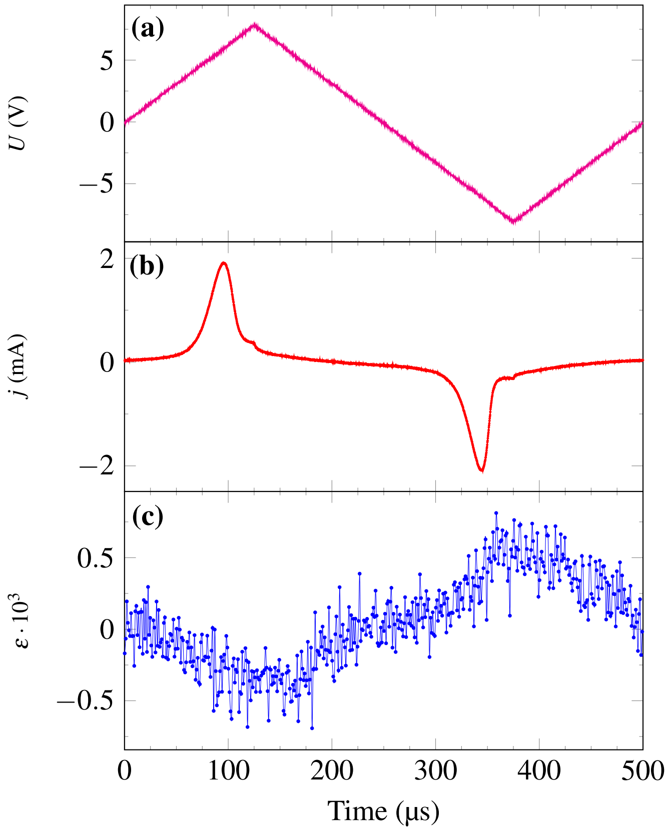

FIGURE 7.6: Time-resolved dynamics of the pseudo-cubic 002 Bragg peak of BFO under triangular pulse. (a) Applied pulse sequence $U(t)$. (b) Current response $j(t)$. (c) Out-of-plane lattice strain $\varepsilon(t)$.

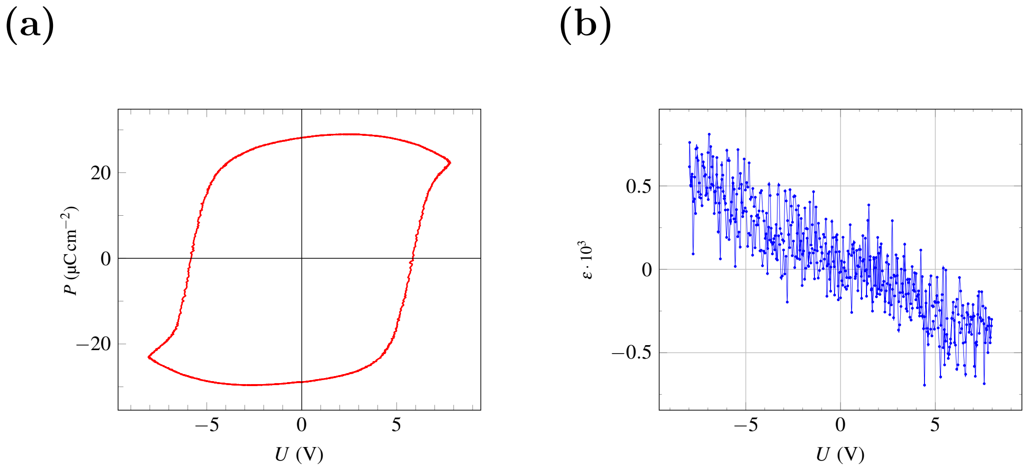

FIGURE 7.7: (a) $P - E$ loop obtained from Figure 7.6 (b). (b)Strain ε versus electric field amplitude U obtained form Figure 7.6 (c).

A 180° polarization reversal requires switching of all 3 components of the polarization vector. The absence of the 180° switching here is not surprising since the field is applied along the vertical component of the polarization vector, giving no direct driving force to switch the in-plane components.

In both films, negative bias induces expansion in the direction parallel to the applied field due to electric field-induced strain. This *c*-axis expansion is accompanied by peak broadening both in-plane and out-of-plane likely due to structural disorder and inhomogeneous strain distribution. The application of the positive field on the other hand induces a contraction of the *c*-axis, accompanied by a decrease in the peak widths. This suggests that already the equilibruim state (field free state) contains a certain level of structural disorder. The opposite sign of the PE response for the different pulse polarity could be due to the fact that most of the dipoles of the as-grown film are pointing towards the surface and applying positive charges to the Pt top electrode leads to contraction while the negatively charged Pt electrode leads to expansion. The reason why the contraction is less than the expansion might be a limitation from the clamping of the film to the substrate. In essence, the macroscopic polarization reversal is not reached during these measurement. For monodomain BFO thin film grown on SRO//(001)STO, Baek *et al.,* demonstrated that the polarization direction of the as-grown film is "down", towards the substrate [236]. This suggests the domain mixture observed in these samples might influence the preferential direction.

7.4 Summary and Conclusion

XRD captures the essential features of FE domains structure. Our static measurements showed that canted (001) planes result in a peak splitting along the momentum transfer parallel to the film surface while monodomain film with 71° domains resulted in a narrow peak. In the time-resolved study, we followed the dynamics of the (002) plane of BFO thin film during electric field loading. The strain response of the film was found to be inhomogeneous over the electrode area, with an average piezoelectric coefficient of 40 pm/V under positive bias and 45 pm/V under negative bias for sample III.The field was applied along the *c*-axis, which affects mostly the vertical component of the polarization vector. The maximum applied field was limited by the device lifetime. The $(00l)$ plane does not give a direct visualization of the polarization vector as opposed to tetragonal ferroelectrics such as $Pb(Zr,Ti)O_3$. Thus, for the case of rhombohedral structures such as BFO, an investigation of a plane including information about one in-plane lattice parameter would provide more clear visualization of the dynamics along the polarization direction during electric field cycling.

CHAPTER 8

Electric field-induced laser-assisted polarization switching

8.1 Introduction

The ability to reverse their polarization from "up" to "down" back and forth is one of the key attributes of ferroelectric materials. The ferroelectric polarization is usually reversed by an electric pulse. During the process, the polarization switching is mediated by the nucleation and growth of regions with oppositely polarized domains [167, 168]. The timescale of this switching process, limited by the domain wall velocity, is about hundreds of picoseconds [237]. The improvement of the switching timescale is a permanent quest for researchers in order to improve device time response especially for applications requiring fast data processing. To achieve this, it has been suggested by simulations, to manipulate the ferroelectric "soft phonon" mode with ultrashort optical pulses to realize reversal times of less than 10 ps [238]. Mankowsky *et al.,* demonstrated a reversal time of less than 80 fs by using femtosecond mid-infrared pulses to excite a high-frequency phonon mode in $LiNbO_3$ making use of the coupling between the latter and the soft phonon mode to displace the atoms within the unit cell along the ferroelectric mode to transiently reverse the polarization, thus achieving a reversal time three orders of magitude faster than with electric pulses. Although they succeeded in reversing the polarization in both directions, the polarization relaxed back to its initial state about 200 fs after the excitation [239].

In this chapter, we discuss an alternative route for stable ultrafast switching of polarization in FE thin films sandwiched between two metal electrodes using an ultrafast acoustic sound wave propagating through the FE and assisting the polarization reversal process. The effect on the switching current, which is a good measure of FE polarization, is presented.

8.2 Experimental details

The first sample used for this experiment consists of a $\sim$ 60 nm BTO layer grown by pulsed laser deposition onto an SRO buffer layer and a (001)-oriented STO substrate. Pt top electrodes of $\sim$ 100 μm size were deposited by e-beam evaporation. This sample was provided to us by Marin Alexe from the University of Warwick, United Kingdom. The second sample used for this study is made of a $\sim$ 100 nm $Pb(Zr_{0.2},Ti_{0.8})O_3$ grown by sol-gel deposition onto a $\sim$ 30 nm SRO buffer on a (001) STO substrate. Top electrodes of diameter between 150 μm and 300 μm were deposited by sputtering of $\sim$ 90 nm thick SRO on the sample surface. This sample was provided to us by Bertrand Vilquin from the Ecole centrale de Lyon, France.

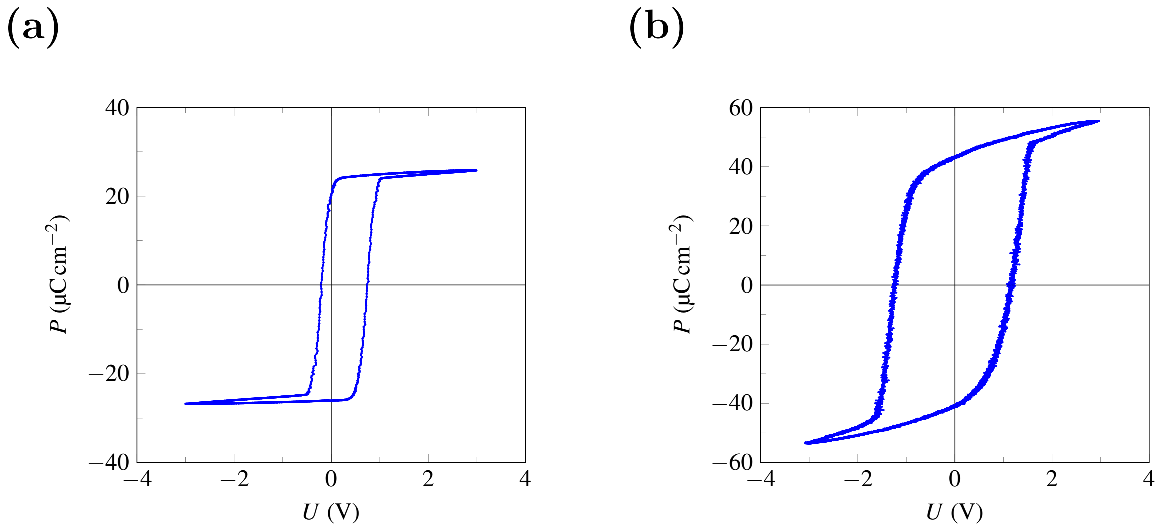

FIGURE 8.1: $P - E$ hysteresis loop measured on (a) Pt/BFO/SRO device (b) SRO/PZT/SRO device at 2 kHz.

Figure 8.1 shows $P - E$ hysteresis loops of the two samples measured at 2 kHz. The $P - E$ loops of both samples show well saturated loops with a high asymmetry for the BTO layer.

For the generation of the strain wave, femtosecond laser pulses with a wavelength of 800 nm were used to excite the buffer SRO layer by shining the laser from the back of the sample through the transparent STO substrate. The substrate was polished to reduce reflections at the air/STO interface. The experimental setup is described in section 3.3. The laser spot had a diameters of $\sim$1000 μm and incident power was 200 mW.

8.3 Results and discussion

Pt/BTO/SRO capacitor device

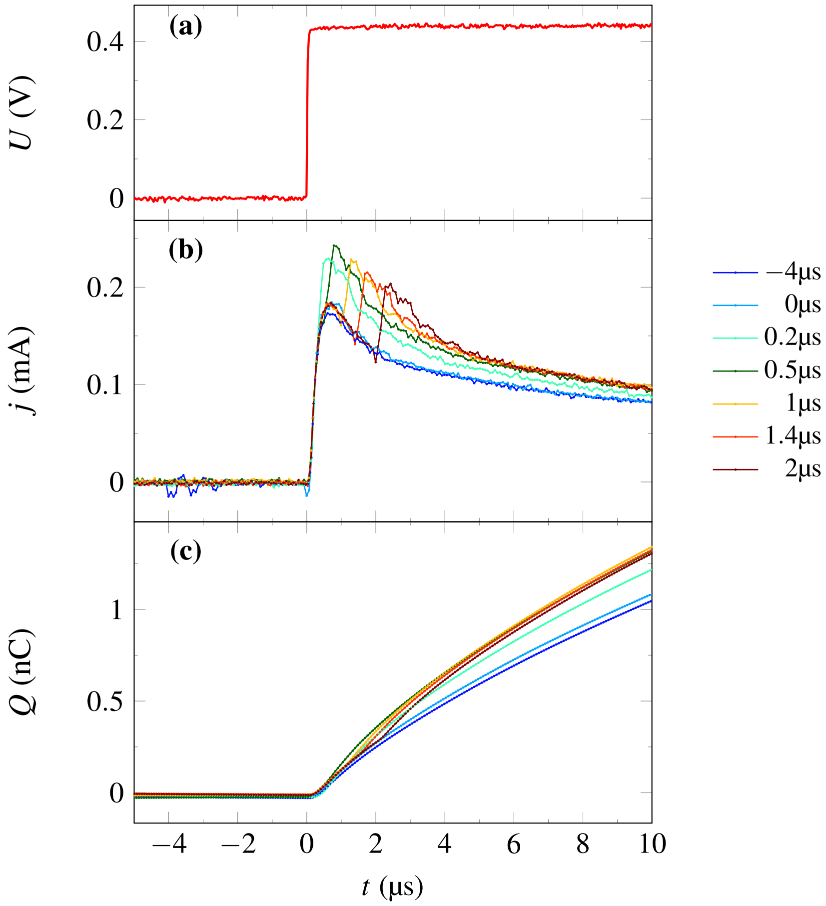

FIGURE 8.2: Laser-induced current in a BTO film under sub-coercive field. (a) Voltage drop U across the capacitor. (b) Measured current for different time-delays indicated in the legend. (c) Corresponding charge obtained by integrating the current in (b) over time.

From the hysteresis presented in Figure 8.1(a), the BTO film shows a positive coercive field of $\sim 0.7\,\mathrm{V}$. We applied a square sub-coercive pulse of $0.45\,\mathrm{V}$ amplitude and we varied the temporal position of the laser by time-delaying the electric pulse. Figure 8.2 shows the measured current response for few time-delays between the laser-pulse and the onset of the electric pulse.

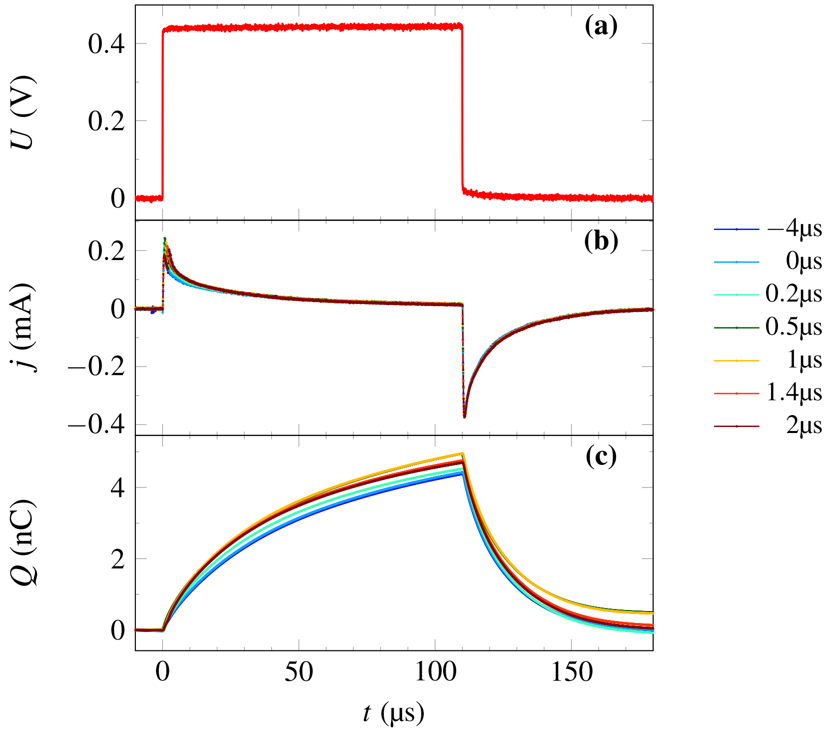

FIGURE 8.3: Laser-induced current in a BTO film under sub-coercive field showing the complete pulse presented in Figure 8.2. (a) Voltage drop U across the capacitor. (b) Measured current for different time-delays indicated in the legend. (c) Corresponding charge obtained by integrating the current in (b) over time.

Figure 8.2(a) shows the voltage drop across the capacitor where time $t = 0$ defines the rising edge of this sub-coercive field pulse. Before this pulse, the sample has seen an above coercive field pulse that poled the film in the opposite direction, ensuring a stable polarization state for the laser-assisted experiment. Figure 8.2(b) shows that an additional current contribution is induced when the laser-pulse excites the electrode during the electrical poling pulse. No additional current is observed when the laser-pulse excites the sample before the electrical pulse (see measurement at -4 μs). The little "wiggle" observed in the current around -4 μs is noise from the Pockels cells of the laser system. The rising slope of the current is the same even at 0 μs delay between the laser excitation and the electrical pulse. This is likely limited by the RC time constant of the device. The integrated current over time presented in Figure 8.2(c) shows an increase when the laser-pulse excites the sample. The additional contribution on the charge seems to be higher when the laser arrives more than 0.5 μs after the electrical pulse onset. The complete pulse showing the falling edge and the discharge current is presented in Figure 8.3

Figure 8.3(c) shows the calculated charge, where the small additional charge induced by the laser-pulse seems to be remanent after the electric pulse has been switched off even though no difference is observed in the discharge current shown in Figure 8.3(b). With the laser excitation 1 μs after the electric pulse onset, the total charge shows a $\sim$ 13% increase as compared to the switching with only the electric pulse.

SRO/PZT/SRO capacitor device

Unlike the BTO film, this PZT film shows a current response also when the laser excites the sample before the electrical pulse although we use a 800 nm laser that corresponds to an excitation energy of 1.54 eV which is far smaller than the 3.5 eV band gap of PZT.

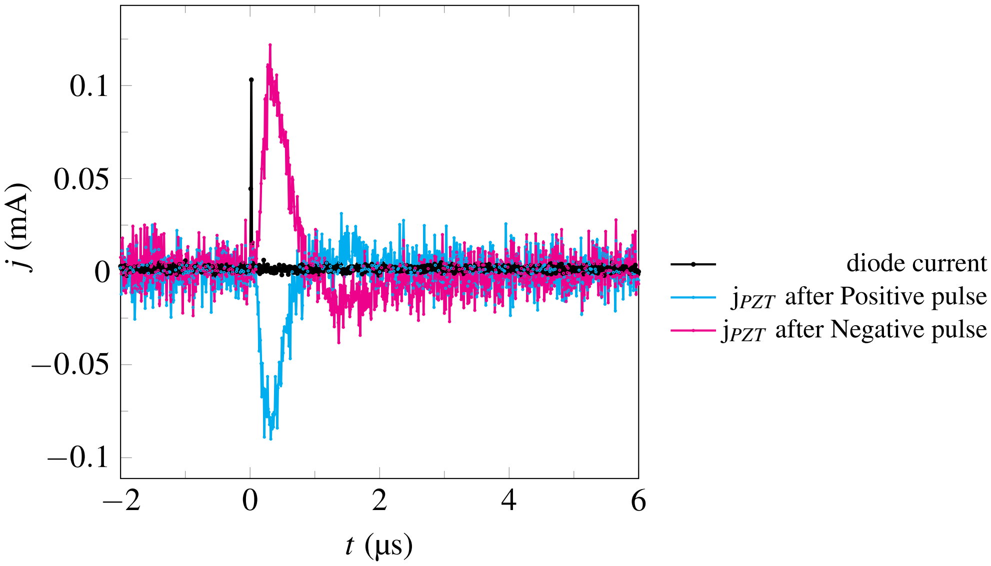

FIGURE 8.4: Laser-induced current in a PZT film after poling the film with a positive (cyan color) and after poling with a negative (magenta color) square pulse of 3 V amplitude. The black color shows the photo-induced current in the photodiode, where its maximum represents the arrival time of the laser pulse at the sample.

Figure 8.4 shows the current induced when the laser-pulse excites the sample after the film has been poled with an electric pulse of positive polarity (in cyan) and that induced when the laser-pulse excites the sample after the film has been poled with an electric pulse of negative polarity (in magenta). We observe that the polarity of this current changes with the polarization direction. Here, time $t = 0$ marks the time at which the laser pulse excites the sample. The photo-induced current of the timing photodiode is plotted as reference and indicates the arrival time of the laser pulse at the sample.

Figure 8.5 shows the induced current when the laser-pulse hits the sample 100 μs after the film has been poled with an electric pulse of negative polarity for different values of the incident laser power.

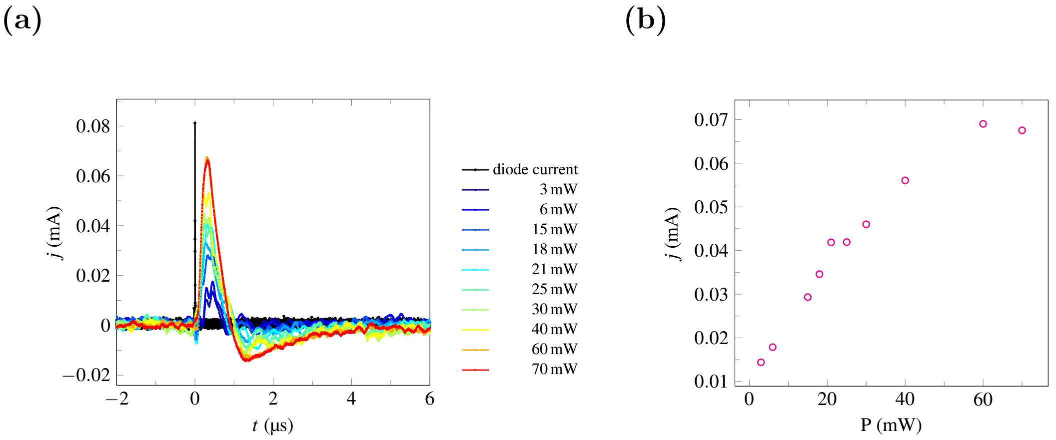

FIGURE 8.5: Laser-induced current in a PZT film 100 μs after poling the film with a negative square pulse of 3 V amplitude. (a) Dependence on laser power. The black color shows the photo induced current in the diode. (b) Current maximum as a function of laser power.

The slope of the induced current (Figure 8.5(a)) develops faster with increasing laser power due to the higher temperature change and lasts for less than 1 μs. This current is likely related to the pyroelectric effect. Pyroelectric currents have been observed before in PZT films [240, 241, 242]. The nearly linear enhancement of the current amplitude (Figure 8.5(b)) with laser power is consistent with the linear increase of deposited heat with laser power.

8.4 Outlook

Increasing the laser power led to an increase in the additional contribution in the current, even for the BTO film. The big challenge with this experiment is the fast electrical breakdown the sample experienced with increasing laser power. When a weak sub-coercive field is applied to a ferroelectric capacitor, the induced contraction is expected to modulate the potential energy but not enough for polarization reversal to occur. The laser excitation of the bottom SRO electrode layer of the device launches a compressive wave that propagates through the FE layer, which we expect to complete the polarization reversal. This would enable a shortening of the switching time scale since switching would be driven in this case by sound propagation. Polarization reversal is accompanied by charge motion which we expect to observe in the current signal. But, as can be seen from the PZT film, additional contributions in the current may also result from pyroelectric current induced by the latent heat from the laser-pulse. The discharge current observed in the latter around 1 μs shows that this induces charge motion. It would be interesting to see how these different charge motion from different origins affect the unit cell structure and domain wall motion within the film. Thus the next step is to study simultaneously the electrical and structural dynamics by using time-resolved X-ray diffraction.

Chapter 9

Summary and outlook

In this thesis, we have studied the polarization reversal in different ferroelectric thin films under periodically applied electric field pulses by simultaneously observing the evolution of charge and lattice response in real time using time-resolved X-ray diffraction and displacement current measurements.

First, we implemented a new time-resolved scheme at the XPP-KMC3 beamline of BESSY II to investigate the dynamics of a $Pb(Zr_{0.2},Ti_{0.8})O_3$ ferroelectric layer under a PUND sequence with pulses of amplitude far above the coercive field of the device. We observe that the complex atomic motion during the ferroelectric polarization reversal starts with a fast contraction of the lattice that tweaks the energy barrier between the two polarization states and facilitates the switching. During this time, domain wall motion is evidenced by the broadening of the in-plane component of the Bragg reflection. The expansive piezoelectric response sets in after considerable charge flow due to the applied electric field on the electrodes of the capacitor. After polarization reversal, domain wall creep motion induces a non-linear piezoelectric response, concomitant with a charge increase, which develops on a much longer time scale than the RC time constant of the device.

We measured the structural dynamics under sub-coercive field conditions showing partial polarization reversal. We observed that the reversal is slower for smaller field as compared to high field strength, and the disordered domain structure induced by domain nucleation and growth is remanent after the field is switched off. The field-dependence of the fraction of the total polarization reversed could be inferred from the structural transients. It was possible to partly reverse the polarization at low field with the pulse applied for a long time. With increasing applied field amplitude, the switching time decreases almost exponentially. We also demonstrated an unpoled state of remanent ferroelectric domain disorder obtained after the application of an "erasing pulse" sequence and suggest that this state be used as a reference state for multilevel data storage.

The electrical and structural dynamics of a $Pb(Zr_{0.52},Ti_{0.48})O_3$ ferroelectric layer, a composition close to the the morphotropic phase boundary, were investigated during triangular pulse cycling. Pulses with the same maximum amplitude and varying frequency were applied and the results highlight the correlation between the polarization-electric field and the electromechanical hysteresis loops. At low frequency, the slow domain wall motion can follow the speed of electrical loading but at high frequency it lags behind. This leads to an increase of the strain and polarization after the maximum field amplitude, although the field is reduced. This considerably distorts the $P - E$ and $\varepsilon - E$ loops towards a more rounded shape. For higher frequencies the polarization reversal is incomplete, despite the high pulse amplitude. A 180° phase lag between the applied field and the structural response is observed at 200 kHz ac cycling frequency. Furthermore, externally modifying the RC time constant of the circuit resulted in an increase of the build-up time of voltage across the FE leading to slower polarization reversal dynamics and higher compressive strain before the reversal.

Static reciprocal space maps of multiferroic (001) oriented $BiFeO_3$ thin films show both the single peak characteristic for 71° domains and the peak splitting associated with 109° domains. Depending on the sample preparation a domain mixture or a certain prevalent domain structure are observed. Time-resolved measurements under external electric field show an inhomogeneous piezoelectric response with an asymmetry between the positive and negative polarities.

Finally, the effect of a 800 nm laser excitation on the bottom electrode of $BaTiO_3$ and $Pb(Zr_{0.2},Ti_{0.8})_3$ based ferroelectric capacitors was investigated by displacement current measurements. We observed an additional current response when the laser pulse excites the metallic bottom $SrRuO_3$ electrode of the sample. The observed current may have two possible origins, one is the pyroelectric effect which responds to a temperature change, and the other is the propagation of a compressive wave through the ferroelectric layer.

This thesis demonstrated that the combination of structural and electrical measurements on ferroelectric thin films is very useful for understanding the coupling between charge and domain wall dynamics within the film. However, real time investigations are sometimes limited by the increase in leakage current and electrical breakdown under long exposure time. Thus, a reduction of the measurement time would be helpful and also make this technique interesting for more routine investigation of FE devices. For the switching under the combined action of electric field and laser excitation, it is important to be able to distinguish between the laser induced strain and the laser induced heat effects on the polarization switching. This can be achieved by exciting the metal electrode with laser pulses of different pulse duration. Future work will look at the simultaneous electrical and structural dynamics in order to understand how these effects modify the domain wall propagation during the switching.

References

[1] L. Maerten, PhD dissertation, University of Potsdam, Germany (2015).

[2] G. Shirane and K. Suzuki, Journal of the Physical Society of Japan **7**, 333 (1952).

[3] G. Shirane, K. Suzuki, and A. Takeda, Journal of the Physical Society of Japan **7**, 12 (1952).

[4] S. Yang, H. Bao, C. Zhou, Y. Wang, X. Ren, Y. Matsushita, Y. Katsuya, M. Tanaka, K. Kobayashi, X. Song, et al., Phys. Rev. Lett. **104**, 197201 (2010).

[5] J. B., W. R. C. Jr., and J. H., *Piezoelectric ceramics* (Academic Press, London, UK, 1971).

[6] M. Haun, E. Furman, S. Jang, and L. Cross, Ferroelectrics **99**, 13 (1989).

[7] I. Kanno, H. Kotera, K. Wasa, T. Matsunaga, T. Kamada, and R. Takayama, Journal of Applied Physics **93**, 4091 (2003).

[8] M. Vijatović, J. Bobić, and B. Stojanović, Science of Sintering **40**, 155 (2008).

[9] K. M. Rabe, C. H. Ahn, and J.-M. Triscone, *Physics of ferroelectrics: a modern perspective*, vol. 105 (Springer Science & Business Media, 2007).

[10] X. Lou, Journal of Applied Physics **105**, 024101 (2009).

[11] T. Graz, *Phy.f20 molecular and solid state physics* (2016), URL `http://lampx.tugraz.at/~hadley/ss1/crystaldiffraction/atomicformfactors/formfactors.php`.

[12] B. Noheda, J. A. Gonzalo, L. E. Cross, R. Guo, S.-E. Park, D. E. Cox, and G. Shirane, Phys. Rev. B **61**, 8687 (2000).

[13] S. Zhang and F. Li, Journal of Applied Physics **111**, 031301 (2012).

[14] M. Zupan, M. Ashby, and N. Fleck, Advanced Engineering Materials **4**, 933 (2002).

[15] J. Kreisel and M. Kenzelmann, Europhysics News, EDP Sciences **5**, 17 (2009).

[16] S. H. Baek and C. B. Eom, Philosophical Transactions of the Royal Society of London A: Mathematical, Physical and Engineering Sciences **370**, 4872 (2012).

[17] W. L. Warren, D. Dimos, B. A. Tuttle, R. D. Nasby, and G. E. Pike, Applied Physics Letters **65**, 1018 (1994).

[18] A. Gruverman, O. Auciello, and H. Tokumoto, Applied Physics Letters **69**, 3191 (1996).

[19] J. Als-Nielsen and D. McMorrow, *Elements of Modern X-ray Physics* (John Wiley & Sons, Ltd, 2011), 2nd ed.

[20] D.-h. Do, P. G. Evans, E. D. Isaacs, D. M. I. N. Kim, C. B. Eom, and E. M. Dufresne (2004).

[21] J. Scott, L. McMillan, and C. Araujo, Ferroelectrics **93**, 31 (1989).

[22] J. R. Teague, R. Gerson, and W. James, Solid State Communications **8**, 1073 (1970), ISSN 0038-1098.

[23] A. M. dos Santos, S. Parashar, A. Raju, Y. Zhao, A. Cheetham, and C. Rao, Solid State Communications **122**, 49 (2002), ISSN 0038-1098.

[24] Y. P. Wang, L. Zhou, M. F. Zhang, X. Y. Chen, J.-M. Liu, and Z. G. Liu, Applied Physics Letters **84**, 1731 (2004).

[25] R. Landauer, D. R. Young, and M. E. Drougard, Journal of Applied Physics **27**, 752 (1956).

[26] N. Setter, D. Damjanovic, L. Eng, G. Fox, S. Gevorgian, S. Hong, A. Kingon, H. Kohlstedt, N. Y. Park, G. B. Stephenson, et al., Journal of Applied Physics **100**, 051606 (2006).

[27] J. S. Speck and W. Pompe, Journal of Applied Physics **76**, 466 (1994).

[28] S. K. Streiffer, J. A. Eastman, D. D. Fong, C. Thompson, A. Munkholm, M. V. Ramana Murty, O. Auciello, G. R. Bai, and G. B. Stephenson, Phys. Rev. Lett. **89**, 067601 (2002).

[29] D. Damjanovic, *The science of hysteresis* (Academic Press Oxford, UK, 2006), vol. 3, chap. Hysteresis in piezoelectric and ferroelectric materials, pp. 337–465.

[30] T. Rojac and D. Damjanovic, Japanese Journal of Applied Physics **56**, 10PA01 (2017).

[31] J. Guyonnet, PhD dissertation, University of Geneva, Switzerland (2014).

[32] S. Stemmer, S. K. Streiffer, F. Ernst, and M. Rüuhle, Philosophical Magazine A **71**, 713 (1995).

[33] D. Atkinson, D. A. Allwood, G. Xiong, M. B. D. Cooke, C. C. Faulkner, and R. Cowburn, Nature materials **2 2**, 85 (2003).

[34] T. Trunk, M. Redjdal, A. Kákay, M. F. Ruane, and F. B. Humphrey, Journal of Applied Physics **89**, 7606 (2001).

[35] G. L. Messing, S. Trolier-McKinstry, E. M. Sabolsky, C. Duran, S. Kwon, B. Brahmaroutu, P. Park, H. Yilmaz, P. W. Rehrig, K. B. Eitel, et al., Critical Reviews in Solid State and Materials Sciences **29**, 45 (2004).

[36] A. Bhalla, R. Guo, and R. Roy, Materials Research Innovations **4**, 3 (2000).

[37] E. Dagotto and Y. Tokura, MRS Bulletin **33**, 1037–1045 (2008).

[38] J. Blasco, J. García, J. M. de Teresa, M. R. Ibarra, P. A. Algarabel, and C. Marquina, Journal of Physics: Condensed Matter **8**, 7427 (1996).

[39] K. A. Müller, W. Berlinger, and F. Waldner, Phys. Rev. Lett. **21**, 814 (1968).

[40] Solid State Ionics **161**, 209 (2003).

[41] G. Kieslich, S. Sun, and A. K. Cheetham, Chemical science **6**, 3430 (2015).

[42] T. Sato, S. Takagi, S. Deledda, B. C. Hauback, and S.-i. Orimo, Scientific reports **6**, 23592 (2016).

[43] C. Li, K. C. K. Soh, and P. Wu, Journal of Alloys and Compounds **372**, 40 (2004).

[44] C. Randall, A. Bhalla, T. Shrout, and L. Cross, Journal of Materials Research **5**, 829 (1990).

[45] P. Baettig, C. F. Schelle, R. LeSar, U. V. Waghmare, and N. A. Spaldin, Chemistry of materials **17**, 1376 (2005).

[46] C. A. Randall, N. Kim, J.-P. Kucera, W. Cao, and T. R. Shrout, Journal of the American Ceramic Society **81**, 677 (1998).

[47] H. Chen, K. Udayakumar, C. Gaskey, and L. Cross, Applied physics letters **67**, 3411 (1995).

[48] X.-h. Du, J. Zheng, U. Belegundu, and K. Uchino, Applied physics letters **72**, 2421 (1998).

[49] G. A. Rossetti Jr, W. Zhang, and A. G. Khachaturyan, Applied Physics Letters **88**, 072912 (2006).

[50] P. Marton, I. Rychetsky, and J. Hlinka, Phys. Rev. B **81**, 144125 (2010).

[51] S. Hwang, C. Lynch, and R. McMeeking, Acta metallurgica et materialia **43**, 2073 (1995).

[52] A. B. Schäufele and K. Heinz Härdtl, Journal of the American Ceramic Society **79**, 2637 (1996).

[53] G. H. Haertling, Journal of the American Ceramic Society **82**, 797 (1999).

[54] R. Cohen, Nature pp. 136—-138 (1992).

[55] D. Berlincourt and H. H. A. Krueger, Journal of Applied Physics **30**, 1804 (1959).

[56] P. Ghosez, PhD dissertation, Université Catholique de Louvain (1997).

[57] F. Zavaliche, S. Y. Yang, T. Zhao, Y. H. Chu, M. P. Cruz, C. B. Eom, and R. Ramesh, Phase Transitions **79**, 991 (2006).

[58] S. K. Streiffer, C. B. Parker, A. E. Romanov, M. J. Lefevre, L. Zhao, J. S. Speck, W. Pompe, C. M. Foster, and G. R. Bai, Journal of Applied Physics **83**, 2742 (1998).

[59] N. Laanait, W. Saenrang, H. Zhou, C.-B. Eom, and Z. Zhang, Advanced structural and chemical imaging **3**, 11 (2017).

[60] D. Lebeugle, D. Colson, A. Forget, M. Viret, A. M. Bataille, and A. Gukasov, Phys. Rev. Lett. **100**, 227602 (2008).

[61] S. Picozzi and C. Ederer, Journal of Physics: Condensed Matter **21**, 303201 (2009).

[62] J. B. Neaton, C. Ederer, U. V. Waghmare, N. A. Spaldin, and K. M. Rabe, Phys. Rev. B **71**, 014113 (2005).

[63] F. Kubel and H. Schmid, Acta Crystallographica Section B **46**, 698 (1990).

[64] C. Ederer and N. A. Spaldin, Phys. Rev. B **71**, 060401 (2005).

[65] J. Heron, J. Bosse, Q. He, Y. Gao, M. Trassin, L. Ye, J. Clarkson, C. Wang, J. Liu, S. Salahuddin, et al., Nature **516**, 370 (2014).

[66] A. J. Hatt, N. A. Spaldin, and C. Ederer, Phys. Rev. B **81**, 054109 (2010).

[67] C. Ederer and N. A. Spaldin, Phys. Rev. B **71**, 224103 (2005).

[68] J. H. Barrett, Phys. Rev. **86**, 118 (1952).

[69] N. Pertsev, A. Zembilgotov, S. Hoffmann, R. Waser, and A. Tagantsev, Journal of Applied Physics **85**, 1698 (1999).

[70] R. Mehta, B. Silverman, and J. Jacobs, Journal of Applied Physics **44**, 3379 (1973).

[71] R. Cowley, Advances in Physics **29**, 1 (1980).

[72] A. Devonshire, Advances in physics **3**, 85 (1954).

[73] K. Ishikawa, K. Yoshikawa, and N. Okada, Phys. Rev. B **37**, 5852 (1988).

[74] N. A. Hill, The Journal of Physical Chemistry **104**, 6694 (2000).

[75] O. Auciello, J. F. Scott, and R. Ramesh, Physics today **51**, 22 (1998).

[76] J. F. Scott and C. A. P. De Araujo, Science **246**, 1400 (1989).

[77] H. Duiker, P. Beale, J. Scott, C. Paz de Araujo, B. Melnick, J. Cuchiaro, and L. McMillan, Journal of applied physics **68**, 5783 (1990).

[78] J. Scott and M. Dawber, Applied Physics Letters **76**, 3801 (2000).

[79] P. Gao, C. T. Nelson, J. R. Jokisaari, S.-H. Baek, C. W. Bark, E. a. D. G. Zhang, Yi andWang, C.-B. Eom, and X. Pan, Nature Communications **2** (2011).

[80] S. M. Yang, T. H. Kim, J.-G. Yoon, and T. W. Noh, Advanced Functional Materials **22**, 2310 (2012).

[81] A. K. Tagantsev, I. Stolichnov, E. Colla, and N. Setter, Journal of Applied Physics **90**, 1387 (2001).

[82] E. L. Colla, S. Hong, D. V. Taylor, A. K. Tagantsev, N. Setter, and K. No, Applied Physics Letters **72**, 2763 (1998).

[83] A. Sidorkin, P. Saint-Gregoire, and L. P. Nesterenko, Journal of Advanced Dielectrics **03** (2013).

[84] P. Joshi and S. Krupanidhi, Applied physics letters **62**, 1928 (1993).

[85] M. Dawber, K. M. Rabe, and J. F. Scott, Reviews of modern physics **77**, 1083 (2005).

[86] W. Warren, D. Dimos, G. Pike, B. Tuttle, M. Raymond, R. Ramesh, and J. Evans Jr, Applied physics letters **67**, 866 (1995).

[87] M. Alexe, C. Harnagea, D. Hesse, and U. Gösele, Applied Physics Letters **79**, 242 (2001).

[88] B. Kang, J.-G. Yoon, D. Kim, T. Noh, T. Song, Y. Lee, J. Lee, and Y. Park, Applied physics letters **82**, 2124 (2003).

[89] J. F. Scott, C. Araujo, H. B. Meadows, L. McMillan, and A. Shawabkeh, Journal of Applied Physics **66**, 1444 (1989).

[90] B. Nagaraj, S. Aggarwal, and R. Ramesh, Journal of applied physics **90**, 375 (2001).

[91] R. Meyer, R. Liedtke, and R. Waser, Applied Physics Letters **86**, 112904 (2005).

[92] Y. Noguchi, I. Miwa, Y. Goshima, and M. Miyayama, Japanese Journal of Applied Physics **39**, L1259 (2000).

[93] Y. Kizaki, Y. Noguchi, and M. Miyayama, Applied physics letters **89**, 142910 (2006).

[94] K. Prume, T. Schmitz-Kempen, and S. Tiedke, *Polar Oxides: Properties, Characterization, and Imaging* (2005), chap. Electrical Characterization of Ferroelectrics, pp. 53 – 75.

[95] D. Damjanovic, Reports on Progress in Physics **61**, 1267 (1998).

[96] C. B. Sawyer and C. H. Tower, Phys. Rev. **35**, 269 (1930).

[97] H. Diamant, K. Drenck, and R. Pepinsky, Review of Scientific Instruments **28**, 30 (1957).

[98] R. Bouregba, B. Vilquin, G. Le Rhun, G. Poullain, and B. Domenges, Review of Scientific Instruments **74**, 4429 (2003).

[99] R. Bouregba and G. Poullain, Journal of Applied Physics **93**, 522 (2003).

[100] J. F. Scott and C. A. Paz de Araujo, Science **246**, 1400 (1989).

[101] Journal of the European Ceramic Society **24**, 1145 (2004), electroceramics VIII.

[102] I. Fina, L. Fàbrega, E. Langenberg, X. Martí, F. Sánchez, M. Varela, and J. Fontcuberta, Journal of Applied Physics **109**, 074105 (2011).

[103] H. Naganuma, Y. Inoue, and S. Okamura, Applied Physics Express **1**, 061601 (2008).

[104] R. Karin M., A. Charles, H., and T. Jean-Marc, *Physics Of Ferroelectrics* (Springer, 2007).

[105] D. Dorset, Microscopy and microanalysis **4**, 513 (1998).

[106] W. H. Zachariasen, *The Theory Of X-ray Diffraction in crystals* (Dover, 1945).

[107] J. Als-Nielsen and D. McMorrow, *Elements of Modern X-ray Physics* (John Wiley & Sons, Ltd, 2011), 2nd ed.

[108] S. Ramaseshan, K. Venkatesan, and N. Mani, in *Proceedings of the Indian Academy of Sciences-Section A*, Springer (Springer, 1957), vol. 46, pp. 95–111.

[109] P. S. Halasyamani and K. R. Poeppelmeier, Chemistry of Materials **10**, 2753 (1998).

[110] S. J. Van Reeuwijk, K. Karakaya, H. Graafsma, and S. Harkema, Journal of Applied Crystallography **37**, 193 (2004).

[111] M. Green and V. E. Cosslett, Proceedings of the Physical Society **78**, 1206 (1961).

[112] D. M. Tucker, G. T. Barnes, and X. Wu, Medical Physics **18**, 402 (1991).

[113] D. Schick, A. Bojahr, M. Herzog, C. v. K. Schmising, R. Shayduk, W. Leitenberger, P. Gaal, and M. Bargheer, Review of Scientific Instruments **83**, 025104 (2012).

[114] M. Ibrahim, Journal of Al-Nahrain University-Science **13**, 51 (2010).

[115] C. Pellegrini and J. Stöhr, Nuclear Instruments and Methods in Physics Research Section A: Accelerators, Spectrometers, Detectors and Associated Equipment **500**, 33 (2003).

[116] E. Giovenale, in *Spectroscopy of Systems with Spatially Confined Structures* (Springer, 2003), pp. 559–592.

[117] M. Chaker, H. Pepin, V. Bareau, B. Lafontaine, I. Toubhans, R. Fabbro, and B. Faral, Journal of applied physics **63**, 892 (1988).

[118] D. Schick, R. Shayduk, A. Bojahr, M. Herzog, C. von Korff Schmising, P. Gaal, and M. Bargheer, Journal of Applied Crystallography **46**, 1372 (2013).

[119] D. Schick, A. Bojahr, M. Herzog, P. Gaal, I. Vrejoiu, and M. Bargheer, Phys. Rev. Lett. **110**, 095502 (2013).

[120] H. Navirian, R. Shayduk, W. Leitenberger, J. Goldshteyn, P. Gaal, and M. Bargheer, Review of Scientific Instruments **83**, 063303 (2012).

[121] R. Shayduk, H. Navirian, W. Leitenberger, J. Goldshteyn, I. Vrejoiu, M. Weinelt, P. Gaal, M. Herzog, C. von Korff Schmising, and M. Bargheer, New Journal of Physics **13**, 093032 (2011).

[122] M. Reinhardt, A. Koc, W. Leitenberger, P. Gaal, and M. Bargheer, Journal of Synchrotron Radiation **23**, 474 (2016).

[123] B. Henrich, A. Bergamaschi, C. Broennimann, R. Dinapoli, E. Eikenberry, I. Johnson, M. Kobas, P. Kraft, A. Mozzanica, and B. Schmitt, Nuclear Instruments and Methods in Physics Research Section A: Accelerators, Spectrometers, Detectors and Associated Equipment **607**, 247 (2009), radiation Imaging Detectors 2008.

[124] D. Schick, R. Shayduk, A. Bojahr, M. Herzog, C. von Korff Schmising, P. Gaal, and M. Bargheer, Journal of Applied Crystallography **46**, 1372 (2013).

[125] B. Henke, E. Gullikson, and J. Davis, Atomic Data and Nuclear Data Tables, 54(2) (1993).

[126] A. Tkachuk and H. Chen, Ferroelectrics **253**, 1 (2001).

[127] A. Tkachuk, H. Chen, P. Zschack, and E. Colla, AIP Conference Proceedings **535**, 136 (2000).

[128] J. J. Hoyt, D. de Fontaine, and W. K. Warburton, Journal of Applied Crystallography **17**, 344 (1984).

[129] S. Wemple, Physical Review B **2**, 2679 (1970).

[130] J. Robertson and C. Chen, Applied Physics Letters **74**, 1168 (1999).

[131] A. K. Tagantsev, Ferroelectrics **184**, 79 (1996).

[132] A. K. Tagantsev, I. Stolichnov, N. Setter, J. S. Cross, and M. Tsukada, Physical Review B **66**, 214109 (2002).

[133] W. S. Oates, in *Behavior and Mechanics of Multifunctional and Composite Materials 2008* (International Society for Optics and Photonics, 2008), vol. 6929, p. 69290C.

[134] S. V. Kalinin and D. A. Bonnell, Physical Review B **65**, 125408 (2002).

[135] A. Gruverman and S. V. Kalinin, Journal of materials science **41**, 107 (2006).

[136] D.-Y. Wang and C.-Y. Chang, Japanese journal of applied physics **44**, 1857 (2005).

[137] W. J. Merz, Physical Review **95**, 690 (1954).

[138] A. Grigoriev, D.-H. Do, D. M. Kim, C.-B. Eom, B. Adams, E. M. Dufresne, and P. G. Evans, Physical review letters **96**, 187601 (2006).

[139] P. Lambeck and G. Jonker, Journal of Physics and Chemistry of Solids **47**, 453 (1986).

[140] I. Vrejoiu, G. Le Rhun, L. Pintilie, D. Hesse, M. Alexe, and U. Gösele, Advanced materials **18**, 1657 (2006).

[141] S. Trolier-McKinstry, N. Bassiri Gharb, and D. Damjanovic, Applied Physics Letters **88**, 202901 (2006).

[142] A. Grigoriev, R. Sichel, H. N. Lee, E. C. Landahl, B. Adams, E. M. Dufresne, and P. G. Evans, Phys. Rev. Lett. **100**, 027604 (2008).

[143] S. Li, W. Cao, and L. E. Cross, Journal of Applied Physics **69**, 7219 (1991).

[144] S. J. Van Reeuwijk, K. Karakaya, H. Graafsma, and S. Harkema, Journal of Applied Crystallography **37**, 193 (2003).

[145] S. Gorfman, H. Simons, T. Iamsasri, S. Prasertpalichat, D. Cann, H. Choe, U. Pietsch, Y. Watier, and J. Jones, Scientific reports **6**, 20829 (2016).

[146] D.-H. Do, P. G. Evans, E. D. Isaacs, D. M. Kim, C. B. Eom, and E. M. Dufresne, Nature materials **3**, 365 (2004).

[147] L. Pintilie, I. Vrejoiu, D. Hesse, and M. Alexe, Journal of Applied Physics **104**, 114101 (2008).

[148] J. J. Lee and S. B. Desu, Ferroelectrics Letters Section **20**, 27 (1995).

[149] P. W. M. Blom, R. M. Wolf, J. F. M. Cillessen, and M. P. C. M. Krijn, Phys. Rev. Lett. **73**, 2107 (1994).

[150] L.-Q. Chen, Journal of the American Ceramic Society **91**, 1835 (2008).

[151] A. Gruverman, B. J. Rodriguez, A. I. Kingon, R. J. Nemanich, A. K. Tagantsev, J. S. Cross, and M. Tsukada, Applied Physics Letters **83**, 728 (2003).

[152] L. E. Cross, Materials chemistry and physics **43**, 108 (1996).

[153] X. J. Lou and J. Wang, Journal of Applied Physics **108**, 034104 (2010).

[154] J. Nuffer, D. Lupascu, and J. Rödel, Acta Materialia **48**, 3783 (2000).

[155] N. Wongdamnern, N. Triamnak, M. Unruan, K. Kanchiang, A. Ngamjarurojana, S. Ananta, Y. Laosiritaworn, and R. Yimnirun, Physics Letters A **374**, 391 (2010).

[156] A. Pramanick, D. Damjanovic, J. E. Daniels, J. C. Nino, and J. L. Jones, Journal of the American Ceramic Society **94**, 293 (2011).

[157] D. A. Allwood, G. Xiong, and R. P. Cowburn, Applied Physics Letters **85**, 2848 (2004).

[158] D. A. Allwood, G. Xiong, C. C. Faulkner, D. Atkinson, D. Petit, and R. P. Cowburn, Science **309**, 1688 (2005).

[159] A. Pramanick, D. Damjanovic, J. C. Nino, and J. L. Jones, Journal of the American Ceramic Society **92**, 2291 (2009).

[160] A. Pramanick, J. E. Daniels, and J. L. Jones, Journal of the American Ceramic Society **92**, 2300 (2009).

[161] B. Kundys, V. Iurchuk, C. Meny, H. Majjad, and B. Doudin, Applied Physics Letters **104**, 232905 (2014).

[162] W. Zhou, Y. Xiong, Z. Zhang, D. Wang, W. Tan, Q. Cao, Z. Qian, and Y. Du, ACS applied materials & interfaces **8**, 5424 (2016).

[163] J. Ayers, Journal of Crystal Growth **135**, 71 (1994).

[164] J. Serafińczuk, Crystal Research and Technology **51**, 276 (2016).

[165] K. Kobayashi, A. A. Yamaguchi, S. Kimura, H. Sunakawa, A. Kimura, and A. Usui, Japanese journal of applied physics **38**, L611 (1999).

[166] Solid State Communications **149**, 1919 (2009).

[167] W. J. Merz, Physical Review **95**, 690 (1954).

[168] D. Kim, J. Jo, T. Kim, S. Yang, B. Chen, Y. Kim, and T. Noh, Applied Physics Letters **91**, 132903 (2007).

[169] M. Dawber, K. Rabe, and J. Scott, Reviews of modern physics **77**, 1083 (2005).

[170] L. Pintilie and M. Alexe, Applied Physics Letters **87**, 112903 (2005).

[171] F. N. Sayed, B. Mandal, O. Jayakumar, and A. Tyagi, AIP Advances **3**, 072133 (2013).

[172] L. Pintilie, I. Vrejoiu, D. Hesse, G. LeRhun, and M. Alexe, Physical Review B **75**, 104103 (2007).

[173] L. Corbellini, J. Plathier, C. Lacroix, C. Harnagea, D. Ménard, and A. Pignolet, Journal of Applied Physics **120**, 124101 (2016).

[174] J. Scott, Journal of Physics: Condensed Matter **20**, 021001 (2007).

[175] A. Kholkin, C. Wütchrich, D. Taylor, and N. Setter, Review of scientific instruments **67**, 1935 (1996).

[176] A. Masys, W. Ren, G. Yang, and B. Mukherjee, Journal of Applied Physics **94**, 1155 (2003).

[177] A. Davydok, T. W. Cornelius, C. Mocuta, E. Lima, E. B. Araújo, and O. Thomas, Thin Solid Films **603**, 29 (2016).

[178] S. Gorfman, H. Choe, V. V. Shvartsman, M. Ziolkowski, M. Vogt, J. Strempfer, T. Łukasiewicz, U. Pietsch, and J. Dec, Physical review letters **114**, 097601 (2015).

[179] F. Vasiliu, P. G. Lucuta, and F. Constantinescu, physica status solidi (a) **80**, 637 (1983).

[180] B. Noheda, D. Cox, G. Shirane, J. Gonzalo, L. Cross, and S. Park, Applied physics letters **74**, 2059 (1999).

[181] R. Guo, L. Cross, S. Park, B. Noheda, D. Cox, and G. Shirane, Physical Review Letters **84**, 5423 (2000).

[182] K. Kakegawa, O. Matsunaga, T. Kato, and Y. Sasaki, Journal of the American Ceramic Society **78**, 1071 (1995).

[183] J. Fernandes, D. Hall, M. Cockburn, and G. Greaves, Nuclear Instruments and Methods in Physics Research Section B: Beam Interactions with Materials and Atoms **97**, 137 (1995).

[184] A. Wilkinson, J. Xu, S. Pattanaik, and S. Billinge, Chemistry of materials **10**, 3611 (1998).

[185] D. Zhou, M. Kamlah, and D. Munz, in *Smart Structures and Materials 2001: Active Materials: Behavior and Mechanics* (International Society for Optics and Photonics, 2001), vol. 4333, pp. 64–71.

[186] Takaakitsurumi, S.-M. Num, Y.-B. Kil, and S. Wada, Ferroelectrics **259**, 43 (2001).

[187] S. Bose and S. Krupanidhi, Applied physics letters **90**, 212902 (2007).

[188] A. Chaipanich, N. Jaitanong, and R. Yimnirun, Ferroelectric Letters **36**, 59 (2009).

[189] G. Catalan, J. Seidel, R. Ramesh, and J. F. Scott, Reviews of Modern Physics **84**, 119 (2012).

[190] Q. Meng, M.-G. Han, J. Tao, G. Xu, D. O. Welch, and Y. Zhu, Phys. Rev. B **91**, 054104 (2015).

[191] Y. Zhou, H. Chan, C. Lam, and F. G. Shin, Journal of applied physics **98**, 024111 (2005).

[192] M. Okatan and S. Alpay, Applied Physics Letters **95**, 092902 (2009).

[193] T. W. Cornelius, C. Mocuta, S. Escoubas, A. Merabet, M. Texier, E. C. Lima, E. B. Araujo, A. L. Kholkin, and O. Thomas, Journal of Applied Physics **122**, 164104 (2017).

[194] J. E. Daniels, A. Pramanick, and J. L. Jones, IEEE transactions on ultrasonics, ferroelectrics, and frequency control **56**, 1539 (2009).

[195] J. Y. Jo, S. M. Yang, T. Kim, H. N. Lee, J.-G. Yoon, S. Park, Y. Jo, M. Jung, and T. W. Noh, Physical review letters **102**, 045701 (2009).

[196] T. Tybell, P. Paruch, T. Giamarchi, and J.-M. Triscone, Physical review letters **89**, 097601 (2002).

[197] W. J. Merz, Journal of Applied Physics **27**, 938 (1956).

[198] W. Li, Z. Chen, and O. Auciello, Journal of Physics D: Applied Physics **44**, 105404 (2011).

[199] Y. Ishibashi and H. Orihara, Integrated Ferroelectrics **9**, 57 (1995).

[200] X. Chen, X. Dong, H. Zhang, F. Cao, G. Wang, Y. Gu, H. He, and Y. Liu, Journal of the American Ceramic Society **94**, 4165 (2011).

[201] H. Naganuma, Y. Inoue, and S. Okamura, Journal of the Ceramic Society of Japan **118**, 656 (2010).

[202] S. Singh, H. Ishiwara, K. Sato, and K. Maruyama, Journal of Applied Physics **102**, 094109 (2007).

[203] Y.-T. Liu, S.-J. Chiu, H.-Y. Lee, and S.-Y. Chen, Thin Solid Films **529**, 66 (2013).

[204] H. A. Navirian, D. Schick, P. Gaal, W. Leitenberger, R. Shayduk, and M. Bargheer, Applied Physics Letters **104**, 021906 (2014).

[205] J.-M. Liu, Q. Xiao, Z. Liu, H. Chan, and N. Ming, Materials chemistry and physics **82**, 733 (2003).

[206] J.-M. Liu, B. Pan, K. Wang, and H. Yu, Ceramics international **30**, 1471 (2004).

[207] X. Chen, X. Dong, F. Cao, J. Wang, and G. Wang, Journal of the American Ceramic Society **97**, 213 (2014).

[208] H. Wu, S. Cao, J. Zhu, and T. Zhang, Acta Mechanica **228**, 2811 (2017).

[209] H. Liu, J. Koruza, P. Veber, D. Rytz, M. Maglione, and J. Rödel, Applied Physics Letters **109**, 152902 (2016).

[210] N. Liu, R. Liang, X. Zhao, Y. Zhang, Z. Zhou, X. Tang, and X. Dong, Journal of Alloys and Compounds **740**, 470 (2018).

[211] M. Bhattacharyya and A. Arockiarajan, Smart Materials and Structures **22**, 085032 (2013).

[212] T. Zhao, A. Scholl, F. Zavaliche, K. Lee, M. Barry, A. Doran, M. Cruz, Y. Chu, C. Ederer, N. Spaldin, et al., Nature materials **5**, 823 (2006).

[213] J. Dho, X. Qi, H. Kim, J. MacManus-Driscoll, and M. Blamire, Advanced Materials **18**, 1445 (2005).

[214] K. Y. Yun, M. Noda, M. Okuyama, H. Saeki, H. Tabata, and K. Saito, Journal of Applied Physics **96**, 3399 (2004).

[215] J. Zhang, B. Xiang, Q. He, J. Seidel, R. Zeches, P. Yu, S. Yang, C. Wang, Y. Chu, L. Martin, et al., Nature nanotechnology **6**, 98 (2011).

[216] J. Moreau, C. Michel, R. Gerson, and W. James, Journal of Physics and Chemistry of Solids **32**, 1315 (1971).

[217] C. Ederer and C. J. Fennie, Journal of Physics: Condensed Matter **20**, 434219 (2008).

[218] N. H. Khansur, T. Rojac, D. Damjanovic, C. Reinhard, K. G. Webber, J. A. Kimpton, and J. E. Daniels, Journal of the American Ceramic Society **98**, 3884 (2015).

[219] H. J. Lee, E.-J. Guo, T. Min, S. H. Hwang, S. Y. Lee, K. Dörr, J. Lee, and J. Y. Jo, Nano Research **11**, 3824 (2018).

[220] S. K. Singh, N. Menou, H. Funakubo, K. Maruyama, and H. Ishiwara, Applied Physics Letters **90**, 242914 (2007).

[221] S. K. Singh, H. Ishiwara, and K. Maruyama, Applied Physics Letters **88**, 262908 (2006).

[222] J.-Z. Huang, Y. Wang, Y. Lin, M. Li, and C. W. Nan, Journal of Applied Physics **106**, 063911 (2009).

[223] R. Guo, L. You, M. Motapothula, Z. Zhang, M. B. Breese, L. Chen, D. Wu, and J. Wang, AIP Advances **2**, 042104 (2012).

[224] A. C. Dürr, F. Schreiber, M. Münch, N. Karl, B. Krause, V. Kruppa, and H. Dosch, Applied Physics Letters **81**, 2276 (2002).

[225] H. L. Wang, C. H. Du, Y. Pu, R. Adur, P. C. Hammel, and F. Y. Yang, Phys. Rev. Lett. **112**, 197201 (2014).

[226] A. Dürr, F. Schreiber, M. Münch, N. Karl, B. Krause, V. Kruppa, and H. Dosch, Applied Physics Letters **81**, 2276 (2002).

[227] N. Laanait, W. Saenrang, H. Zhou, C.-B. Eom, and t. Zhang, Zhan (????).

[228] Y.-H. Chu, Q. He, C.-H. Yang, P. Yu, L. W. Martin, P. Shafer, and R. Ramesh, Nano Letters **9**, 1726 (2009).

[229] J. C. T. Lee, A. R. Damodaran, R. Ramesh, L. W. Martin, and P. Abbamonte, Phys. Rev. B **89**, 214104 (2014).

[230] C. Folkman, S. Baek, H. Jang, C. Eom, C. Nelson, X. Pan, Y. Li, L. Chen, A. Kumar, V. Gopalan, et al., Applied Physics Letters **94**, 251911 (2009).

[231] J. Seidel, L. W. Martin, Q. He, Q. Zhan, Y.-H. Chu, A. Rother, M. Hawkridge, P. Maksymovych, P. Yu, M. Gajek, et al., Nature materials **8**, 229 (2009).

[232] C. Daumont, S. Farokhipoor, A. Ferri, J. Wojdeł, J. Íñiguez, B. Kooi, and B. Noheda, Physical Review B **81**, 144115 (2010).

[233] S. Nakashima, O. Sakata, H. Funakubo, T. Shimizu, D. Ichinose, K. Takayama, Y. Imai, H. Fujisawa, and M. Shimizu, Applied Physics Letters **111**, 082907 (2017).

[234] D. Kan and I. Takeuchi, Journal of Applied Physics **108**, 014104 (2010).

[235] P. Chen, R. J. Sichel-Tissot, J. Young Jo, R. T. Smith, S.-H. Baek, W. Saenrang, C.-B. Eom, O. Sakata, E. M. Dufresne, and P. G. Evans, Applied Physics Letters **100**, 062906 (2012).

[236] S. Baek, H. Jang, C. Folkman, Y. Li, B. Winchester, J. Zhang, Q. He, Y. Chu, C. Nelson, M. Rzchowski, et al., Nature materials **9**, 309 (2010).

[237] J. Li, B. Nagaraj, H. Liang, W. Cao, C. H. Lee, and R. Ramesh, Applied physics letters **84**, 1174 (2004).

[238] S. Fahy and R. Merlin, Phys. Rev. Lett. **73**, 1122 (1994).

[239] R. Mankowsky, A. von Hoegen, M. Först, and A. Cavalleri, Physical review letters **118**, 197601 (2017).

[240] L. E. Garn and E. J. Sharp, Journal of Applied Physics **53**, 8974 (1982).

[241] R. Takayama and Y. Tomita, Journal of Applied Physics **65**, 1666 (1989).

[242] C.-p. Ye, T. Tamagawa, and D. Polla, Journal of applied physics **70**, 5538 (1991).

List of publications

1) C. Kwamen, M. Rössle, W. Leitenberger, M. Alexe and M. Bargheer, "Time-resolved X-ray diffraction study of the structural dynamics in a ferroelectric thin film induced by sub-coercive fields", submitted to Applied physics letters, preprint arXiv:1812.01740, 2018.

2) C. Kwamen, M. Rössle, M. Reinhardt, W. Leitenberger, F. Zamponi, M. Alexe and M. Bargheer, "Simultaneous dynamic characterization of charge and structural motion during ferroelectric switching", Physical Review B, 96, 134105, 2017.

3) M. Sander, A. Koc, C.T. Kwamen, H. Michaels, A. v. Reppert, J. Pudell, F. Zamponi, M. Bargheer, J.Sellmann, J. Schwarzkopf, and P. Gaal, "Characterization of an ultrafast Bragg-Switch for shortening hard x-ray pulses", Journal of Applied Physics, 120, 193101, 2016.

4) V. Iurchuk, D. Schick, J. Bran, D. Colson, A. Forget, D. Halley, A. Koc, M. Reinhardt, C. Kwamen, N.A. Morley, M. Bargheer, M. Viret, R. Gumeniuk, G. Schmerber, B. Doudin, and B. Kundys, "Optical Writing of Magnetic Properties by Remanent Photostriction", Physical Review Letters, 117, 107403, 2016.

Acknowledgments

I would like to express my gratitude to my supervisor Prof. Dr. Matias Bargheer for giving me the opportunity to pursue a PhD in such exciting fields as X-ray diffraction and ferroelectrics. His insightful criticisms have been helpful throughout.

Many thanks to Dr. Matthias Rössle who provided support during beamtimes, and was always available for discussions and reviews. I am sincerely grateful for your availability, advices and help to improve my writing skills.

Thanks to Prof. Catherine Dubourdieu for the discussions.

I would like to thank all my ex-colleagues and colleagues of the Ultrafast Dynamics group at the University of Potsdam. Especially Dr. Matthias Reinhardt, Dr. Flavio Zamponi, Dr. Wolfram Leitenberger, Azize Koc, Dr. Daniel Schick, and Dr. Matthias Rössle who supported me during my beamtimes at BESSY. I would also like to acknowledge Elko Hannemann, Andreas Pucher, and Thomas Waltinger for their help in designing some components needed for the experimental setup. I would also like to thank Dr. Peter Gaal, Lisa Willig, Felix Stete and Radwan for all the good times.

I would like to acknowledge helpful discussions with Dr. Xunlin Qiu about the electrical measurements.

My sincere thanks to Prof. Marin Alexe and Alan Brunier for their coorperation and endless effort in providing me with good samples for my studies. I also say a big thank to Prof. Bertrand Vilquin, Dr. Pedro-Rojo Romeo, Dr. Houssny Bouyanfif, and Prof. Catherine Dubourdieu who also provided good samples used in this thesis.

I am indebted to my father, Daniel, for all the love and care. I would also like to thank the rest of the Kwamen's family, Mireille and Ben for being there for me always.

Last but not the least, a big thank to Azize Koç for being the friend and colleague that she is. She was always available to listen, discuss and encourage me during the odd times. Thanks for everything.

Selbstständigkeitserklärung

Hiermit versichere ich, dass ich die vorliegende Dissertation selbstständig erarbeitet und verfasst habe. Ich habe die vorliegende Dissertation ohne Benutzung anderer als der angegebenen Quellen und Hilfsmittel angefertigt und die direkt oder indirekt übernommenen Zitate aus anderen Quellen kenntlich gemacht.

Diese Dissertation ist bisher an keiner anderen Hochschule oder Universität eingereicht oder veröffentlicht worden.

Potsdam, den 18.12.2018 Christelle Larodia Tchoumba Kwamen